Detection of Supernova and Reactor neutrinos with the Spherical Proportional Counter

Ioannis Katsioulas

Aristotle University of Thessaloniki
Department of Physics

February 2012

Department of Physics,
Aristotle University of Thessaloniki
Postgraduate Diploma Specialisation in Computational Physics

Supervisors:

Assoc. Prof. Ilias Savvidis
Assoc. Prof. Christos Elefthriadis

Tripartite committee:

Assoc. Prof. Christos Elefthriadis
Assoc. Prof. Anastasios Liolios
Assoc. Prof. Ilias Savvidis

Abstract

This project focuses on the study of the conditions for the detection of neutrinos from Supernovae and nuclear reactors, with the Spherical Proportional Counter, by exploiting the neutrino-nucleus coherent elastic scattering. The Spherical Proportional Counter is a novel proportional gaseous detector, developed to exploit the many advantages of the spherical geometry. These advantages are presented here, along with the characteristics of the detector. Neutrinos coming from a Supernova carry 99% of its energy. Thus they are an excellent source of information, about its internal mechanisms. In the present work the possible neutrino emission spectra of a Supernova are studied and the detector's response to them is calculated. Different parameters of the detector are taken into account, such as the threshold energy, the gas filling (Ar, Xe) and the size of the detector. It is very important to know well the behaviour of our detector, before moving to the detection of Supernova neutrinos. For this reason it is proposed to test the system using terrestrial neutrino sources. The most important terrestrial neutrino source are the nuclear reactors, as the detection of the neutrinos emitted by them, offers important applications such as the precise control of the nuclear reactor. The Spherical Proportional Counter is tested to the detection of nuclear recoils (Ar nuclei), by exploiting the neutron-nucleus elastic scattering, from which we have low energy recoils. As neutron source is used an AmBe source. The possible shieldings of the detector are studied by simulation using FLUKA. In this work we also examine various aspects of this experimental procedure, such as the use of various elements of the signal (amplitude, rise time, and duration of the pulse), for the discrimination of the different radiations interacting with the detector, during data analysis, using the ROOT package.

Acknowledgements

I would like to thank my supervisors, Assoc. Prof. Ilias Savvidis for his understanding and help all this years and Assoc. Prof. Christos Elefthriadis for the always useful comments and advises. Also I would like to thank the other member of the tripartite committee Assoc. Prof. Anastasios Liolios for his remarks.

I owe special thanks to Dr. Georgios Tsiledakis who helped when I thought I was lost.
Thank God that I have a family that supported me in every step all this years, even when they shouldn't.

Contents

Chapter 1

Introduction

Neutrinos appear to be excellent probes for studying the deep sky. They travel large distances with the speed of light. They can pass through obstacles, without getting distorted on their way and they are not affected by the presence of magnetic fields. Thus with neutrinos one can see much further than with light one cannot observe further than 50 Mpc ($1\ Mpc = 3.3 \times 10^6\ light\ years$). Furthermore the detection of neutrinos reveals information about the source and more specifically about the source interior. Without neutrinos we would probably know nothing about the sun's interior. Thus neutrinos offer a good hope for understanding the early stages of a supernova. In a typical supernova an energy of about $10^{53}\ ergs$ is released in the form of neutrinos. These neutrinos are emitted within an interval of about $10\ s$ after the explosion and they travel to Earth undistorted, except that, on their way to Earth, they may oscillate into other flavors. The phenomenon of neutrino oscillations is by now established by the observation of atmospheric neutrino oscillations interpreted as $\nu_\mu \to \nu_\tau$ oscillations, as well as ν_e disappearance in solar neutrinos. These results have been recently confirmed by the KamLAND experiment, which exhibits evidence for reactor anti-neutrino disappearance. Thus for traditional detectors relying on the charged current interactions the precise event rate may depend critically on the specific properties of the neutrinos. The time integrated spectra in the case of charged current detectors, like the SNO experiment, depend on the neutrino oscillations. This, of course, may turn into an advantage for the study of the neutrino properties. An additional problem is the fact that the charged current cross sections depend on the details of the structure of the nuclei involved. During the last years various detectors aiming at detecting recoiling nuclei have been developed in connection with dark matter searches with thresholds in the $10\ keV$ region. Recently, however, it has become feasible to detect neutrinos by measuring the recoiling nucleus and employing gaseous detectors with much lower threshold energies. Thus one is able to explore the

advantages offered by the neutral current interaction, exploring ideas put forward more than a decade ago. This way the deduced neutrino fluxes do not depend on the neutrino oscillation parameters (e.g. the mixing angles). Even in our case, however, the obtained rates depend on the assumed characteristic temperature for each flavor. Furthermore this interaction, through its vector component, can lead to coherence, i.e. an additive contribution of all nucleons in the nucleus. Since the vector contribution of the protons is tiny, the coherence is mainly due to the neutrons of the nucleus.

A new type of radiation detector, the Spherical Proportional Counter (SPC), was developed recently based on a spherical geometry. The detector consists of a large spherical gas volume with a central electrode forming a radial electric field. Charges deposited in the conversion volume drift to the central sensor where they are amplified and collected. A small spherical sensor is located at the center acting as a proportional amplification structure. It allows high gas gains to be reached and operates in a wide range of gas pressures. The SPC has been proven to operate in a simple and robust way and allows reading large volumes with a single read-out channel. The spherical geometry gives many advantages to a proportional counter, one of the most important is, the development of large drift volumes ($radius > 10m$) with very low electronic noise. Sub-keV energy threshold, measuring x-rays, with good energy resolution has been achieved with this detector. In this project we study the conditions required, to detect low energy nuclear recoils with the Spherical Proportional Counter, by exploiting the neutrino-nucleus coherent elastic scattering.

Chapter 2

The Spherical Proportional Counter

2.1 Detector description

The detector consists of a hollow copper sphere (the sphere is actually an old LEP cavity) of 1.3 meter in diameter and 6 mm thick surrounding a small stainless ball of 1.4 centimeter in diameter. It operates in a sealed mode: the spherical vessel is first pumped out and then filled with an appropriate gas at a pressure from low pressure up to 5 bar. The ball is maintained in the centre of the sphere by a stainless steel rod. In the simplest design the small spherical electrode acts as proportional amplification counter and is read by a single channel electronic chain. A picture of detector and surrounding equipment is shown in Fig. 2.1. The

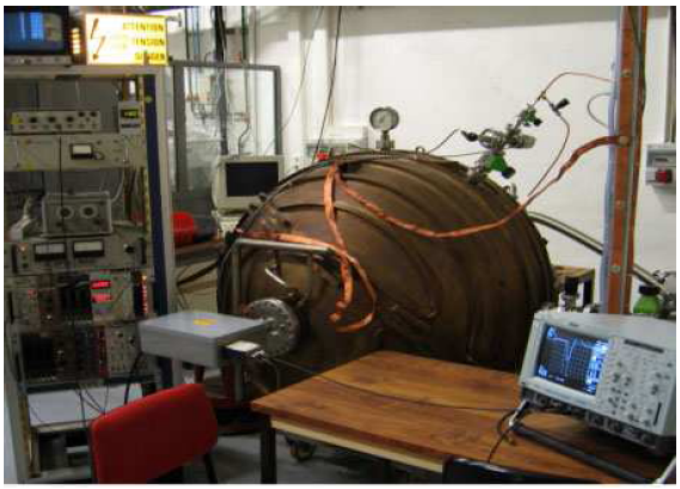

Figure 2.1: A photograph of the spherical vessel and electronics.

detector was operated with positive bias applied to the anode (inner sphere) while the cathode (external sphere) remained at ground potential. A high voltage capacitor was decoupling the high voltage cable to protect the sensitive preamplifier.

The anode ball 14 mm in diameter was made out of stainless steel [5].

2.2 The electric field

In the spherical proportional detector, the electric field depend on the anode radius r_2, cathode radius r_1 (cathode voltage is set at 0 Volt) anode voltage V_0 and radial distance r. To calculate it at a distance r we apply the Gauss's Law:

$$\int \vec{E} d\vec{S} = \frac{Q}{\varepsilon}$$

where ε is the gas permittivity (of the order of $0.1\ pF/cm$) and Q is the total charge of the positive ions. The integration on a sphere of radius r gives:

$$E(r) = \frac{Q}{4\pi\varepsilon}\frac{1}{r^2}$$

Using $E = -\nabla V$ we have

$$V(r) = -\int E(r)dr = \frac{Q}{4\pi\varepsilon}\int \frac{dr}{r^2} = \frac{Q}{4\pi\varepsilon}\frac{1}{r^2} + C^t$$

Now applying the boundary conditions $V(r_2) = V_0$; $V(r_1) = 0$, we obtain:

$$V = V_0\rho(\frac{1}{r} - \frac{1}{r_1}) \tag{2.1}$$

with

$$\frac{1}{\rho} = \frac{1}{r_2} - \frac{1}{r_1}$$

and

$$V_0 = \frac{Q}{4\pi\varepsilon\rho}$$

From this equation we can deduce the capacitance of the detector

$$C = 4\pi\varepsilon\rho \tag{2.2}$$

which is of the order of1 pF, and now the intensity of the electric field E can be written as:

$$E(r) = \frac{V_0}{r^2}\rho \tag{2.3}$$

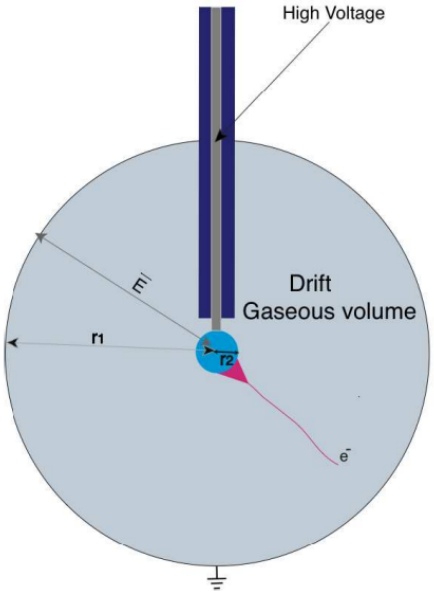

Figure 2.2: A positive High Voltage (HV) applied in the central producing a radial electric field in the inner spherical volume. An electron created in the gas volume drifts to the central electrode producing an avalanche near the spherical ball at a distance of a few *mm*. Positive ions moving backward are inducing a signal to the preamplifier.

2.3 The Detector response

Energetic charged particles, x-rays, or gamma rays or even neutrons entering the detector strip electrons from the gas atoms to produce positively charged ions and negatively charged electrons. The electric field created across the electrodes drifts the electrons to the positive electrode. Near the inner anode sphere the electric field is high enough and electrons gain enough energy to ionize more gas atoms, a process that produces more electrons. Typical gases at atmospheric pressure require field strength on the order 10kV/cm to produce the avalanche of secondary electrons around the small anode ball. The avalanche is produced at a few mm distance from the anode and the positive ions drifting toward the cathode are inducing a pulse to the charge preamplifier. Since the avalanche takes place near the small ball and the electrons are attracted to it the positive ions travel a much greater distance. Therefore the induced pulse to the preamplifier is mainly due the ion movement; electrons produced during avalanche process have a negligible contribution to the signal.

Now we want to find the signal induced by the ions displacement created by an avalanche at time $t = 0$. The ion mobility in the gas, μ, is taken as independent

of the electric field but inversely proportional to the pressure P:

$$\mu = \frac{\mu_0}{P}$$

where μ_0 is the mobility at 1 atm of the order of 2×10^{-6} $cm^2 V^{-1} \mu s^{-1}$. By definition:

$$\mu = \frac{1}{E(r)} \frac{dr}{dt}$$

Replacing $E(r)$ by (2.3):

$$r^2 dr = a dt$$

with

$$\alpha = \mu_0 \frac{V_0}{P} \rho$$

Note the parameter α is a function of V_0/P. The integration no the drift range gives:

$$\int_{r_2}^{r} u^2 du = \int_0^t \alpha du$$

So the ions arrive at time t at the distance r given by:

$$r = (r_2^3 + 3\alpha t)^{1/3}$$

The duration of the ions drift corresponds to $r = r_1$:

$$t_{max} = \frac{r_1^3 - r_2^3}{3\alpha}$$

for the SPC with radius 0.65 cm, filled with Argon at pressure $P = 1$ atm we have an approximate value of $t_{max} = 10$ s.

The general method to calculate the induced charge on electrodes due to the motion of charge carriers in a detector makes use of the Shockley-Ramo Theorem [42] and the concepts of the *weighting field* and *weighting potential*. The theorem states that the instantaneous current induced on a given electrode is equal to

$$i = q\vec{v}\Delta\vec{E}_0$$

where q is the charge of the carrier, $\vec{v}$ its velocity, and $\vec{E}_0$ is called the weighting field. Another way of stating the same principle is that the induced charge on the electrode is given by the product of the charge of the carrier multiplied by the difference in the weighting potential ϕ_0 from the beginning to the end of the carrier path:

$$Q = q\Delta\phi_0$$

To find this weighting potential ϕ_0 as a function of position, one must solve the Laplace equation for the geometry of the detector, but with some artificial boundary conditions:

1. The voltage on the electrode for which the induced charge is to be calculated is set equal to unity.

2. The voltages on all electrodes are set to zero.

3. Even if a trapped charge is present within the detector volume, it is ignored in the calculation.

The solution under these conditions gives the weighting potential, and its gradient is the weighting field. The weighting potential is *not* the actual electric potential in the detector but instead serves as a convenience that allows simple determination of the induced charge on the electrode of interest by taking differences in the weighting potential at the start and end of the carrier motion. The path of the carrier must still be determined from the actual electric field lines. If the position of the carrier as a function of time is determined as previously described, then the time profile of the induced charge (or the induced current) can also be traced out to determine the shape of the out put pulse.

Now we can apply the Shockley-Ramo theorem to compute the charge on the small sphere induced by the movement of the ions:

$$\begin{aligned} dQ_{ind} &= q_{ions} d\phi_0 \\ dQ_{ind} &= -q_{ions} E(r) dr \\ dQ_{ind} &= -q_{ions} v_{ions} E(r) dt \\ dQ_{ind} &= -q_{ions} \mu E^2(r) dt \\ dQ_{ind} &= -q_{ions} \alpha \rho \frac{dt}{r^4} \end{aligned}$$

If we substitute the expression (2.3) of $r(t)$ in this equation, we get:

$$dQ_{ind} = -q_{ions} \alpha \rho (r_2^3 + 3\alpha t)^{-\frac{4}{3}} \tag{2.4}$$

By integration on time, we get the charge pulse given by the detector for an avalanche created at time $t = 0$:

$$Q_{ind} = -q_{ions} \rho [\frac{1}{r_2} - \frac{1}{(r_2^3 + 3\alpha t)^{1/3}}] \tag{2.5}$$

And from this equation we can derive the signal with respect to time:

$$V(t) = V_0 \rho [\frac{1}{(r_2^3 + 3\alpha t)^{1/3}} - \frac{1}{r_1}] \tag{2.6}$$

Note, that at the maximum ions drift time t_{max} given by relation (2.3), which is the duration of the detector pulse, the induced charge equals the avalanche ones:

$$Q_{ind} = -q_{ions}$$

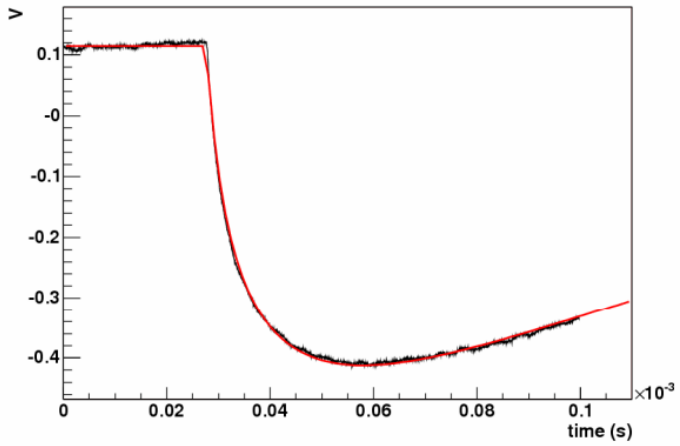

Figure 2.3: Pulse observed by a ^{55}Fe X-ray (black line) well reproduced by the calculation (red line).

Now we can derive the expected shape of the induced signal by taking into account the preamplifier shaping constant. Using the preamplifier transfer function we will reproduce the observed signal. As the transfer function of the amplifier, we can take the exponential:

$$A_0 = e^{-X}, \qquad \text{with} \quad X = \frac{t - t_0}{\tau} \tag{2.7}$$

or a more general function which parametrizes the rising t_r and the falling t_f time:

$$A = e^{-X_1} - e^{-X_2} \tag{2.8}$$

with $X_1 = \alpha(t - t_0)$ and $X_2 = b(t - t_0)$, $\alpha = 1/t_f$ and $b = 1/t_f + 1/t_r$. For the standard amplifiers used in neutron spectroscopy the rising time is very small in respect to the falling time, so the transfer function is approximated by A_0 . The electronic signal given by an avalanche created at $t = 0$ is then given by the convolution of the detector response and the amplifier transfer function:

$$S(t) = \int_0^t A(t-u)\frac{dQ_{ind}}{du}(u)du \tag{2.9}$$

so we need to compute :

$$S(t) = -q_{ind}\alpha\rho e^{-\frac{t}{\tau}} \int_0^t e^{\frac{u}{\tau}}(r_2^3 + 3\alpha u)^{-\frac{4}{3}}du \tag{2.10}$$

if we assume a shaping constant of $\tau = 120\mu s$ The numerical integration shows that the avalanche signal can be parametrized by an expression similar to (2.8) :

$$S(t) = -q_{ions}k(e^{-\alpha t} - e^{-bt}) \tag{2.11}$$

with the scaling constant k close to the ballistic deficit. The parameters α,b, and k are function of V_0 and τ. The detector response and a typical signal from

an avalanche are shown on Fig.2.4 and Fig.2.5. The variation of the signal parameters versus V_0/P (detector) is shown on Fig.2.6 and versus τ (amplificator) on Fig.2.7. The main feature is that the ballistic deficit is always greater than 50% [2].

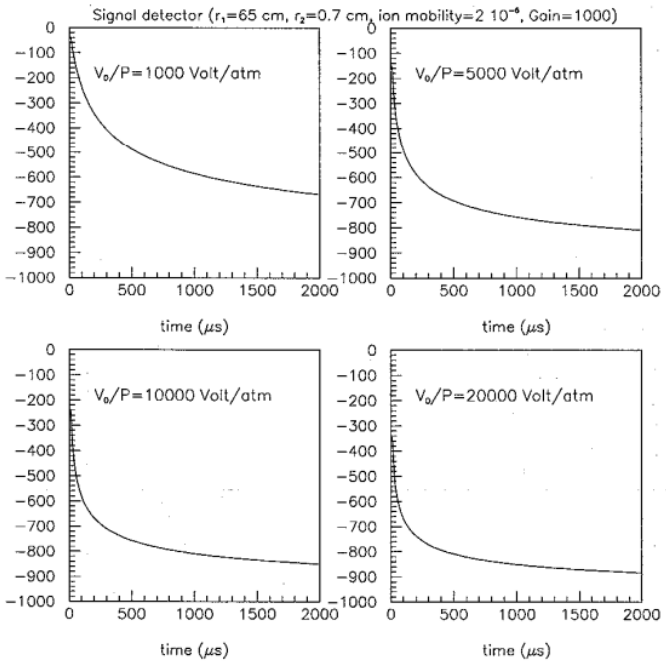

Figure 2.4: Simulation of the detector response.

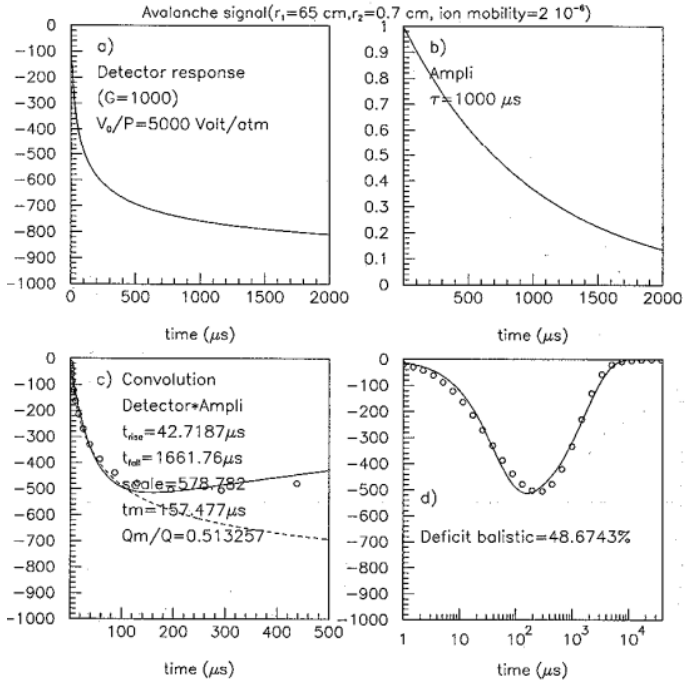

Figure 2.5: Simulation of the signal given by avalanche (t=0), scale=$q_{ions}k$.

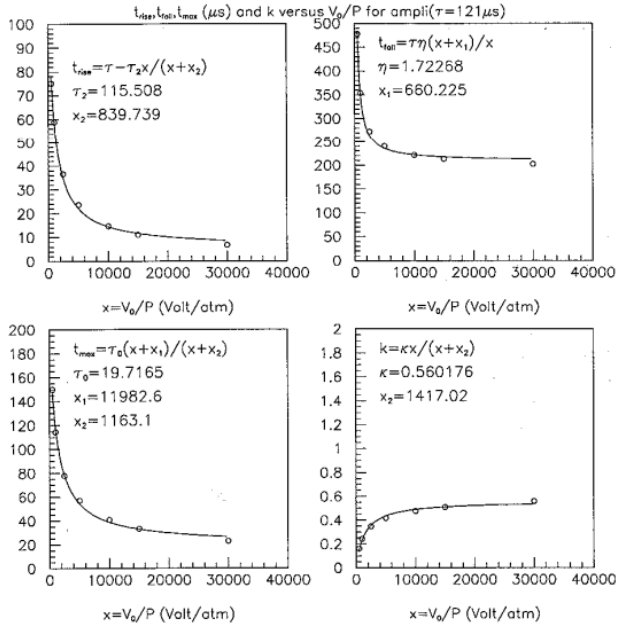

Figure 2.6: Simulation of the avalanche signal versus V_0/P.

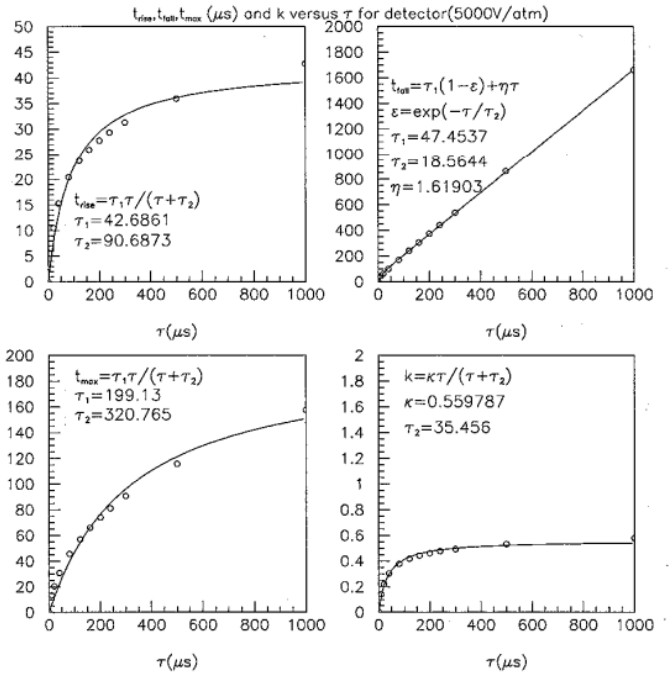

Figure 2.7: Simulation of the avalanche signal parameters versus τ.

2.4 Electrostatic of the Spherical TPC

In a real implementation of the spherical TPC concept, the ideal spherical symmetry is broken by the rod that supports the central electrode and that necessarily connects it to the front-end electronics, placed outside, to amplify and read the signals. In Fig.2.8 the equipotential lines are plot for this simplest geometry, showing how the presence of this rod makes the electric field to be far from spherically symmetric. In particular, by doing simple electrostatics calculations, we see that only about 20% of the volume have field lines that end up in the spherical electrode, while the rest go to the cylinder, in which no amplification (or a wrong one) is expected.

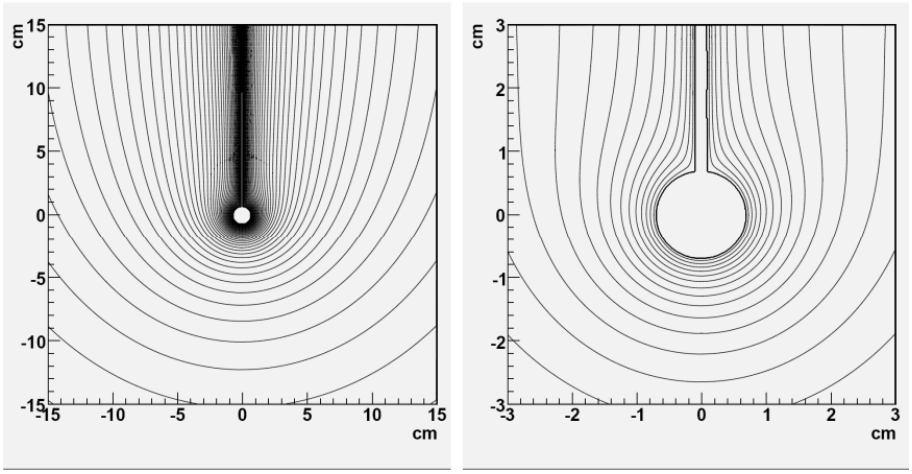

Figure 2.8: Electric field (equipotential lines) around the simplest electrode geometry (sphere connected to stick).

Moreover, a close inspection of the voltage gradient in the region very close to the electrode surface (less than few mm), where the amplification of the signal is expected to occur, shows variations along the surface which leads to amplification factors that will depend on the precise point on the electrode surface where the field line ends. This inhomogeneity in gain is magnified by the usual exponential dependence of the avalanche gain with the electric field. Therefore, this simple geometry, although necessary to provide a proof of the principle of detection with a point-like source, is unsuitable for a serious application where a homogeneous response over the detector volume is required. Current efforts focus on the design of an electrostatic structure that allows bringing the high voltage to the internal sphere with minimal distortion of the spherical field, both for purposes of drift and homogeneous amplification all around the small sphere.

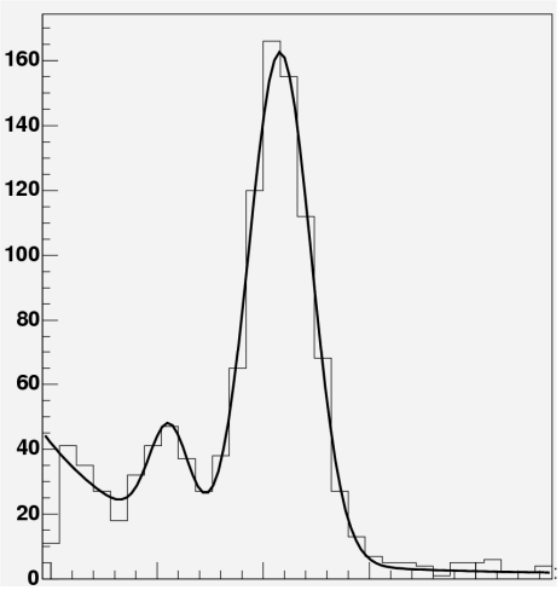

Figure 2.9: Pulse height distribution of the signal produced by a ^{55}Fe source.

2.5 Results in the simplest electric field configuration

In this section are given the results obtained in the simple mode without using any field correction system but simply testing only the 'good' hemisphere. In this compartment a ^{55}Fe source is introduced inside the sphere by means of a movable stick which allows us to place the source at any distance from the inner electrode. The first tests were oriented to the assessment of the tightness of the vessel, so the gas could keep the sufficient level of purity for right operation. The volume was pumped by a primary pump followed by a turbo molecular pump, reaching a level of vacuum below 10^{-6} $mbar$. The outgassing rate measured was below 10^{-9} $mbar/s$, which allows us to avoid permanent gas circulation through special cleaning filters and to operate instead in seal mode. The gas was introduced into the vessel through a simple oxisorb filter. Data taken at different source distances show no evidence of loss of signal intensity due to electron attachment. In Figure 2.9 shows the recorded energy spectrum obtained irradiating the detector with a ^{55}Fe source, the energy resolution obtained is 18% (FWHM) in Ar + 10% CO_2 gas mixture.

The prototype has been operated with two different gas mixtures, namely Ar + 10% CO_2 as well as Ar + 2% $Isobutane$; and at different pressures up to 1.5 bar. These first tests showed that even with such a simple amplification element, high gas gains (above 104) are easily achieved. Figure 2.10 and Figure 2.11 show the obtained gain versus voltage using Argon as carrier gas mixed with 2% Isobutane

and 10% CO_2 respectively for various gas pressures. Notice the advantage of the Isobutane mixture requiring twice lower voltage at same pressure. Stable oper-

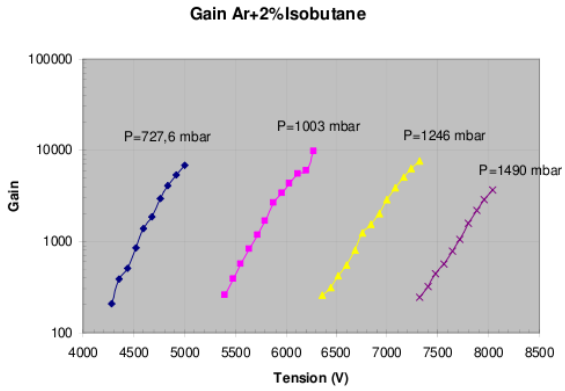

Figure 2.10: Effective gas gain versus high voltage for various pressures in Ar + 2% Isobutane.

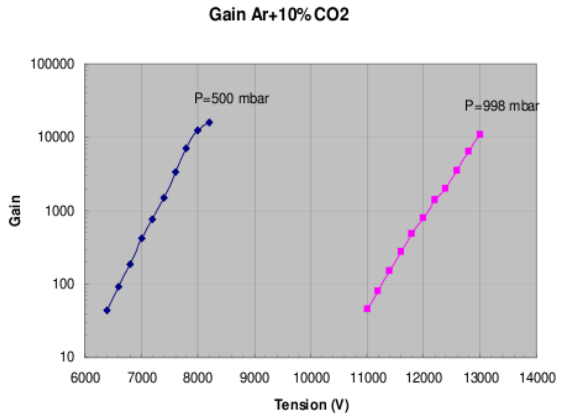

Figure 2.11: Effective gas gain versus high voltage for various pressures in Ar + 10% CO_2.

ation was tested up to 40 days, without gas circulation (seal mode). Runs using calibration sources of ^{109}Cd and ^{55}Fe or cosmic rays have been also performed. A typical detector response at 22 keV in Ar + 10% CO_2 gas, from a ^{109}Cd source, is shown in Fig. 2.12. High gain combined with low electronic noise provides low energy threshold. At low electric fields (E) the drift velocity is roughly proportional to E and the longitudinal diffusion coefficient (D) is inversely proportional to the square of E. So the time dispersion is correlated to the cube of the radius. So there is an information contained in the signal that is correlated to the radial distance of the interaction. By measuring the time dispersion of the signal with a deconvolution method one can find with a precision of about 10 cm, especially at large distances, the depth of the interaction as shown on Figure 2.13.

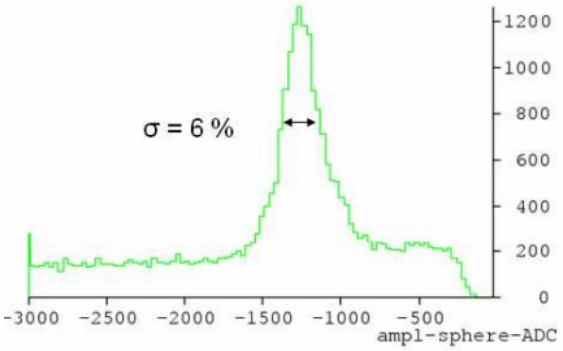

Figure 2.12: Pulse height distribution of the signal produced by a ^{109}Cd source.

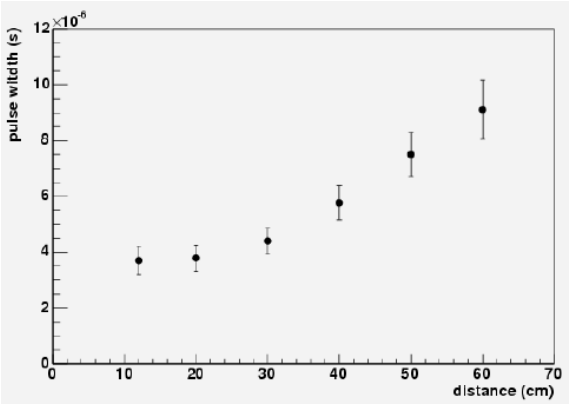

Figure 2.13: Time dispersion of the signal as function of the depth of interaction.

2.6 Results with a field corrector

To solve the problem of field distortion due to voltage anode electrode one needs to add one or more electrodes to the system, in order to correct the field lines towards an electrostatic configuration which:

1. approaches more an ideal spherical symmetry
2. makes all (or most) of the field lines end up in the spherical electrode, and not in the rod
3. the amplification associated with each of those field lines is sufficiently similar, so the detector response is homogeneous over the whole volume. It will be shown later that 1 is probably not easy to achieve together with 2 and 3, and that achieving 2 and 3 relaxing 1 is certainly possible keeping the robustness and simplicity of the original concept, and an interesting option for many applications.

Several practical geometries have been tried to accomplish such objectives. The additional elements have been one of more of the following: annular electrodes

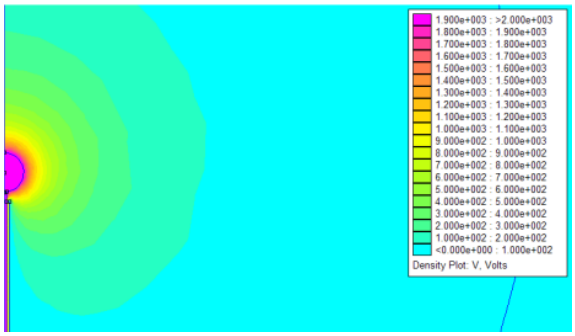

Figure 2.14: Electrostatic configuration for the readout electrode, with the "corrector" electrode consisting of a grounded cylinder surrounding the high voltage rod and placed 4 mm away from the spherical electrode [34].

placed along the rod at different voltages, a conical piece of resistive material placed under a voltage drop at the end of the rod or one or more concentric cylindrical electrodes placed around the rod at different voltages and at different distances from the sphere. Although all tested solutions are valid in theory, the selection of the preferred one is done by practical and technical issues, in particular, the ease of construction or the absence of sparking when going to higher voltages. In this sense, the more successful configuration, (and the one with which we have obtained the results presented) is the one with a cylinder around the high voltage rod, placed at 4 *mm* away from the central sphere and powered with an independent voltage V_2 (which can be zero, i.e., at ground). The equipotential lines for the described "corrected" configuration are shown in Figure 2.14.

As can be seen, the presence of the cylinder at ground twists the field lines around the spherical electrode in a way that makes them more spherically symmetric than before. Nevertheless, a closer inspection to the region close to the electrode surface still shows differences, especially near the connection to the rod. However, the relevant feature of the proposed geometry, which is responsible of its success of operation, is illustrated in Figure 2.15,where the corresponding field lines are drawn. As can be seen, the presence of the cylinder at ground pushes the field lines away, focusing most of them in a "constrained" region of the spherical electrode, the one opposite the rod (where the amplification happens to be more homogeneous). What could be seen as an unpleasant feature, away from the spherical symmetry, is however a positive one, as the amplification suffered along electron path is rather similar making the detector response remarkably homogeneous for most of the detector volume. These facts have been proved by the experimental measurement of the energy resolution for a gaseous source (radon) homogeneously active over the full detector volume, as shown in Figure

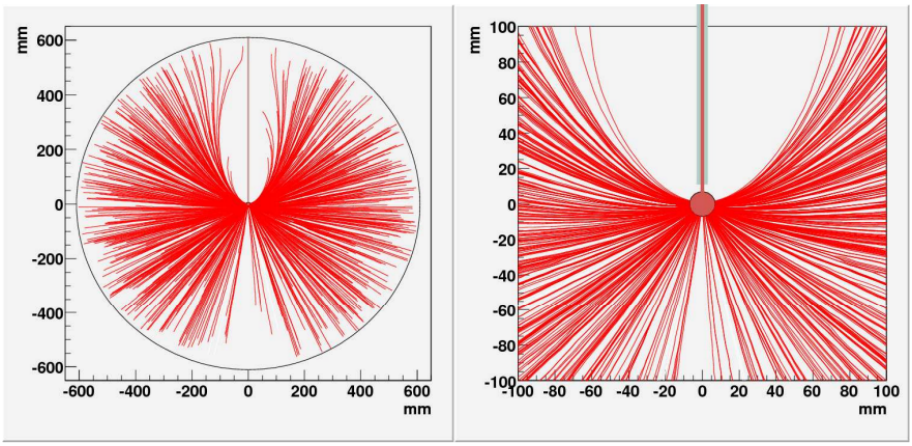

Figure 2.15: Drift field lines for the geometry with the cylinder at ground. The lines have been calculated starting form 1000 points randomly distributed over the sphere volume. In this case all lines end up on the spherical electrode, and are pushed away from the conflictive region of the connection sphere-stick. Left one shows the overall picture and right a close-up of the 10 *cm* around the center.

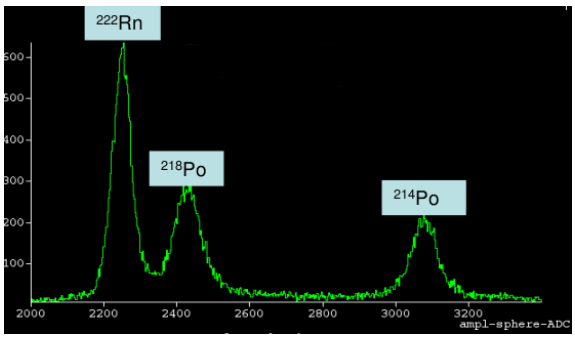

Figure 2.16: Peaks observed from a ^{222}Rn radioactive source. From left to right we observe the ^{222}Rn peak at 5 MeV, the ^{218}Po and ^{214}Po at 6 MeV and 7.7 MeV respectively [7].

2.16; a good energy resolution of 0.5% has been achieved. The remarkable results achieved show that this extremely simple and robust readout configuration is a very appealing working option for cases where perfect radial drift lines are not required [5].

2.6.1 Ultra low energy results

The results obtained for relatively high energies point out the excellent energy resolution obtained with radon nuclide and its daughters. Now we will focus our attention to the detection of very-low energy gamma or X-rays emitted by radioactive sources or fluorescence process. For this study the gas filling used was Argon

with 2% admixture of CH_4 at various pressures. The pressure (P in *mbar*), the high voltage of the ball (HV1 in V), the high voltage of the umbrella field corrector (HV2 in V) and the gain (G) of the amplifier-shaper in all measurements in the section, are written in the top-right box on each of the following figures. Calibration of the counter was initially performed using a ^{109}Cd source by irradiating the gaseous volume through a thin 200 μm aluminum window. Fig. 2.17 shows the energy

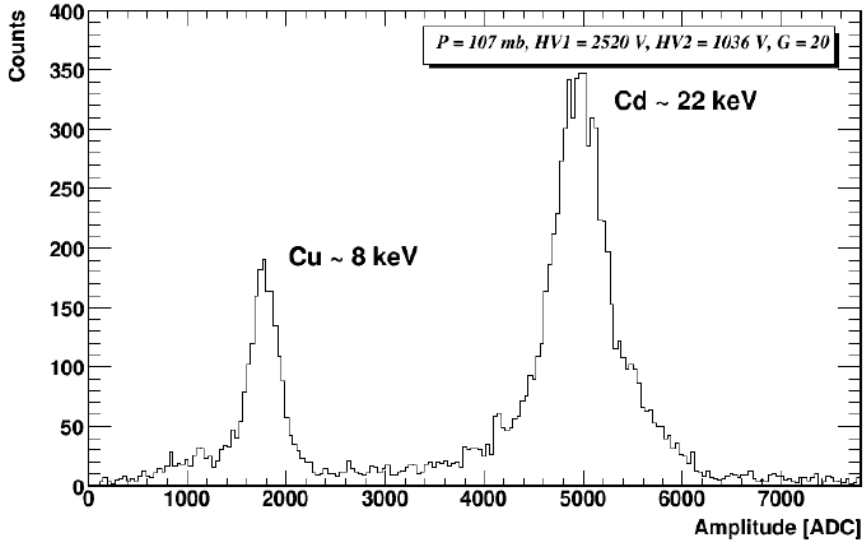

Figure 2.17: The spectrum of the ^{109}Cd source with the energy lines of 8 and 22 keV respectively.

spectrum with the 22 keV line from the ^{109}Cd source and the 8 keV line, which is an induced fluorescence at the copper vessel. The energy resolution is quite satisfactory 6% and 9% (FWHM) respectively. Gamma fluorescence is adequate for producing fluorescence lines in the range above several keV. However, it is very difficult to produce low energy calibration lines below a few keV. In order to create lower energy X-rays we have used an ^{241}Am source, which decays by the following process: $^{241}Am \rightarrow {}^{237}Np + {}^{4}He + 5.6\ MeV$. The ^{237}Np nucleus then decays into a lower energy state by emitting a $59.537 keV$ gamma ray and other L rays , which are used to fluoresce the elements. The source was evaporated to a stainless steel holder and attached to the sensor rod at middle distance; the source then is covered by thin foils with adequate thickness to totally absorb the 5.6 MeV alpha emitted, leaving only gamma rays and fluorescence induced X-rays to pass into the gas volume.

Covering the source with a 20 μm thick aluminum foil we were able to fluoresce the K X-rays ranging from Aluminum whose K electron has a binding energy of 1.56 keV, to Cu whose K electron has a binding energy of 8.98 keV. Fig. 2.18 shows the obtained low energy spectrum. From left to right we observe the aluminum

line (1.45 keV), the iron line (6.4 keV), the copper line (8.0 keV) and two lines emitted by ^{237}Np nucleus at 13.93 keV (X-ray $L\alpha$) and 17.6 keV (X-ray $L\beta$). By increasing the gain of the amplifier 5 times and adjusting its settings, we were able to push the higher part of the spectrum outside the ADC range and keep in the ADC acceptance only the aluminum 1.45 keV peak as shown in Fig. 2.19. The energy threshold is clearly below 100 eV and the low energy background level is flat. In order to obtain even lower energy calibration lines we replaced the aluminum foil by a thinner 10 μm one and we attached a 20 μm polypropylene foil. Therefore, the alpha particle that is crossing the aluminum foil, is fully absorbed by the polypropylene foil and induces both aluminum and carbon fluorescence as shown in Fig. 2.20.

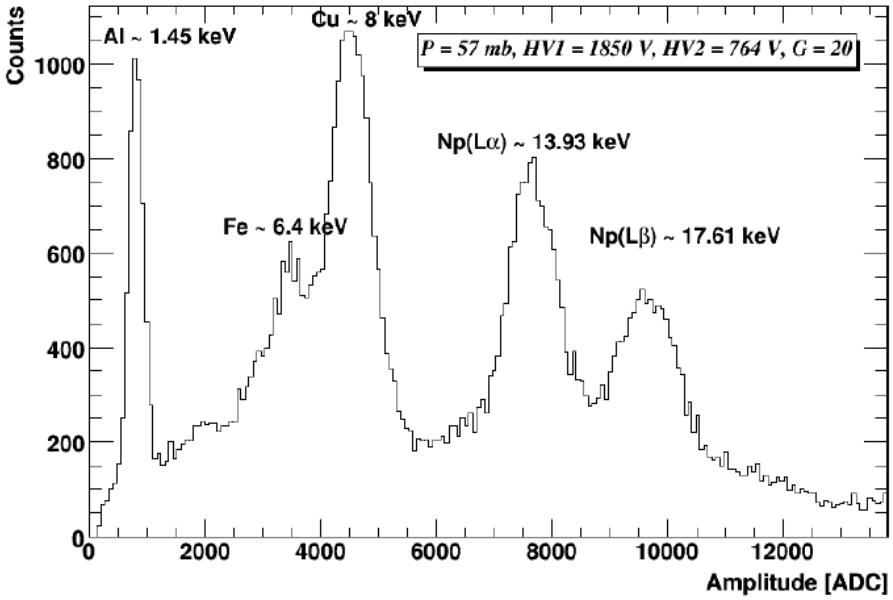

Figure 2.18: Peaks observed from the ^{241}Am radioactive source. From left to right we observe the Aluminium, Iron and Copper peaks followed by the Neptunium peaks.

By increasing the gain of the amplifier by a factor of 5, we are able to push the higher part of the spectrum outside the ADC range and keep in the ADC acceptance only the Carbon 270 eV peak as well as the Aluminum (1.45 keV) as shown in Fig. 2.21. High gain combined with low electronic noise can provide energy thresholds clearly below 100 eV. Fig. 2.22 shows the energy spectra at different gains of the amplifier when no source is used. By applying a cut at the rise time of the signal (which actually provides the depth of the ionized electrons produced in the gas) we can exclude the signal induced by cosmic rays and measure only the Copper energy line of 8 keV (plotted with dashed line in Fig. 2.22). Then, by

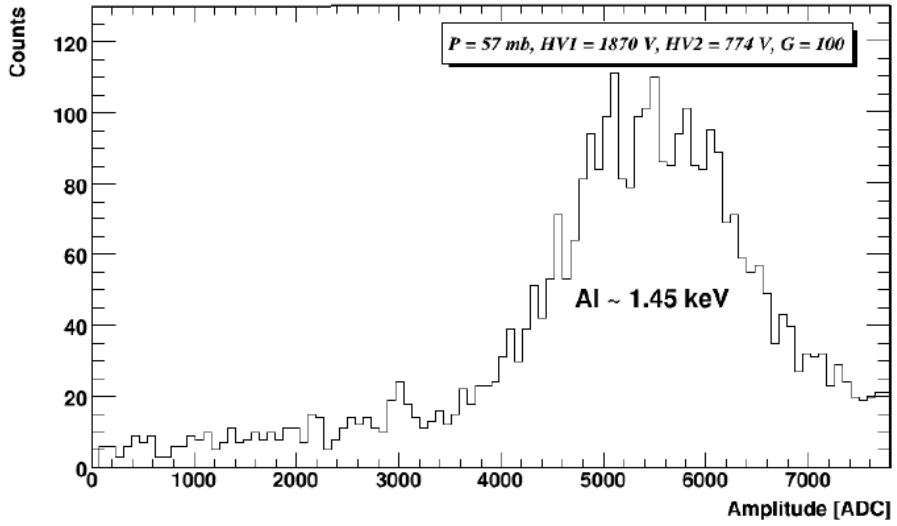

Figure 2.19: An X-ray spectrum showing its characteristic Aluminum K X-ray energy peak.

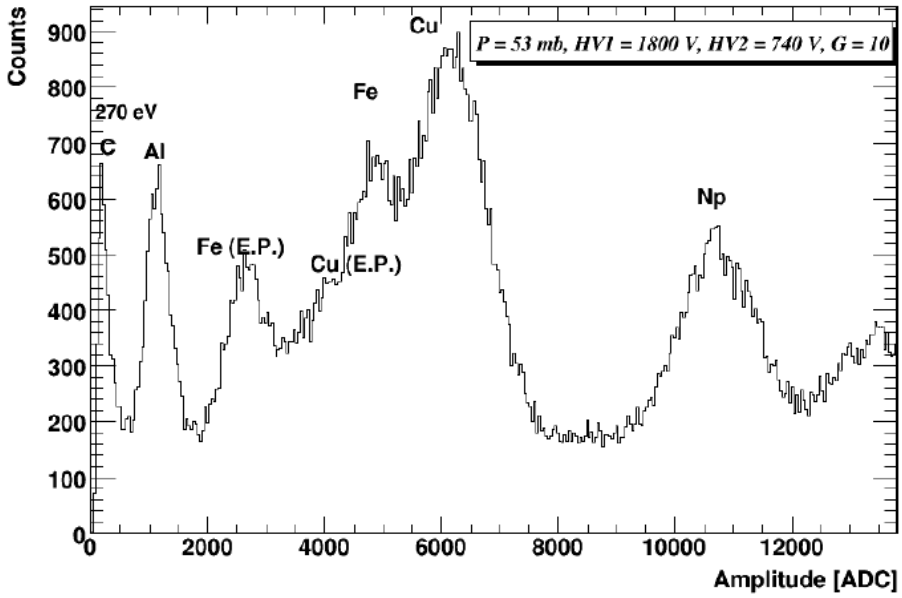

Figure 2.20: Peaks observed from the ^{241}Am radioactive source through aluminium and polypropylene foil. On the left the Carbon (270 eV) peak is shown, followed by the Aluminium peak (1.45 keV), the escape peak (E.P.) of Iron in Argon (3.3 keV), the escape peak of Copper in Argon (5 keV), the Iron peak (6.4 keV), the Copper peak (8 keV) and the Neptunium peak (13.93 keV).

increasing the gain of the amplifier 20 times (from Gain = 10 to Gain =200), we keep in the ADC acceptance only the ultra low energy region (plotted with full line in Fig. 2.22). The value of 1000 ADC corresponds to ~ 150 eV and the peak at

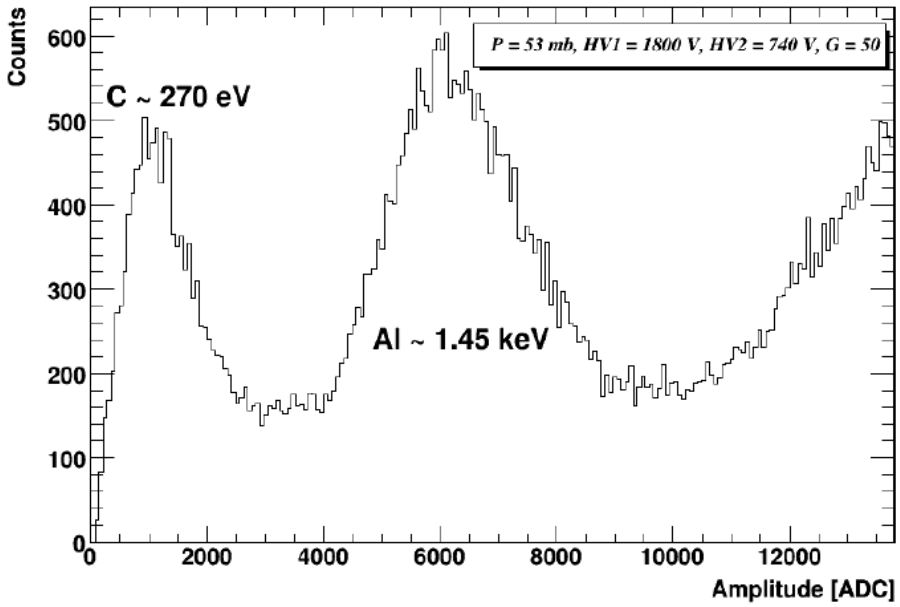

Figure 2.21: From left the Carbon (270 *eV*) peak followed by the Aluminum peak (1.45 *keV*).

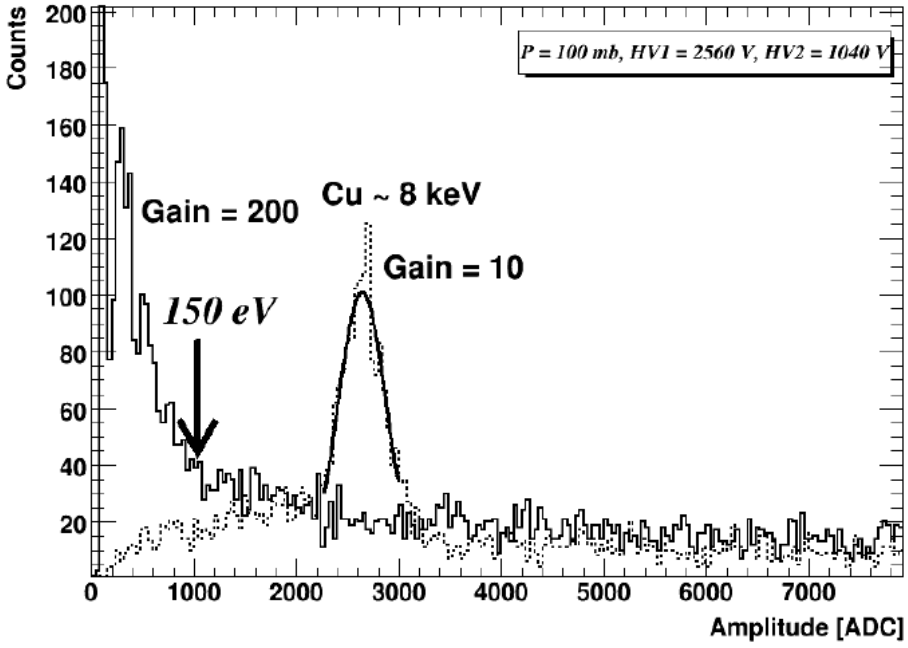

Figure 2.22: The energy spectrum at Gain = 10 with the Copper peak of 8 *keV* (dashed line) and at Gain = 200 where the single electron peak at ~50 *eV* is clearly visible (full line).

~ 50 *eV* is compatible with single electrons. Thus, the detection threshold of the Spherical Proportional Counter is as low as 25 *eV*. From ~ 750 *eV* to 1200 *eV* the energy spectrum looks flat (Fig. 2.22 - full line). At energies lower than ~ 750 *eV*,

an increase of the slope of the energy spectrum is observed and is followed by a steer rise at very low energies. The exponential shape of the spectrum has to be confirmed by underground measurements which are on-going [1].

2.7 Advantages of the Spherical Proportinal Counter

The Spherical Proportional Counter, recently developed, is a novel concept with very promising features, among which is the possibility of easily instrumenting large target masses with good energy resolution and low energy threshold. The natural radial focusing of the spherical geometry allows collecting and amplifying the deposited charges by a simple and robust detector using a single electronic channel to read out a large gaseous volume. Moreover the detector is robust and stable in time. Unlike in the conventional TPC special field cage is not needed.

The amplification process is similar to other commonly used gaseous detectors: the Parallel Plate Avalanche Chamber (PPAC) and the cylindrical proportional counter. Let us compare the three concepts in terms of electric field shape relevant for signal development and capacity relevant for electronic noise: In the PPAC the electric field is constant and the capacity is given by $C = \varepsilon_0 S/d$ where S is the detector surface and d is the thickness of the amplification gap. For large detectors ($> 1\ m^2$) the capacity, proportional to the surface, will exceed $10\ nF$.

In the cylindrical proportional counter the electric field is given by $E = V_0/r$ where V_0 is the applied voltage and r is the radius of the sense wire. The capacity is given by $C = \varepsilon_0 L \log(r/R)$ where L is the length of the sense wire and R the external radius; for large detectors we get $C > 100\ pF$.

In the spherical proportional counter the electric field at a distance r is given by:

$$E(r) = \frac{V_0}{r^2} \frac{1}{1/r_2 - 1/r_1} \tag{2.12}$$

where r_2 is the anode radius, r_1 cathode radius and V_0 the anode voltage. The capacity is given by:

$$C = \frac{4\pi\varepsilon_0}{1/r_2 - 1/r_1} \tag{2.13}$$

and since ($r_1 >> r_2$) $C = 4\pi\varepsilon_0 r_2$. For a typical size of $r_2 = 6\ mm$ the capacity is $C = 0.05\ pF$ [4].Such low capacity will provide a very low electronic noise and therefore low energy threshold even if the detector operates at moderate gains. Notice also that the capacity depends only on the size of the ball radius and is roughly independent of the vessel volume. So we can summarize main advantages of the SPC as follows:

- The spherical geometry naturally focuses a large drift volume into a small amplifying detector with only a few (or even just one) read-out channels. It is the most cost-effective way of instrumenting a large detector volume with a minimum of front-end electronics. Such approach simplifies the construction and reduces the cost of the project.

- Spherical symmetry minimizes the external surfaces per unit of detector volume, as well as the thickness of material needed to hold the gas, therefore allowing a lower background per unit volume due to external surface or material contaminations. In principle, the simplicity of its design should allow an easy optimization from the point of view of radiopurity. Work is in progress to evaluate expected sources of backgrounds as well as to design a radiopure version of the present prototype.

- Large drift volumes can be built without the use of a field cage, unlike cylindrical TPCs. The spherical symmetry means that the detector capacity is very low, allowing for extremely low levels of electronic noise. Keeping in mind that no special measure has been taken for reducing electronic noise, the prospects to achieve thresholds well below 100 eV are realistic [3].

Chapter 3

Neutrino sources

3.1 Artificial and Natural neutrino sources

In the various phenomena where the neutrinos show up, their spectrum includes energies from a few MeV to hundred TeV. Depending the energy they carry, neutrinos are classified into :

1. low energy neutrinos, $E_\nu \preceq 20-30\ MeV$ (solar and low energy supernova neutrinos)

2. intermediate energy neutrinos, $20 \preceq E_\nu \leq 100-150\ MeV$ (high energy supernova neutrinos)

3. high energy neutrinos, $100\ MeV \leq E_\nu \preceq 1-2\ GeV$(atmospheric neutrinos, solar flair neutrinos, γ-ray bursts neutrinos, e.t.c)

Here we refer only to the low and intermediate energies neutrinos where the nucleic degrees of freedom are not excited, and so, the transfer energy from the neutrino-nucleus reaction, changes only the kinetic energy of the nucleus. The properties and the part of the neutrinos are studied in modern research combined with the characteristics of their production sources, which depending on their energy and their production mechanisms, are classified into artificial and astrophysical sources of neutrinos.

3.1.1 Artificial sources of neutrinos

Laboratory low energy neutrino beams

The low and intermediate energy neutrinos produced at various experiments, as, *MiniBoone*, β*-beams*, etc., aren't monoenergetic but present an energy distribution, examples of such neutrino energy distributions are:

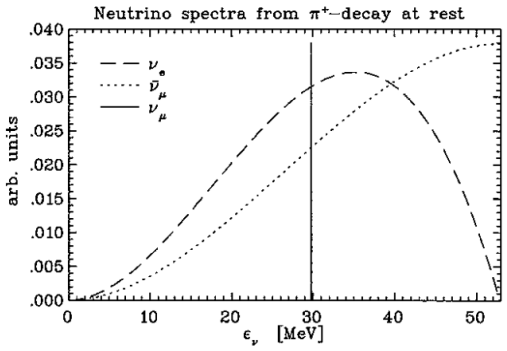

Figure 3.1: Neutrino energy distribution, produce by the decay of slow pions (π^+) and muons (μ^+). The maximum energy of neutrinos coming from pions is $52.8\ MeV$.

1. Neutrinos produced by slow pion and muon decay, with energies, $E_\nu \preceq 52.8\ MeV$.

2. Reactor neutrinos, which are $\bar{\nu}_e$ antineutrinos and are produced during the β-decay of nuclei reach in neutrons (^{235}U,^{238}U,^{239}Pn,^{240}Pn). These neutrinos are detected through the inverse β-decay and have energies $E_\nu \preceq 10\ MeV$

3. β-beam neutrinos, which are produced during the β-decay of nuclei accelerated inside storing rings and have energies, $E_\nu \preceq 1-2\ GeV$.

During the decay of slow pions and muons, mainly muon neutrinos ν_μ and anti-neutrinos $\bar{\nu}_\mu$ are produced, but also electron neutrinos ν_e or anti-neutrinos $\bar{\nu}_e$. When the muons come from slow pions according to the reactions,

$$\pi^\pm \to \mu^\pm + \nu_\mu(\bar{\nu_\mu}) \tag{3.1}$$

$$\pi^\pm \to e^\pm + \nu_e(\bar{\nu}_e) \tag{3.2}$$

they have relatively low energy $E_\mu \leq 29.8\ MeV$ Figure 3.1. Thus, during the decay of muons in flight, we have a beam of

$$\mu^+ \to e^+ + \nu_e + \bar{\nu}_\mu \tag{3.3}$$

$$\mu^- \to e^- + \bar{\nu}_e + \nu_\mu \tag{3.4}$$

with energies of the ν_e neutrinos $E_{\nu_e} \preceq 52.8\ MeV$. With the capture of the positive pions (π^+) or the negative pions (π^-), we can succeed at knowing the exact neutrino distribution of the produced beam. The energy spectrums of the ν_e and $\bar{\nu}_\mu$ that are produced according to the reaction (3.3), are described approximately by the normalized distributions,

$$f_{\nu_e}(E_{\nu_e}) = 96E_{\nu^e}^2 m_\mu^{-4}(m_\mu - 2E_{\nu_e}) \tag{3.5}$$

$$f_{\bar{\nu_\mu}}(E_{\bar{\nu_\mu}}) = 16E^2_{\bar{\nu}\mu} m_\mu^{-4}(m_\mu - 4E_{\bar{\nu_\mu}}) \tag{3.6}$$

which come from fitting experimental data and are visualized at Figure 3.1. At the above expressions, $m_\mu = 105.6\ MeV$, and represents the muon mass. The maximum energy of the ν_e at the eq. (3.60) is $E^{max}_{\nu_e} = 52.8\ MeV$, while the $\bar{\nu}_\mu$ one given at the eq. (3.61) , is $E^{max}_{\nu_e} \leq 79.2\ MeV$.

It worths mentioning that the energy distributions of the eq.(3.60),(3.61), have been used to describe the Supernova neutrinos because their shapes are quite similar with that of the Supernova neutrinos. The drawback is the fact, that the tail of high energies ($E_\nu \approx 50 - 80\ MeV$), is closed, in contrast with the one of the spectrum of the Supernova neutrinos.

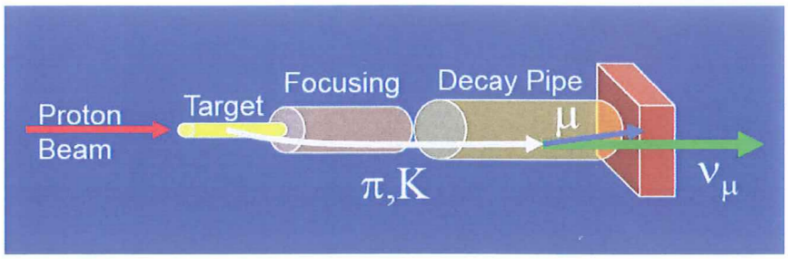

Figure 3.2: Schematic presentation of the experimental set up for the production of muon neutrinos (anti-neutrinos). We can distinguish the proton beam, the Beryllium target where the pions and kaons are produced, the decay pipe of muons and the production area of neutrinos.

Artificial neutrino beams at high energy

At the modern accelerators, with the use of high energy proton beams Fig. 3.2, high energies neutrino beams can be produced (accelerator neutrinos). Such neutrino beams, are powerful, focused and clean enough, so that they can be directed to a laboratory placed near by (short baseline neutrinos) or far away (long baseline neutrinos) the place of their production. This beams, usually are consisted of muon neutrinos or antineutrinos, with a small admixture of electron neutrinos or antineutrinos. In our days, the technological evolution gave us neutrino beams from accelerated β-radioactive nuclei, with energies of $E_\nu < 100\ MeV - 2\ GeV$.

Conventional and Superbeams of neutrinos

At the large storage rings, where its possible for 10^{20} muons per year to be captured, it is possible to produce very powerful beams of neutrinos and antineutrinos. The conventional neutrino beams, are in fact muon neutrino beams ν_μ, with a small admixture (less than 1%) from neutrino of other flavors . The admixture

from ν_e neutrinos of the beam, is limiting the experimental efforts to observe the appearance ν_e neutrinos coming from the oscillations (*MiniBooNE* experiment at Fermilab) of the neutrinos and therefore to count the mixing angle θ_{13} (*MINOS* experiment). For the production of conventional neutrino beams, a beam of high energy protons is directed on a target (at the *MiniBooNE* experiment the target is Beryllium), in which case the generated positive pions (π^+) are collected, focused and finally decay in a long tube Fig.3.2. After the decay, we have a relatively focused beam of ν_μ neutrinos. A muon antineutrino beam is produced $\bar{\nu}_\mu$ when negative charges pions (π^-) are focused at the beam. The neutrino fluxes are parametrized by the number of protons incident at the target per year (POT). The conventional sources have 10^{20} POT.

Neutrino Superbeams are the technological evolution of the conventional beams. The neutrinos of the superbeam, are generated by making use of the modern technology for the production of fine beams, meaning that their energy spectrum has one very high peak. The neutrino flux at the superbeams is greater by a factor of 10 to 50 in comparison with the conventional beams and their power is approximately 10^{21} POT.

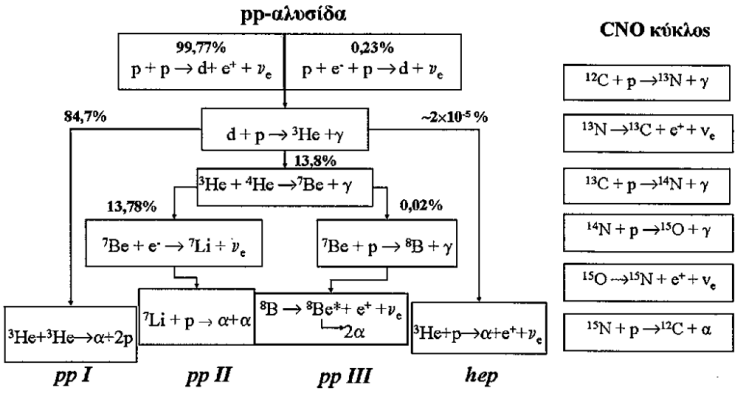

Figure 3.3: Thermonuclear neutrino producing reactions, which take place at the interior of the Sun: *pp*-reaction chain (left) and the main reactions which are includes in the *CNO* cycle (right).

3.1.2 Natural neutrino sources

Solar Neutrinos and their production reactions

In the interior of the Sun, are produced ν_e neutrinos (solar neutrinos), with energies $E_\nu < 20MeV$, through the thermonuclear reactions taking place mainly during the burning of the Hydrogen. Overall, the burning of the hydrogen is described

by the reaction

$$4p \rightarrow {}^4He + 2e^+ + 2\nu_e + 26.731\ MeV \tag{3.7}$$

Individual reactions (sources) of solar neutrinos, through the pp-chain process, are the pp-neutrinos, the pep-neutrinos, the hep-neutrinos, the ${}^7Be$-neutrinos, whereas the production reactions through the CNO-cycle, are shown at Fig.3.3.

The research field of neutrino astrophysics, was created by the effort to count the flux of the solar neutrinos at the *Homestake* experiment at the end of the decade of 1960. Three decades after, the relative research (*SuperKamiokande*, *SAGE*, *GALLEX SNO*, etc experiments) succeeding in having today accurate measurements, not only for the total solar neutrino flux, but also for the individual components of neutrino flavors. That was an important testing of the theory of evolution of stars of the main sequence and also the measurement of the square difference of the mass $|\Delta m|^2_{atm}$, $|\Delta m|^2_{solar}$, of the different neutrino mass eigenstates, as well as the mixing angles θ_{23} and θ_{12}.

Recent data, which are suggest an important decrease of the metalicity of the Sun to a point that it is no longer considered rich in heavy elements, and consequently meaning that we a have a decreased flux of solar neutrinos, due to the decrease of the heart's temperature. But, because the neutrinos of the CNO cycle have a greater dependence from the heart's temperature , a better measurement of the flux of the CNO neutrinos is expected to give a better understanding of the metalicity of the Sun (SNO^+ experiment).

Atmospheric neutrinos and their reactions

It a known fact that the Earth is immersed in a flux of high energy comic rays, which is consisted mainly from protons and α-particles. At the upper layers of the atmosphere, these particles are decelerated and lose energy, generating mainly pions $\pi^{\pm}$ and a few kaons K^{pm},K^0, which decay, producing neutrinos (with energies $E_\nu \preceq 1-3\ GeV$ through the reactions

$$\pi^{\pm}(K^{\pm}) \rightarrow \mu^{\pm} + \nu_\mu(\bar{\nu}_\mu) \tag{3.8}$$

$$\mu^{\pm} \rightarrow e^{\pm} + \nu_e(\bar{\nu}_e) + \bar{\nu}_\mu(\nu_\mu) \tag{3.9}$$

The neutrino-nucleus reactions, are very usefull for the detection of atmospheric neutrinos, as well for the study of their production reactions. At the experiment of atmospheric neutrinos, the characteristics of the nuclear structure are usefull for the simulations of the modern detectors and the choice of the appropriate target-nucleus. Today, there are extended measurements of atmospheric neutrinos.

One of the biggest problems that concerned for decades the scientific community, the so called atmospheric neutrino anomaly, which is express as such: from

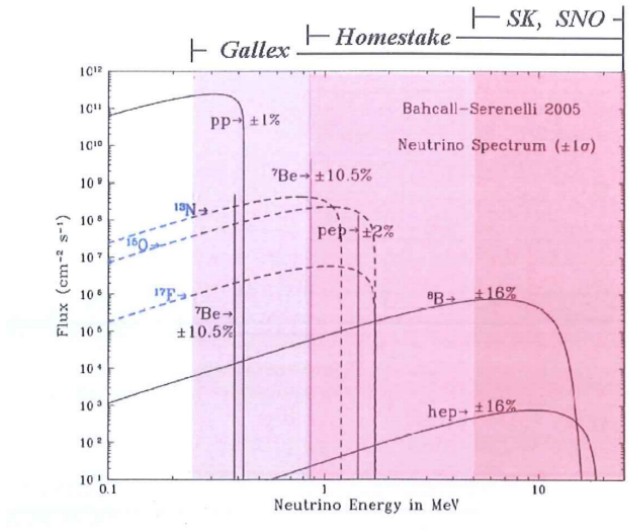

Figure 3.4: Solar neutrino fluxes which are produced by the thermonuclear reactions taking place at the interior of the Sun, as functions of the neutrino energy. The flux from the *pp*-reactions chain, as well as the flux from the *CNO* cycle are presented. The shaded surfaces show the threshold energy and the measured fluxes of solar neutrinos from known experiments.

the decay reactions (3.1) and (3.2), one would expect the ratio of the two neutrino flavors, ν_μ and ν_e and their antiparticles which is given by the expression

$$r = \frac{\nu_\mu + \bar{\nu}_\mu}{\nu_e + \bar{\nu}_e} \tag{3.10}$$

to be equal to 2. However, experimental measurements had shown that, the ratio is equal to $r \approx 1.2$, results that have been confirmed from the charged current neutrino nucleus reactions, of the type (ν_μ,μ^-) and (ν_e,e^-) at the laboratories *IMB*, *Kamiokande*, and *SuperKamiokande*. The above ambiguity means that, either a decrease of the muon neutrinos exists or an increment of the electron neutrinos or both facts and the same time.

For the explanation of the above anomaly, many theoretical explanations where developed, including the widely accepted assumption of the existence of neutrino flavors oscillation, which results in a reduced flux of the ν_e.

According to recent measurements for the atmospheric neutrinos from SuperKamiokande, the dependence of the ratio L/E_ν, where L is the distance that a neutrino covers at the void and E_ν its energy, the ν_{mu} neutrinos can be explained by their conversion into ν_τ. One crucial point that must mentioned, is the fact that, the atmospheric neutrino anomaly means a large mixing angle of the neutrinos. Today we know from measurements of atmospheric neutrinos that

$|\Delta m|^2_{21} = (7.65^{+0.23}_{-0.20}) \times 10^{-5}(eV)^2$ and $|\Delta m|^2_{23} = (2.4^{+0.23}_{-0.20}) \times 10^{-3}(eV)^2$ (*KamLand* experiment.

Cosmological Neutrinos

The neutrino research today, considers that, a low energy neutrino background exists in the Universe, like the cosmic microwave background radiation (*CBM*), which was created at the moment of the Big Bang and its called cosmic neutrino background (*CνB*). At the decade of 1980, it was proposed that this neutrinos could explain the dark matter in the Universe, because they have important advantages in comparison with other dark matter candidates, in that we know their existence, they are consider massless, and they have the same number density like the photons of the *CBM* radiation, according to the Standard Model of particle physics.

From relic neutrinos detected in the cosmic background radiation, is concluded that the neutrinos played and still play prominent role at the procedures of the Big Bang.

The neutrino is the second more abundant particle in the universe after the photons of the cosmic background radiation. Today it is believed that, their total number density, including and the antineutrinos, is

$$\sum(n_\nu + n_{\bar{\nu}}) \approx 340 \quad neutrinos/cm^3 \tag{3.11}$$

almost equally divided among the three types ν_e, ν_μ, ν_τ.

For comparison, the mean number density of the common baryonic matter, is $n_B \approx 2.5 \times 10^{-7} \quad baryons/cm^3$. The neutrino background of the universe is not directly observable today, because of the very weak interaction of this neutrinos which have very low energy. The mean value of the *CνB*, is $E_\nu = 6.1^\circ K \approx 5.3 \times 10^{-4}\, eV$. Cosmological data analysis, allows to be placed an upper limit to neutrino mas, that is $\sum m_\nu \preceq 0.7\ MeV$, from which it results $m_\nu \leq 0.23\ eV$ (assuming equal number of every flavor).

We note that, the *KATRIN* experiment, is expected either to put an upper limit to the neutrino mass at the value of $m_\nu \leq 1\ eV$, or to measure one important mass value at the region of $0.2\ eV \preceq \mu_\nu \preceq 1\ eV$.

Geoneutrinos

The antineutrinos produced, mainly, during the β-decays of the natural and artificial radioactive isotopes of the Earth ($E_\nu < 10\ MeV$), as the U, Th and ^{40}K, are known by the term geoneutrinos and carry informations about the abundance of the radioactive elements from the entire planet and its thermal evolution. Their

detection, can shed light at the explanation of the sources of the earths thermal flux, its current composition as well the origin of the Earth. The first measurement of the geoneutrinos, was made by the scintillator *KamLAND*, through the inverse β-decay

$$\bar{\nu}_e + p \rightarrow e^+ + n \tag{3.12}$$

The main advantage of the pioneering result of *KamLAND*, is a proof that the geoneutrinos can be detected, opening the road for the development of a new research field the geo-science. The research object of the geoneutrinos is one of the future goals, of other scintillators too (SNO^+,*LENA*,*HANOHANO*,*EARTH*,etc).

Astrophysical neutrinos of very high energy

The neutrino astronomy of very high energy branch i.e neutrinos from γ-ray bursts, is in a very primary stage. Future experiments aim to the observation of neutrinos of very high energy from our galaxy, are the *Baikal*, the *AMANDA*, the *ICECUBE*, the *Antares*, the *NEMO* and the *Nestor*. Relative informations are provided by the high energy γ-ray bursts telescopes, like *HESS*,*MAGIC*,etc.

Supernova neutrinos

The supernova neutrinos (SN-neutrinos), have energies $E_\nu < 60 - 80\ MeV$ and are produced at the latter stage of a massive star's life (mass $5 - 8\ M_\odot \leq M \leq 22 - 25\ M_\odot$). Because the SN-neutrinos are an important part of these study we will discuss about their properties more extensively at following parts [22].

3.2 Neutrino-Nucleus interaction

3.2.1 Elastic neutrino nucleon scattering

Kinematics of the neutrino nucleus scattering

Before we can calculate the cross section of the neutrino nucleus elastic scattering one must know the kinematic parameters of the reaction

$$\nu + (A,Z) \rightarrow \nu' + (A,Z)' \tag{3.13}$$

Because neutrinos are elementary particles is necessary to describe their kinematic using relativity. We consider the scattering of a neutrino with a four-vector momentum p from a nucleus of four-vector momentum P. The conservation of

energy and momentum dictates that the sums of the momentum four-vectors will be equal before and after the collision

$$p + P = p' + P' \tag{3.14}$$

or their square

$$p^2 + 2pP + p^2 = p'^2 + 2p'P' + P'^2 \tag{3.15}$$

At the elastic scattering the masses of the scattered particles remain the same

$$p^2 = p'^2 = m^2c^2 \tag{3.16}$$

and

$$P^2 = P'^2 = M^2c^2 \tag{3.17}$$

which lead to

$$p \cdot P = p' \cdot P' \ . \tag{3.18}$$

and by using equations (3.14),(3.15) we get

$$p \cdot P = p' \cdot (p + P - p') = p'p + p'P - m^2c^2 \tag{3.19}$$

At the lab system the nucleus with four-vector momentum P is at rest before the collision. The four vector momentum can be written as

$$p = (E/c, \vec{p}), p' = (E'/c, \vec{p'}), P = (Mc, 0), P' = (E'_P/c, \vec{P'}) \ . \tag{3.20}$$

So the eq.(3.15) is written as

$$E \cdot M = E'E - \vec{p}\vec{p}\,' + E'Mc^2 \ . \tag{3.21}$$

where $E \approx |\vec{p}| \cdot c$. Now we have a relation between the angle of scattering and the energy E

$$E \cdot M = E'E(1 - \cos(\theta)) + E' \cdot M \ . \tag{3.22}$$

At the lab system the energy of the scattered neutrino is

$$E' = \frac{E}{1 + E/M \cdot (1 - \cos(\theta_\nu)} \tag{3.23}$$

where θ_ν is the neutrino scattering angle. The recoil energy that is transferred at the target is given by the difference of the energies $E - E'$ [21].

The other kinematic variables are functions of the recoil kinetic energy of the nucleus, T_A,

$$\cos(\theta_A) = \frac{E_\nu + M_A}{E_\nu} \sqrt{\frac{T_A}{T_A + 2M_A}} \approx \sqrt{\frac{M_A T_A^2}{2E_\nu}} \tag{3.24}$$

$$\cos(\theta_\nu) = 1 - \frac{M_A T_A}{E_\nu(E_\nu - T_A)} \approx 1 - \frac{M_A T_A}{E_\nu^2} \tag{3.25}$$

Differential cross section of an elastic neutrino nucleon scattering

The cross section for elastic neutrino nucleon scattering has extensively been studied. It has been shown that at low energies it can be simplified and be cast in the form:

$$\left(\frac{d\sigma}{dT_N}\right)_{weak} = \frac{G_F^2 m_N}{2\pi}[(g_V+g_A)^2+(g_V-g_A)^2[1-\frac{T_N}{E_\nu}]^2+(g_A^2-g_V^2)\frac{m_N T_N}{E_\nu^2}] \quad (3.26)$$

where m_N is the nucleon mass, T_N its energy and g_V , g_A are the weak coupling constants. Neglecting their dependence on the momentum transfer to the nucleon they take the form:

$$g_V = -2\sin^2\theta_W + 1/2 \approx 0.04 \quad , \quad g_A = \frac{1.27}{2} \ , \qquad (\nu, p) \quad (3.27)$$

$$g_V = -1/2 \quad , \quad g_A = -\frac{1.27}{2} \ , \qquad (\nu, n) \quad (3.28)$$

In the above expressions for the axial current the renormalization in going from the quark to the nucleon level was taken into account. For antineutrinos $g_A \to -g_A$. To set the scale we write:

$$\frac{G_F^2 m_N}{2\pi} = 5.14^{-41}\ \frac{cm^2}{MeV} \quad (3.29)$$

The nucleon energy depends on the neutrino energy and the scattering angle, the angle between the direction of the recoiling particle and that of the incident neutrino. In the laboratory frame it is given by:

$$T_N = \frac{2m_N(E_\nu\cos\theta)^2}{(m_N+E_\nu)^2-(E_\nu\cos\theta)^2} \ , \qquad 0 \le \theta \le \pi/2 \quad (3.30)$$

(forward scattering). For sufficiently small neutrino energies, the last equation can be simplified as follows:

$$T_N \approx \frac{2(E_\nu\cos\theta)^2}{m_N} \quad (3.31)$$

The above formula can be generalized to any target and can be written in dimensionless form as follows:

$$y = \frac{2\cos^2\theta}{(1+1/x_\nu)^2-\cos^2\theta} \quad , \quad y = \frac{T_{recoil}}{m_{recoil}} \ , \ x_\nu = \frac{E_\nu}{m_{recoil}} \quad (3.32)$$

In the present calculation we will treat x_ν and $y-\nu$ as dynamical variables, in line with *CDM* recoils. One, of course, equally well could have chosen x_ν and θ as relevant variables.

The maximum energy occurs when $\theta = 0$,(Fig. 3.10) i.e.:

$$y_{max} = \frac{2}{(1+1/x_\nu)^2-1} \quad (3.33)$$

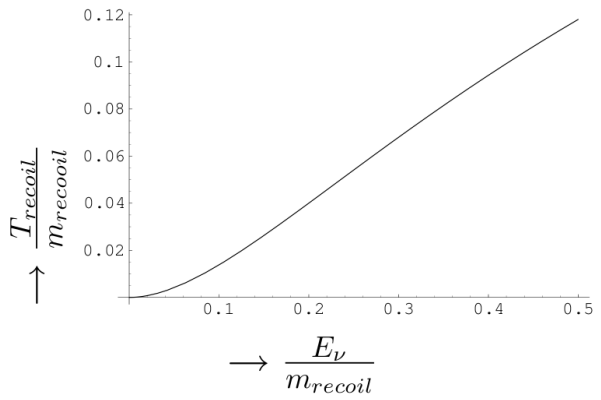

Figure 3.5: The maximum recoil energy as a function of the neutrino energy (both in units of the recoiling mass)

One can invert Eq. (3.32) and get the neutrino energy associated with a given recoil energy and scattering angle. One finds

$$x_\nu = \left(-1+\cos\theta\sqrt{1+\frac{2}{y}}\right)^{-1} \quad , \quad 0 \leq \theta \leq \pi/2 \tag{3.34}$$

The minimum neutrino (Fig. 3.6) energy for a given recoil energy is given by:

$$x_\nu^{min} = \left(-1+\sqrt{1+\frac{2}{y}}\right)^{-1} = \frac{y}{2}(1+\sqrt{1+\frac{2}{y}}) \tag{3.35}$$

The last equation is useful in obtaining the differential cross section (with respect to the recoil energy) after folding with the neutrino spectrum [11].

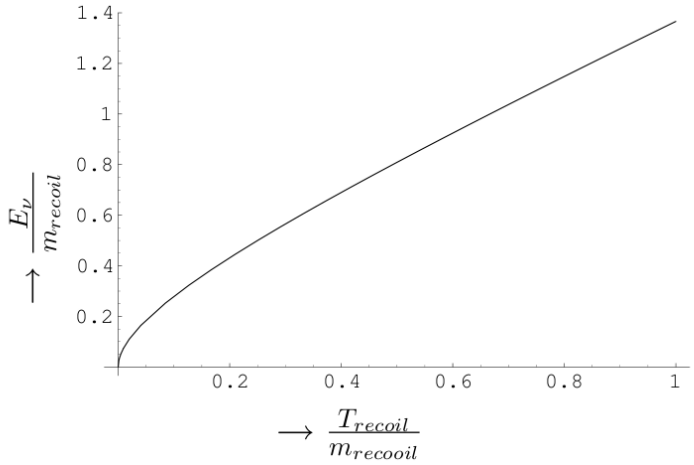

Figure 3.6: The minimum neutrino energy as a function of the recoil energy (both in units of the recoiling mass)

3.2.2 Coherent neutrino nucleus scattering

Coherent nuclear elastic scattering is a neutral current weak interaction. From a theoretical point of view, it is the same process of neutrino-nucleon neutral current scattering. If the momentum of the incoming neutrino is small enough, the single nucleon components (protons and neutrons) will not be distinguished and the neutrino is scattered from the nucleus, such that the amplitudes of the wave function of the nucleon to be in phase and to be added coherently. This turns out to be enhanced a factor of the order of the square of the neutron number compared to that of a single nucleon. The coherent behaviour of the interaction will depend on the actual momentum transfer between the incoming particles (neutrino and nucleus). The higher the momentum transfer, the higher the capacity of the neutrino to distinguish the single components of the nucleus, and hence the smaller the cross section.The nuclear form factor is the parameter that accounts for this dependence of the cross section on the momentum transfer. For this reactions is very usefull to calculate the differential cross section in terms of the recoil energy of the nucleus, instead of the angle of scattering, because most of the neutrino detectors are not sensitive to the direction of the neutrino. It is important to note that the coherent neutrino nucleus scattering hasn't bee experimentally studied yet [14, 21].

The coherent scattering of the neutrino with a nucleus (A,Z),

$$\nu + (A,Z) \rightarrow \nu + (A,Z)' \tag{3.36}$$

is a neutral current reaction,sensitive to all flavors of the neutrino, and is happening at procedures with a small energy transfer. At this reactions the wave function remains unchanged ($gs \rightarrow gs$ transition). Only the nucleus gains kinetic energy.

From the expressions (3.28), (3.28) we see that the vector current contribution, which may lead to coherence, is negligible in the case of the protons. Thus the coherent contribution may come from the neutrons and is expected to be proportional to the square of the neutron number. The neutrino-nucleus scattering can be derived in analogous fashion. It can also be obtained from the amplitude of the neutrino nucleon scattering by employing the appropriate kinematics, i.e. those involving the elastically scattered nucleus and the substitution

$$\boldsymbol{q} \Rightarrow \frac{\boldsymbol{p}}{A} \quad , \quad E_N \Rightarrow \sqrt{m_N^2 + \frac{\boldsymbol{p}^2}{A^2}} = \frac{E_A}{A} \tag{3.37}$$

with $\boldsymbol{q}$ the nucleon momentum, A is the nuclear mass number and $\boldsymbol{p}$ the nuclear momentum. Under the above assumptions the neutrino-nucleus cross section

takes the form:

$$\left(\frac{d\sigma}{dT_A}\right) = \frac{G_F^2 A m_N}{2\pi}[(M_V + M_A)^2 + (M_V - M_A)^2[1 - \frac{T_A}{E_\nu}]^2 + (M_A^2 - M_V^2)\frac{Am_N T_A}{E_\nu^2}] \quad (3.38)$$

where M_V and M_A are the nuclear matrix elements associated with the vector and the axial currents respectively and T_A is the energy of the recoiling nucleus. The axial current contribution vanishes for $0^+ \Rightarrow 0^+$ transitions. Anyway, it is negligible in the case of coherent scattering on neutrons. Thus Eq. (3.38) is reduced to:

$$\left(\frac{d\sigma}{dT_A}\right) = \frac{G_F^2 A m_N}{2\pi}(\frac{N^2}{4})F_{coh}(T_A, E_\nu) \quad (3.39)$$

with

$$F_{coh}(T_A, E_\nu) = F^2(Q^2)\left(1 + (1 - \frac{T_A}{E_\nu})^2 - \frac{Am_N T_A}{E_\nu^2}\right) \quad (3.40)$$

where N is the neutron number [17], Q^2 is the square of the four-momentum transferred

$$Q^2 = \frac{2E_\nu^2 T_A M_A}{E_\nu^2 - E_\nu T_A} \quad (3.41)$$

and $F(Q^2)$ is the nuclear form factor [18]. The effect of the nuclear form factor depends on the target, since the maximum recoil energy depends on the target (Fig. 3.7).

Nuclear Form Factor

In the expression for the cross section for a projectile scattering with a nucleus, the form factor gives a measure of the charge distribution in the nucleus. Specifically, the form factor is the Fourier transform of the density distribution of neutrons and protons.The proton density distribution is often well constrained by measured charge densities, and models exist to calculate the overall form factor. The form factor used in this paper is

$$F(Q^2) = \frac{3j_1(QR_0)}{QR_0}e^{-\frac{1}{2}(Qs)^2} \quad (3.42)$$

where $R_0^2 = R^2 - 5s^2$, $R = (1.2 \times A^{1/3})\ fm$ is the radius of the nucleus, and $s = 0.5\ fm$ is the surface thickness of the nucleus. The momentum transfer Q^2 has been given above [14, 18].

3.2.3 Quenching factors and energy thresholds

The above results refer to an ideal detector operating down to zero energy threshold. For a real detector, however, as we have already mentioned, the nuclear

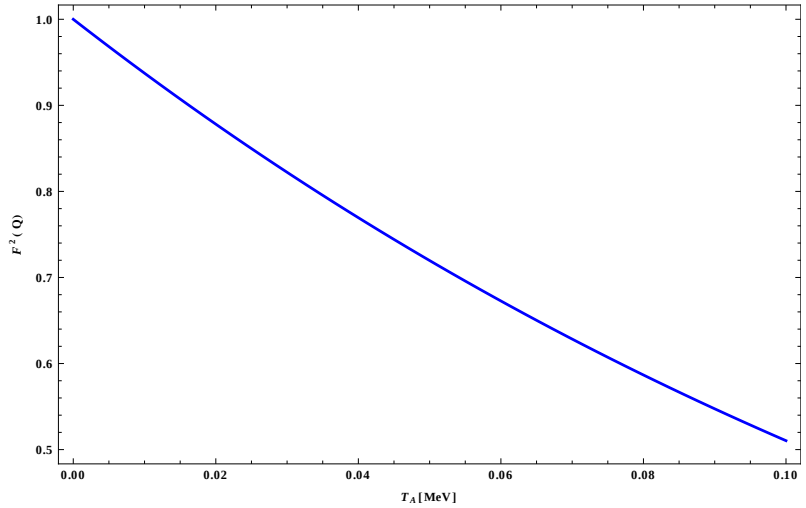

(a)

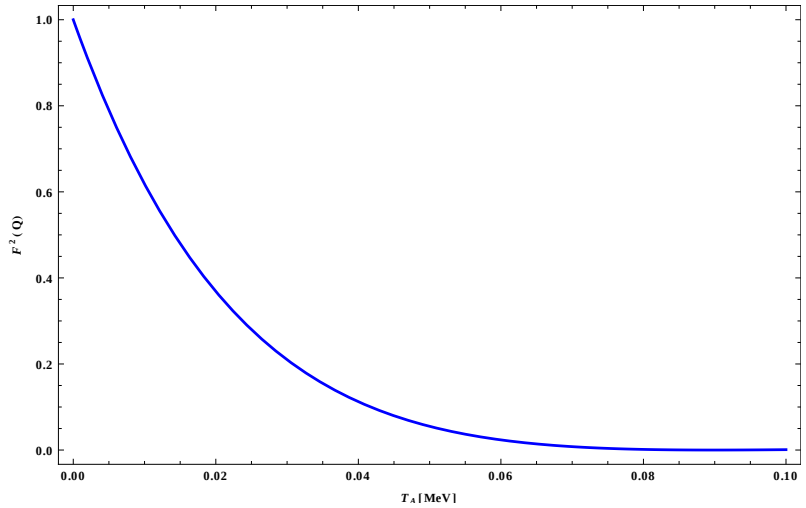

(b)

Figure 3.7: The square of the nuclear form factor, $F^2(T_A)$, as a function of the recoil energy for A=40(a) and A=131 (b). Note that the maximum recoil energy is different for each target.

recoil events are quenched, especially at low energies. The quenching factor for a given detector is the ratio of the signal height for a recoil track divided by that of an electron signal with the same energy. We should not forget that the signal heights depend on the velocity and how the signals are extracted experimentally. The actual quenching factors must be determined experimentally for each target. In the case of NaI the quenching factor is 0.05, while for Ge and Si it is $0.2-0.3$. For our purposes it is adequate, to multiply the energy scale by an recoil energy dependent quenching factor, $Q_{fac}(T_A)$ adequately described by the Lidhard theory. More specifically in our estimate of $Q_u(T_A)$ we assumed a quenching factor of

the following empirical form :

$$Q_{fac}(T_A) = r_1 \left(\frac{T_A}{1\ keV} \right)^{r_2}, \quad r_1 \approx 0.256\ , \quad r_2 \approx 0.153 \tag{3.43}$$

The quenching factors very much depend on the detector type. The quenching factor,exhibited in

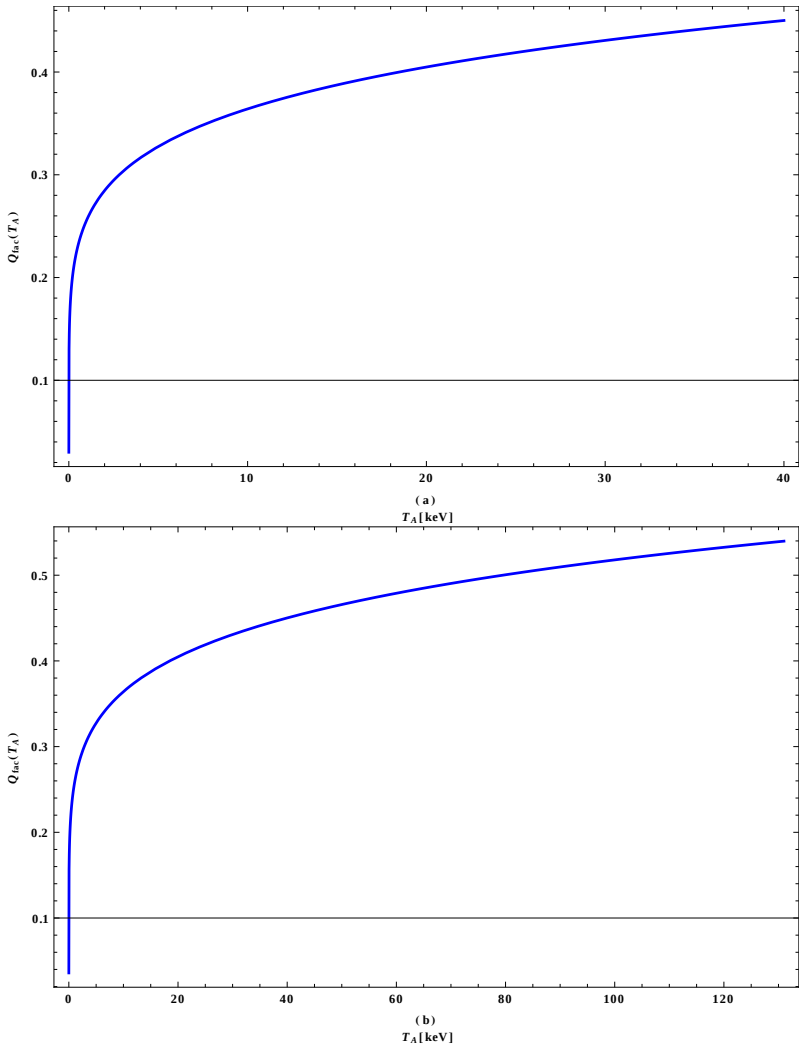

Figure 3.8: The quenching factor as a function of the recoil energy in the case of A=40 (a) and A=131 (b).

Fig. 3.8 for recoil energies of ^{131}Xe and ^{40}Ar, were obtained assuming the same quenching of the form of Eq. (3.43). In the presence of the quenching factor as given by Eq.(3.43) the measured recoil energy is typically reduced by factors of about 3, when compared with the electron energy. In other words a threshold energy of electrons of 1 keV becomes 3 keV for nuclear recoils [24].

3.3 Supernova neutrinos

3.3.1 Origin of type II SN neutrinos

A core collapse supernova (or type II supernova) is an astronomical phenomenon marking the end of a massive star's life. Models have shown that for stars with masses grater than $\sim$9 solar masses the end of the hydrogen burning phase is followed by a series of predictable cycles of contraction, heating and burning of progressively heavier elements within the star core (which assumes a onion like structure with the heavier element, iron, at the centre). The dynamical stability is granted, in each layer, by the energy produced in the nuclear fusions. However, in the iron core no net energy is produced as no fusion can occur; electron degeneracy pressure is the only force that prevents the core from collapsing. When the Chandrasekhar limit ($1.4\,M_{\odot}$) is exceeded, gravity becomes stronger than electron degeneracy and the iron core collapses. During the collapse, the temperature and density increase dramatically and two phenomena occur:

Photodisintegration

$$(A,Z)+\gamma \rightarrow (A',Z')+(Z-Z')p+(A-A'-Z+Z')n \tag{3.44}$$

Inverse Beta Decay

$$\begin{aligned} e^{-}+p &\rightarrow n+\nu_e \\ e^{+}+n &\rightarrow p+\bar{\nu}_e \end{aligned} \tag{3.45}$$

The iron core continues to shrink until the density approaches the nuclear density, and strong forces and neutron degeneracy prevent further collapse. The in-falling matter rebounds, creating an outgoing shockwave that dissociates nuclear matter, loosing energy and finally stalling. The interaction between the shockwave and the core generates extreme temperature/density conditions where nucleon bremsstrahlung and pair annihilation take place.

Bremsstralung

$$(A,Z)+(A',Z') \rightarrow (A,Z)+(A',Z')+\nu_{e,\mu,\tau}+\bar{\nu}_{e,\mu,\tau} \tag{3.46}$$

Pair Annihilation

$$e^- + e^+ \rightarrow \nu_{e,\mu,\tau} + \bar{\nu}_{e,\mu,\tau} \tag{3.47}$$

This last two (3.46),(3.47) are Z_0 mediated neutral current processes.
Numerical simulations show that the interaction of a small fraction (0.1%) of the neutrinos generated in this phase with the nuclear matter behind the stalled shock should be enough to rise the shock total energy to positive values. Unbounded layers are ejected in the supernova explosion.

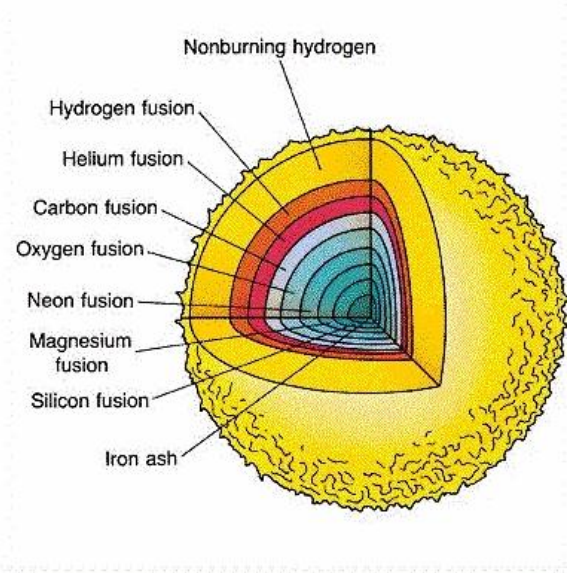

Figure 3.9: At the stage of the main sequence a massive star, the burning of Si starts when the temperature reaches $3-4\times10^9$ K and creates a central core of Fe, which is surrounded form concentric shells of (from inside to outside) Si, O, Ne, C, He, and H. Thus, the central core of Fe is surrounded from shells of brighter elements and the star has an onion-skin like structure.

The processes in Equations (3.45),(3.46)and(3.47) are the mechanisms that generate the neutrino fluxes emitted in the supernova explosion. The individual contributions to the total flux are ∼10-20% from inverse beta decay and ∼80-90% from pair annihilation and bremsstrahlung. A simplified model for the neutrino emission is used in literature when the process described in Equations (3.46) and (3.47) can be considered as the main channels of neutrino production. This approximation is especially valid in the case of detection through coherent scattering. As will be explained in section II B, coherent scattering is blind to neutrino flavour; processes like the ones in Equation (3.47) can thus be considered the main source of the interacting neutrinos. The same simplified model predicts the

equipartition of the total energy ($\sim 3\times10^{53} ergs$) among the six neutrino and antineutrino flavours at production. The emission spectra will have different shapes due to the different interaction cross sections, free paths and neutrino sphere's radii for the different species, with resulting different temperatures for $\nu_e, \bar{\nu}_e$ and ν_x , where ν_x are all the remaining neutrino and antineutrino ($\nu_\mu, \bar{\nu}_\mu, \nu_\tau, \bar{\nu}_\tau$) families [14, 24] (Fig. 3.10).

3.3.2 SN neutrino spectra

In modern literature, the energy spectrum of the SN-neutrinos is parametrized with different forms, with most prevalent the 'pinched' Fermi-Dirac distribution. Thus the flux of SN-neutrinos is described by the analytical expression

$$\frac{dN}{dE_\nu} \equiv f_\nu(E_\nu, T_\nu, n_\nu) = N_\nu \frac{1}{F(n_\nu)} \frac{E_\nu^2}{e^{E_\nu/T_{nu}-n_\nu}+1} \tag{3.48}$$

where $N_\nu = U_\nu/T_\nu$ is each flavors number of neutrinos, which as we see is calculated from U_ν the total energy of each flavor and the temperature of each neutrino species [22]. In our case the temperature is taken to be 3.5,5 and 8 MeV for electron neutrinos (ν_e), electron antineutrinos $(\bar{\nu}_e)$, and all other flavors (ν_x) respectively. The parameter n_ν is an dimensionless free parameter which determines the width of the distribution. By inserting this parameter the width of the spectrum is decreased in comparison with the the thermal spectrum (that's why it's called pinching parameter). The parameter $F(n_\nu)$, is the normalization constant which is defined so that

$$\int_0^\infty f_\nu(E_\nu, T_\nu, n_\nu) dE_\nu = 1 \tag{3.49}$$

i.e. the normalization constant depends on the pinching parameter n_ν.
The normalization constant is equal to

$$\frac{1}{F(n_\nu)} \equiv \int_0^\infty \frac{x^2}{e^{x-n_\nu}+1} dx \tag{3.50}$$

The relationship (3.51) is verified from many simulations in terms of the quality characteristics of the SN-neutrinos,

$$n_{\nu_e} = 0-3, \qquad n_{\bar{\nu}_e} = 0-3, \qquad n_{\nu_x} = 0-2. \tag{3.51}$$

We must note that the mean neutrino energy depends not only by the temperature, but also by the pinching parameter n_ν.

The mean neutrino energy obtained from the Fermi-Dirac distribution, is defined as

$$\langle E_\nu \rangle = \int_0^\infty E_\nu \cdot f_{sp}(E_\nu)\, dE_\nu \tag{3.52}$$

n_ν	$\langle E_\nu \rangle$ $[MeV]$		
	ν_e $T = 3.5\ MeV$	$\bar{\nu}_e$ $T = 5\ MeV$	$\sum_x \nu_x$ $T = 8\ MeV$
0	11.0298	15.7569	25.2110
1	11.6356	16.6223	26.5957
2	12.0787	18.0277	28.8443
3	13.9733	19.9619	31.9391
4	15.6313	22.3305	35.7288

Table 3.1: The average SN-neutrino energies as a function of parameters n_ν and T_ν

n_ν	$N_\nu\ /10^{58}$		
	ν_e $T = 3.5\ MeV$	$\bar{\nu}_e$ $T = 5\ MeV$	$\sum_x \nu_x$ $T = 8\ MeV$
0	0.282969	0.198079	0.495196
1	0.268207	0.187745	0.469363
2	0.247326	0.173128	0.432820
3	0.223361	0.156353	0.390882
4	0.199669	0.139768	0.349421

Table 3.2: The number of primary neutrinos emitted in a typical supernova explosion as a function of the parameters n_ν and T_ν in units of 10^{58}.

thus if we take into account the $U_\nu = 0.5 \times 10^{53}\ ergs$ of emitted energy for every neutrino flavor we can calculate the number of emitted neutrinos. The obtained results are shown below, as well as the flux $\Phi_\nu = N_\nu/(4\pi D^2)$ at distance $D = 10\ kpc = 3.1 \times 10^{22}\ cm$ [14]. The distance of $10\ kpc$ is chosen because it is calculated to be the distance with the highest probability for a supernova explosion. Another distance that is popular in literature is the $8.5\ kpc$, as it is the distance of the centre of our galaxy. Though it is obvious, it is still very important to stress the strong dependence of the flux (and consequently the expected number of interacting neutrinos) on the distance at which the supernova occurs. Calculations show that the probability distribution for the distance between the Earth and a supernova does not exclude smaller distances at all.

n_ν	$\Phi_\nu \ /10^{12}\ cm^{-2}$		
	ν_e $T = 3.5\ MeV$	$\bar{\nu}_e$ $T = 5\ MeV$	$\sum_x \nu_x$ $T = 8\ MeV$
0	0.234318	0.164023	0.410057
1	0.222094	0.155466	0.388665
2	0.204803	0.143362	0.358405
3	0.184958	0.129471	0.323677
4	0.165340	0.115738	0.289345

Table 3.3: The (time integrated) neutrino flux, in units of $10^{12}\ cm^{-2}$, at a distance $10\ kpc$ from the source.

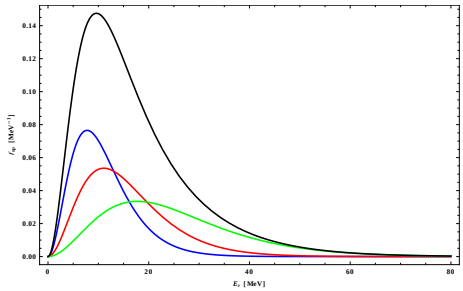

(a) Pinching factor $n_\nu = 0$

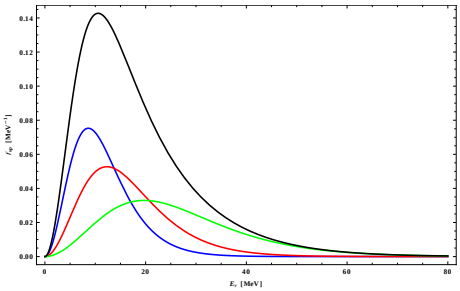

(b) Pinching factor $n_\nu = 1$

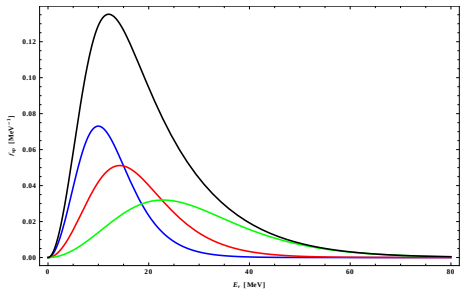

(c) Pinching factor $n_\nu = 2$

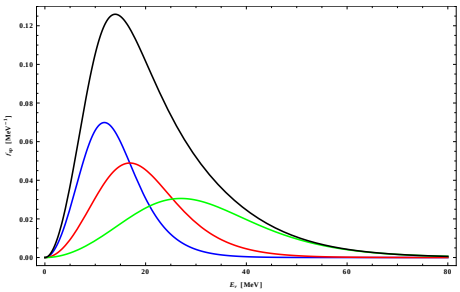

(d) Pinching factor $n_\nu = 3$

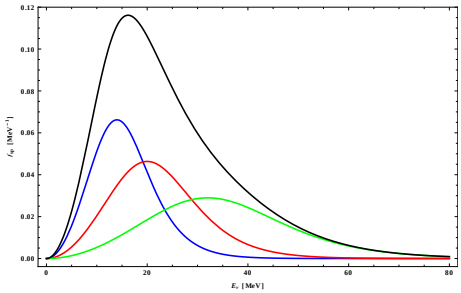

(e) Pinching factor $n_\nu = 4$

Figure 3.10: The normalized to unity SN-neutrino spectrum for $n_\nu = 0$ (top) and $n_\nu = 3$ (bottom).The continuous,dotted and dashed blue curves correspond to $T = 3.5(\nu_e)$, $5(\bar{\nu}_e)$ and $8(\nu_x)$ MeV respectively. The black curve corresponds to the total emitted neutrino spectrum.

3.3.3 Events number calculation

In this work one question that has to be answered, is how many events the SPC would have counted, if there was a SN explosion. This question is quite difficult to answer because there are many parameters that one should keep in mind. Such parameters are the radius, the choice of gas and the threshold of SPC. The free parameters involving the SN itself are the different spectra of the SN, as well as the distance that the explosion occurred.

The first step is to calculate the total cross section of the neutrino-nucleus interaction for the gas filling we use at the SPC. The gas filling that are studied are the ^{131}Xe and the ^{40}Ar. Since the SN is not 'monochromatic' the equation (3.39) has to be written as

$$\frac{d\sigma}{dT_A}(T_A) = \int_{E(T_{thrs})}^{(E_\nu)_{max}} \left(\frac{d\sigma}{dT_A}(E_\nu, T_A) \right) \cdot f_{sp}(E_\nu, T_A, n_\nu) dE_\nu \tag{3.53}$$

Where $(E_\nu)_{max}$ is the maximum neutrino energy and

$$E(T_A) = \frac{T_A}{2} + \sqrt{\frac{T_A}{2}(M_A + \frac{T_A}{2})} \tag{3.54}$$

Here $(E_\nu)_{max} = \infty$.
Integrating the differential cross section (3.53) from T_{thrs} to infinity (for every neutrino flavor that is emitted from a during a SN explosion) we obtain the total cross section. The threshold recoil energy depends on the capabilities of the detector. Furthermore for a real detector the nuclear recoil events, due the nature of the interaction, are quenched, especially at low energies.

The number of the observed events for each neutrino species is found to be

$$N_{ev}(n_\nu, T_\nu) = \Phi_\nu \sigma(n_\nu, T_\nu, T_{thrs}) N_d(P, T_0, R) \tag{3.55}$$

$$N_d(P, T_0, R) = \frac{P}{kT_0} \frac{4}{3} \pi R^3 \tag{3.56}$$

where N_d is the number density of target nuclei in the detector, which depends on the pressure (P), the absolute temperature (T_0) and the radius (R) of the detector.

To obtain the total cross section for a target of nucleus, first we have to obtain a differential cross of the form of equation (3.53), which depends only from the recoil energy. To do so we have to fold the differential cross section (3.39) with the energy spectrum, for energies from $0 - (E_\nu)max$ for each neutrino flavor. Because the energy of the incoming neutrino E_ν is orders of magnitude greater than the recoil energy T_A, we can simplify the relationship to of the four-momentum transfer to $Q^2 = 2M_A T_A$. This simplification will help us to integrate analytically the relationship

$$\frac{d\sigma}{dT_A}(T_A) = F^2(Q^2) \int_{E(T_{thrs})}^{(E_\nu)max} \left(1 + (1 - \frac{T_A}{E_\nu})^2 - \frac{A m_N T_A}{E_\nu^2} \right) \cdot f_{sp}(E_\nu, T_A, n_\nu) dE_\nu \tag{3.57}$$

Also the form factor must be normalized to unity when the moment transfer is equal to zero ($F^2(0) = 1$), so we must modify the relationship (3.42) to

$$F(Q^2) = \frac{3j_1(QR_0 + \delta_{0,Q^2})}{QR_0 + \delta_{0,Q^2}} Exp\left(\frac{1}{2}(QR_0)^2\right) \tag{3.58}$$

The result is the product of the form factor squared and a polynomial of second degree in recoil energy.

$$\sigma_{tot} = \int_{(T_A)_{thrs}}^{(T_A)_{max}} F^2(Q) \cdot \sum_{i=0}^{2} C_i T_A^2 dT_A \tag{3.59}$$

By finding the roots of this polynomial we obtain the maximum recoil energy ($(T_A)_{max}$) for each neutrino flavor.

Now we can integrate the differential cross section (3.59) from the threshold recoil energy to the maximum recoil energy (depends on the distribution of the neutrino spectrum) to obtain the total cross section. The threshold recoil energy as we said depends on the detector, if we assume a perfect detector we have $(T_A)_{min} = 0$. Because a perfect detector does not exist, we must obtain the event rate in the presence of a threshold. We assume a detection threshold of 1 keV (larger than the current threshold of our detector which is ~ 100 eV. Because of the quenching factor, this threshold is increased to 3 keV, so we must take that into account when we calculate the event rate.
The results for values of the pinching factor $n_\nu = 0-4$, $(T_A)_{thrs} = 0,1,3$ keV, for gas fillings Ar and Xe (in 10 atm pressure) and for SPC radii $R = 0.65,4,10$ m, are presented in the following sections.

3.3.4 Results for the Ar target

Neutrino-Ar Differential cross $d\sigma/dT_A$ as a function of the neutrino energy E_ν and the recoil nucleus energy T_A, for values of the pinching factor $n_\nu = 0-4$ and for every neutrino flavor emitted by a SN.

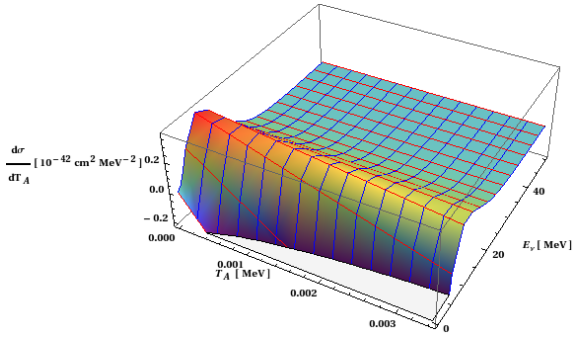

(a) Pinching factor $n_\nu = 0$

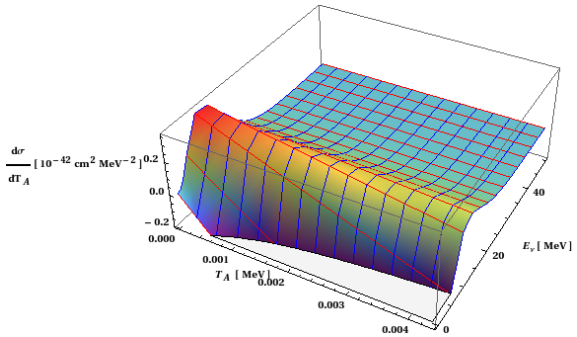

(b) Pinching factor $n_\nu = 1$

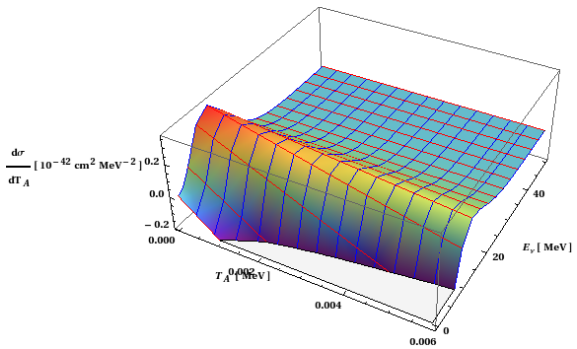

(c) Pinching factor $n_\nu = 2$

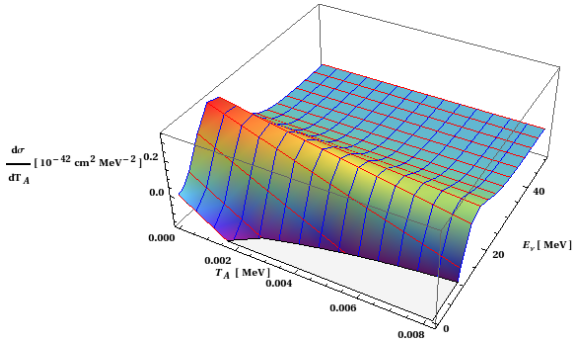

(d) Pinching factor $n_\nu = 3$

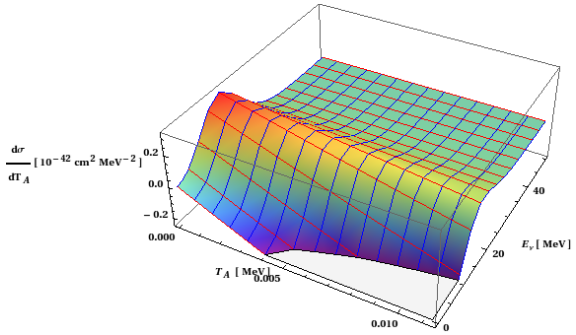

(e) Pinching factor $n_\nu = 4$

Figure 3.11: Differential cross $d\sigma/dT_A(E_\nu, T_A) \cdot f_{sp}(E_\nu, T_A, n_\nu)$ for the ν_e flavor.

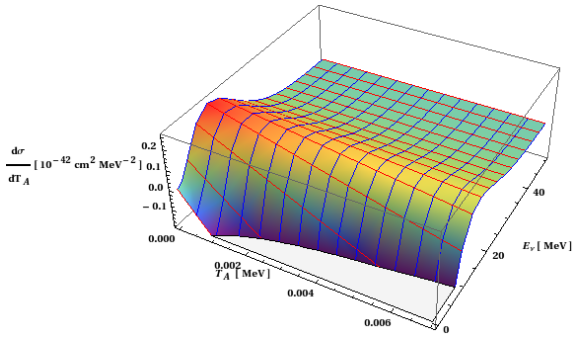

(a) Pinching factor $n_\nu = 0$

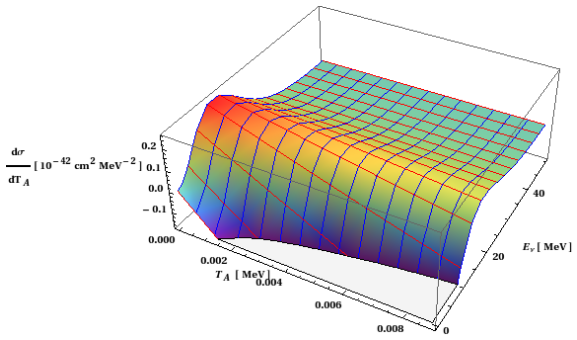

(b) Pinching factor $n_\nu = 1$

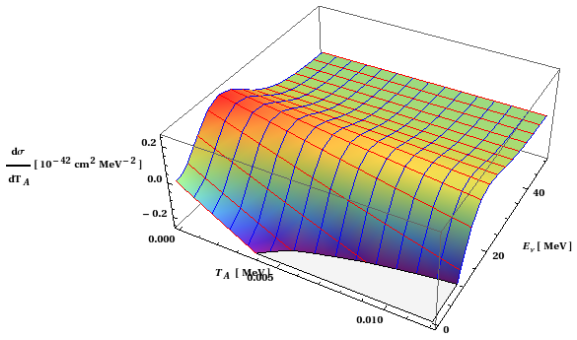

(c) Pinching factor $n_\nu = 2$

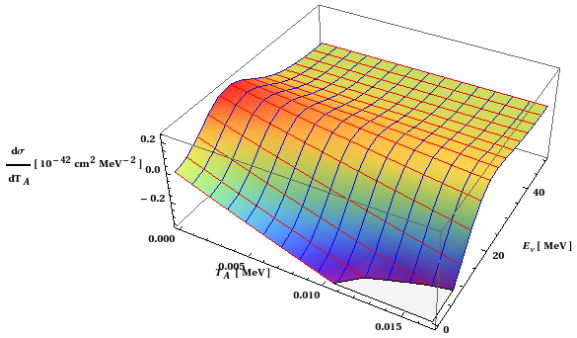

(d) Pinching factor $n_\nu = 3$

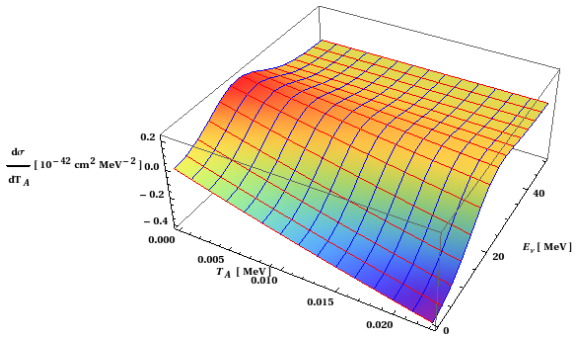

(e) Pinching factor $n_\nu = 4$

Figure 3.12: Differential cross $d\sigma/dT_A(E_\nu, T_A) \cdot f_{sp}(E_\nu, T_A, n_\nu)$ for the $\bar{\nu}_e$ flavor.

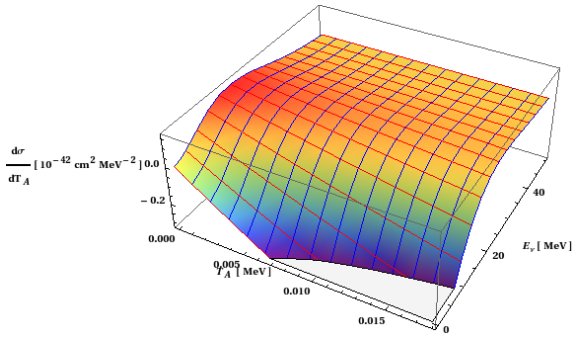

(a) Pinching factor $n_\nu = 0$

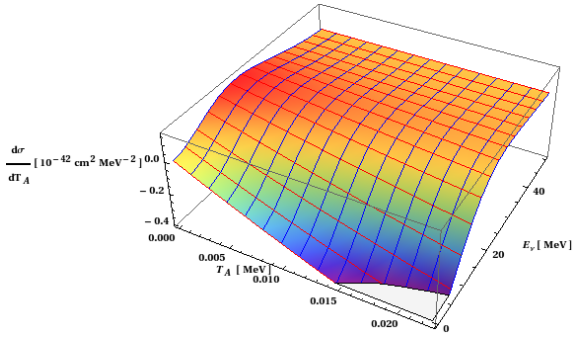

(b) Pinching factor $n_\nu = 1$

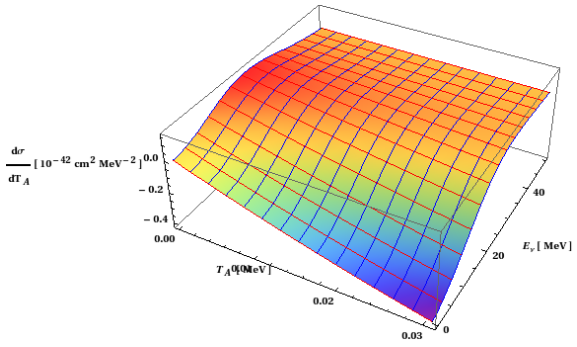

(c) Pinching factor $n_\nu = 2$

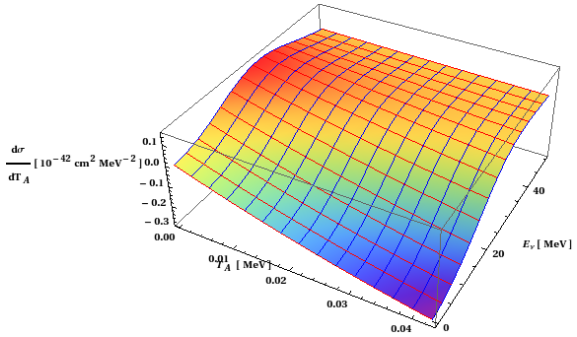

(d) Pinching factor $n_\nu = 3$

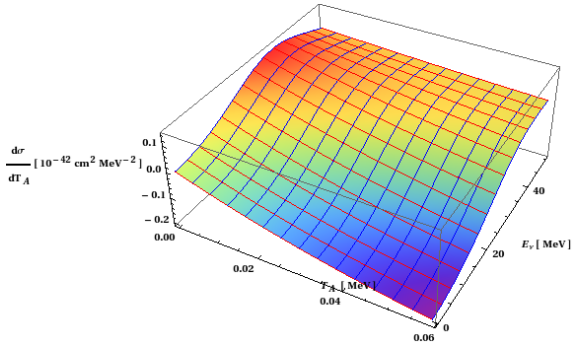

(e) Pinching factor $n_\nu = 4$

Figure 3.13: Differential cross $d\sigma/dT_A(E_\nu, T_A) \cdot f_{sp}(E_\nu, T_A, n_\nu)$ for the ν_x flavors.

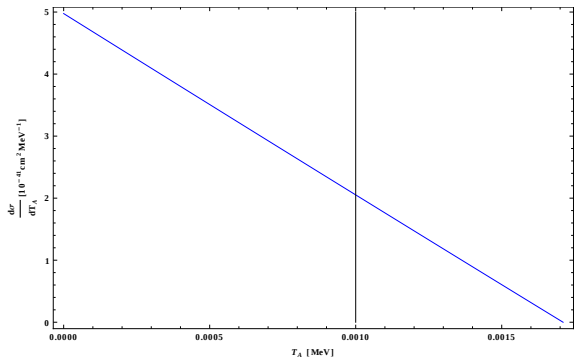

(a) Pinching factor $n_\nu = 0$

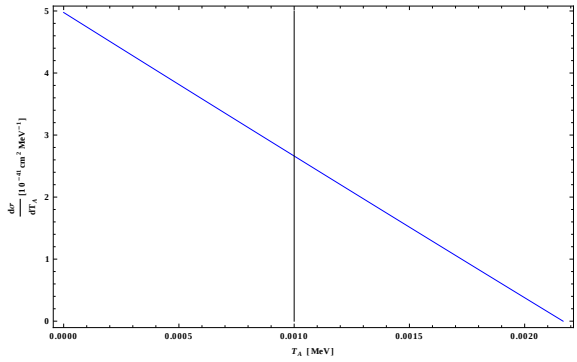

(b) Pinching factor $n_\nu = 1$

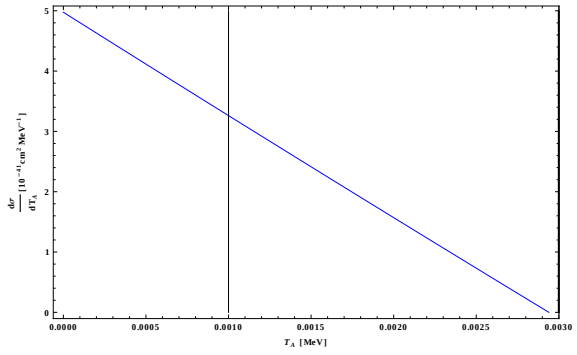

(c) Pinching factor $n_\nu = 2$

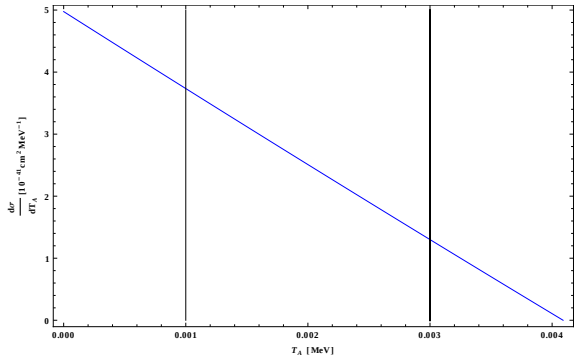

(d) Pinching factor $n_\nu = 3$

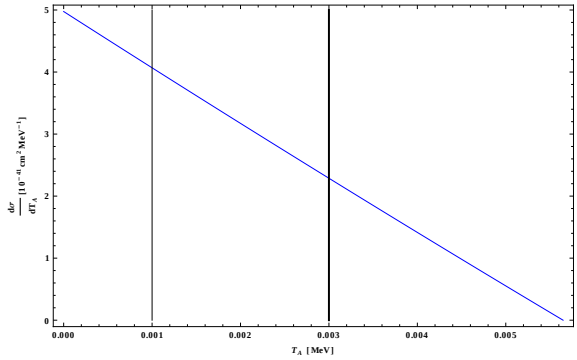

(e) Pinching factor $n_\nu = 4$

Figure 3.14: Differential cross $d\sigma/dT_A(T_A)$ for the ν_e flavor.The thin and thick vertical bars represent the $(T_A)_{thrs}$ and the threshold energy from the quenching factor.

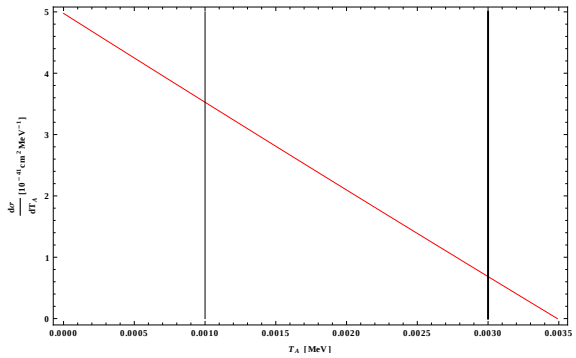

(a) Pinching factor $n_\nu = 0$

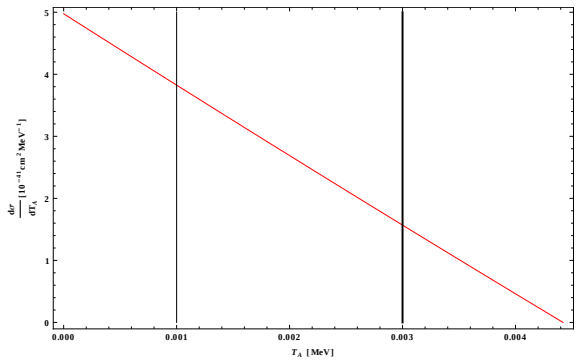

(b) Pinching factor $n_\nu = 1$

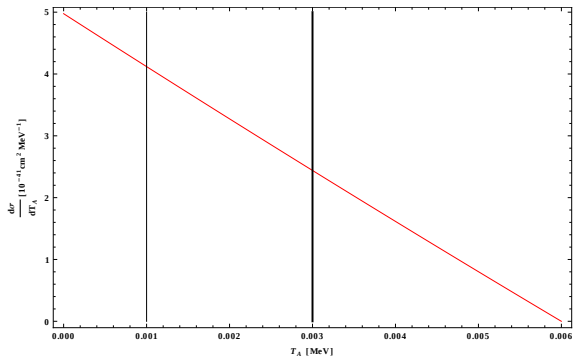

(c) Pinching factor $n_\nu = 2$

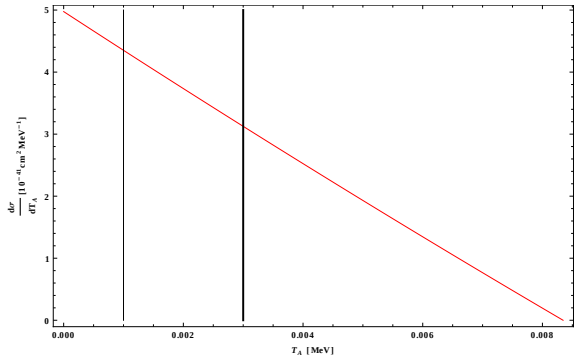

(d) Pinching factor $n_\nu = 3$

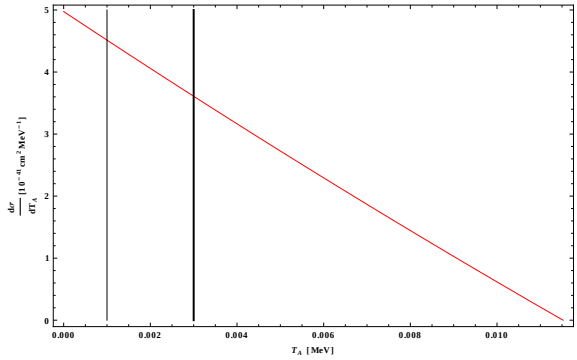

(e) Pinching factor $n_\nu = 4$

Figure 3.15: Differential cross $d\sigma/dT_A(T_A)$ for the $\bar{\nu}_e$ flavor.The thin and thick vertical bars represent the $(T_A)_{thrs}$ and the threshold energy from the quenching factor.

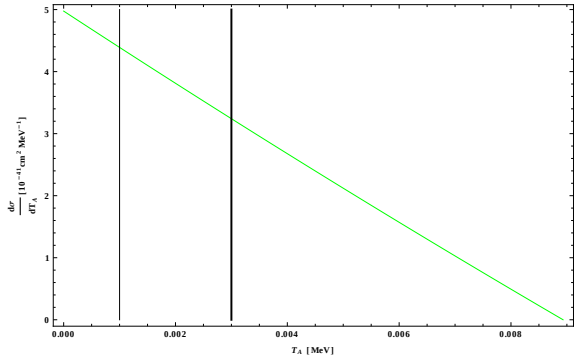

(a) Pinching factor $n_\nu = 0$

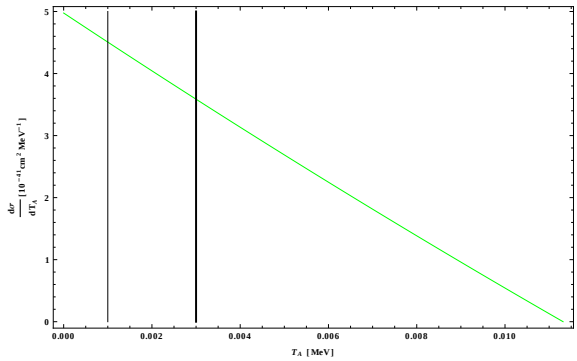

(b) Pinching factor $n_\nu = 1$

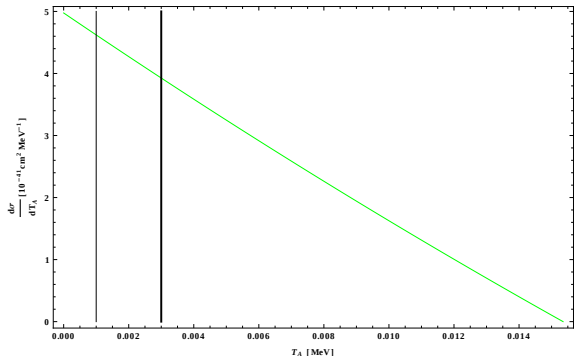

(c) Pinching factor $n_\nu = 2$

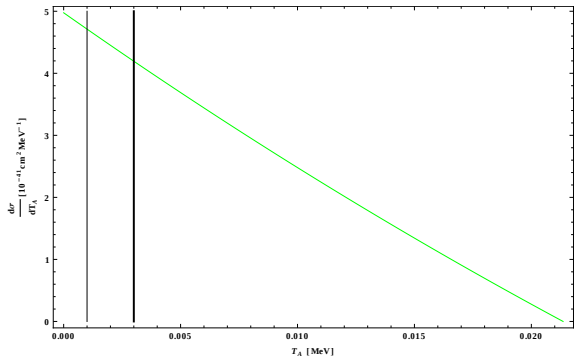

(d) Pinching factor $n_\nu = 3$

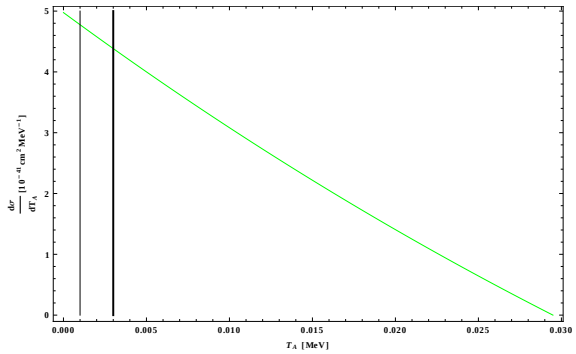

(e) Pinching factor $n_\nu = 4$

Figure 3.16: Differential cross $d\sigma/dT_A(T_A)$ for the ν_x flavor.The thin and thick vertical bars represent the $(T_A)_{thrs}$ and the threshold energy from the quenching factor.

(a) Total cross section for $(T_A)_{thrs} = 0\ keV$

n_ν	$\sigma_{tot}\ /10^{-40}\ cm^2$			
	ν_e $T = 3.5\ MeV$	$\bar{\nu}_e$ $T = 5\ MeV$	$\sum_x \nu_x$ $T = 8\ MeV$	Total
0	4.239	8.614	21.800	34.653
1	5.365	10.895	27.477	43.737
2	7.268	14.731	36.963	58.962
3	10.086	20.393	50.764	81.243
4	13.882	27.971	68.905	110.758

(b) Total cross section for $(T_A)_{thrs} = 1\ keV$

n_ν	$\sigma_{tot}\ /10^{-40}\ cm^2$			
	ν_e $T = 3.5\ MeV$	$\bar{\nu}_e$ $T = 5\ MeV$	$\sum_x \nu_x$ $T = 8\ MeV$	Total
0	0.728	4.367	17.117	22.212
1	1.549	6.496	22.737	30.782
2	3.151	10.187	32.265	45.603
3	5.7326	15.730	45.9214	67.384
4	9.360	23.227	64.029	96.616

(c) Total cross section for $(T_A)_{thrs} = 3\ keV$

n_ν	$\sigma_{tot}\ /10^{-40}\ cm^2$			
	ν_e $T = 3.5\ MeV$	$\bar{\nu}_e$ $T = 5\ MeV$	$\sum_x \nu_x$ $T = 8\ MeV$	Total
0	0	1.675	9.491	11.166
1	0	1.111	14.647	15.758
2	0.003	3.635	23.619	27.257
3	0.707	15.730	37.016	53.453
4	3.012	23.227	54.871	81.110

Table 3.4: Total cross sections of the $Neutrino - Ar$ elastic scattering for pinching factor values $n_\nu = 0 - 4$.

(a) Event rate for $n_\nu = 0$

$R\ [m]$	Number of events		
	$(T_A)_{thrs} = 0\ kev$	$(T_A)_{thrs} = 1\ kev$	$(T_A)_{thrs} = 3\ kev$
0.65	0	0	0
4	74	52	29
10	1162	810	549

(b) Event rate for $n_\nu = 1$

$R\ [m]$	Number of events		
	$(T_A)_{thrs} = 0\ kev$	$(T_A)_{thrs} = 1\ kev$	$(T_A)_{thrs} = 3\ kev$
0.65	0	0	0
4	89	67	40
10	1390	1044	619

(c) Event rate for $n_\nu = 2$

$R\ [m]$	Number of events		
	$(T_A)_{thrs} = 0\ kev$	$(T_A)_{thrs} = 1\ kev$	$(T_A)_{thrs} = 3\ kev$
0.65	0	0	0
4	110	89	58
10	1726	1396	921

(d) Event rate for $n_\nu = 3$

$R\ [m]$	Number of events		
	$(T_A)_{thrs} = 0\ kev$	$(T_A)_{thrs} = 1\ kev$	$(T_A)_{thrs} = 3\ kev$
0.65	1	1	1
4	137	117	86
10	2145	1840	1350

(e) Event rate for $n_\nu = 4$

$R\ [m]$	Number of events		
	$(T_A)_{thrs} = 0\ kev$	$(T_A)_{thrs} = 1\ kev$	$(T_A)_{thrs} = 3\ kev$
0.65	1	1	1
4	167	149	119
10	2609	2332	1857

Table 3.5: Number of events for the different radii of the SPC .

n_ν	$(T_A)_{max}$ keV		
	ν_e $T = 3.5$ MeV	$\bar{\nu}_e$ $T = 5$ MeV	$\sum_x \nu_x$ $T = 8$ MeV
0	1.710	3.490	8.932
1	2.167	4.421	11.316
2	2.940	5.199	15.353
3	4.900	8.345	21.367
4	5.648	11.524	29.491

Table 3.6: Maximum recoil energy $(T_A)_{max}$, for pinching factor values $n_\nu = 0-4$.

3.3.5 Results for the Xe target

Neutrino-Xe Differential cross $d\sigma/dT_A$ as a function of the neutrino energy E_ν and the recoil nucleus energy T_A, for values of the pinching factor $n_\nu = 0-4$ and for every neutrino flavor emitted by a SN.

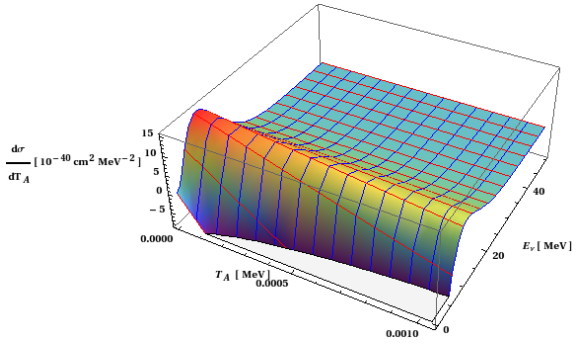

(a) Pinching factor $n_\nu = 0$

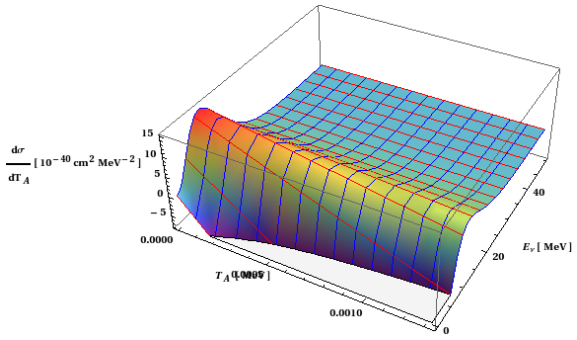

(b) Pinching factor $n_\nu = 1$

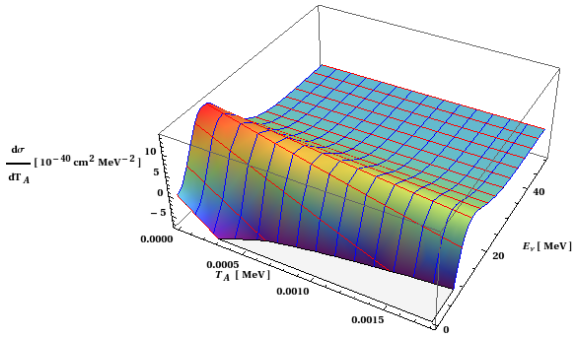

(c) Pinching factor $n_\nu = 2$

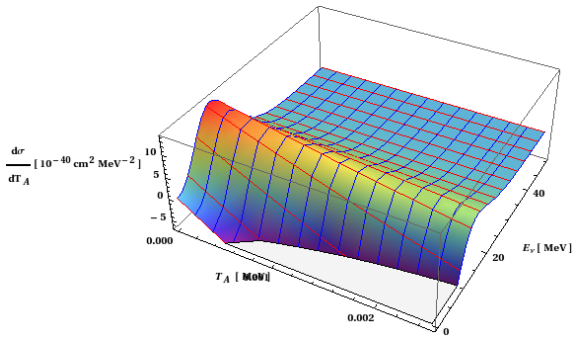

(d) Pinching factor $n_\nu = 3$

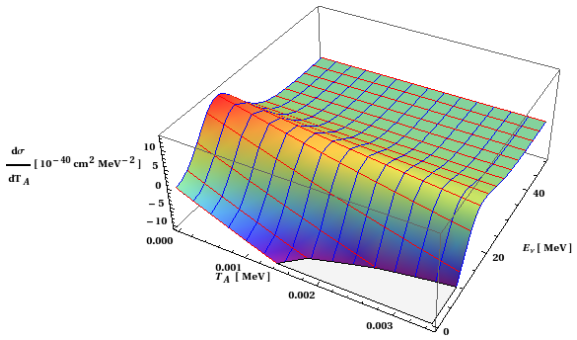

(e) Pinching factor $n_\nu = 4$

Figure 3.17: Differential cross $d\sigma/dT_A(E_\nu, T_A) \cdot f_{sp}(E_\nu, T_A, n_\nu)$ for the ν_e flavor.

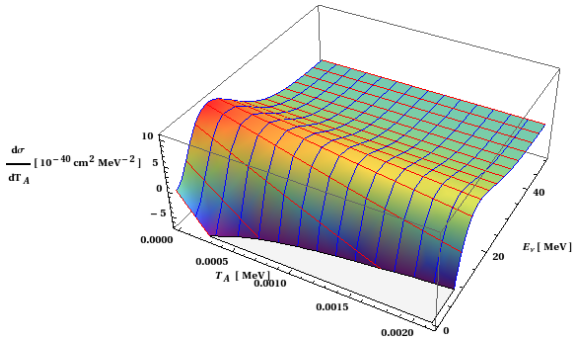

(a) Pinching factor $n_\nu = 0$

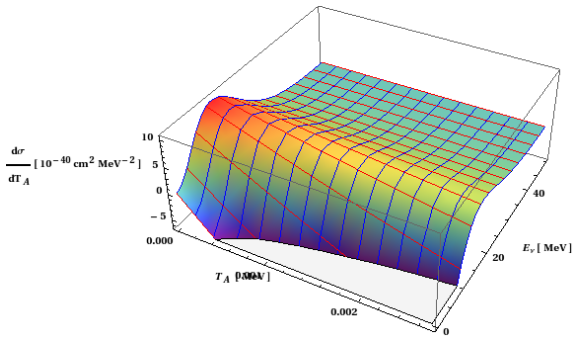

(b) Pinching factor $n_\nu = 1$

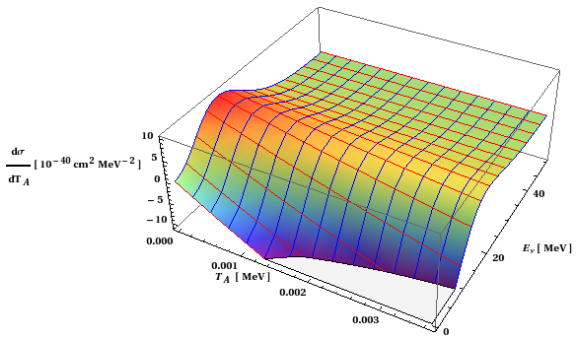

(c) Pinching factor $n_\nu = 2$

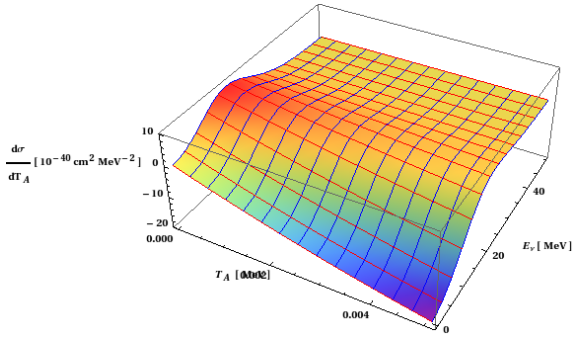

(d) Pinching factor $n_\nu = 3$

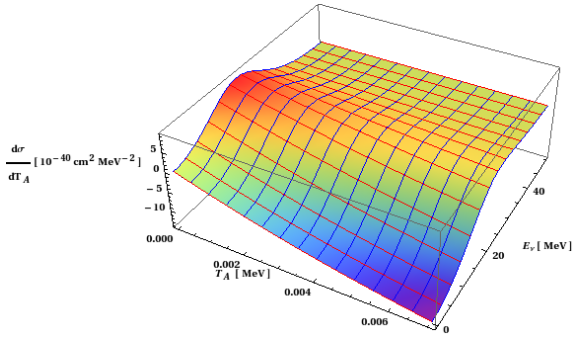

(e) Pinching factor $n_\nu = 4$

Figure 3.18: Differential cross $d\sigma/dT_A(E_\nu, T_A) \cdot f_{sp}(E_\nu, T_A, n_\nu)$ for the $\bar{\nu}_e$ flavor.

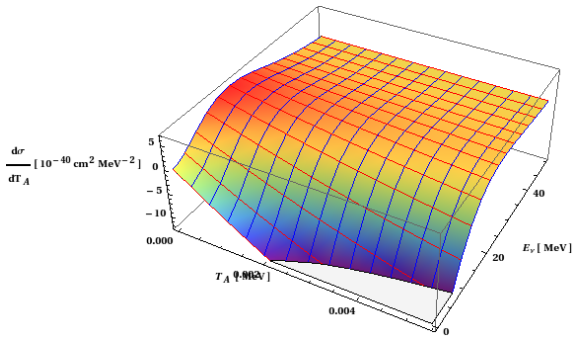

(a) Pinching factor $n_\nu = 0$

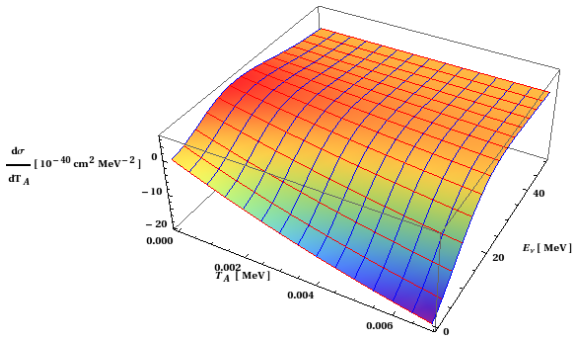

(b) Pinching factor $n_\nu = 1$

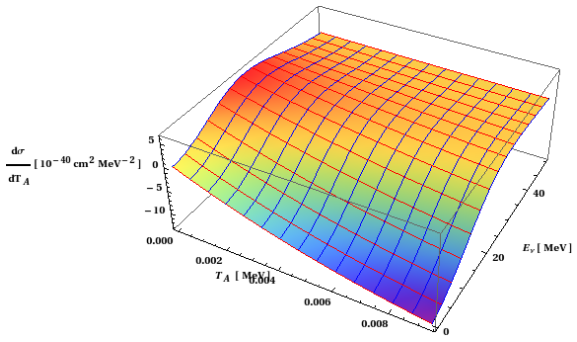

(c) Pinching factor $n_\nu = 2$

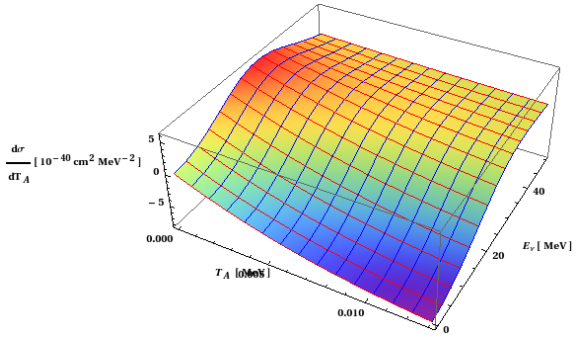

(d) Pinching factor $n_\nu = 3$

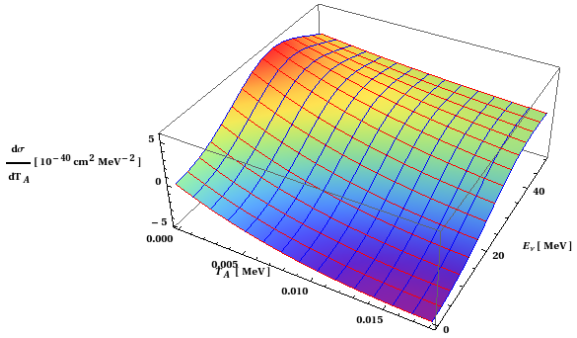

(e) Pinching factor $n_\nu = 4$

Figure 3.19: Differential cross $d\sigma/dT_A(E_\nu, T_A) \cdot f_{sp}(E_\nu, T_A, n_\nu)$ for the ν_x flavors.

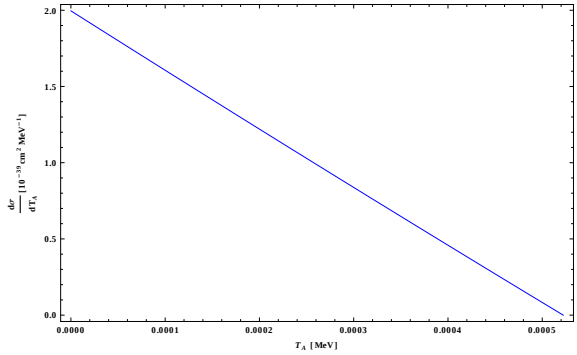

(a) Pinching factor $n_\nu = 0$

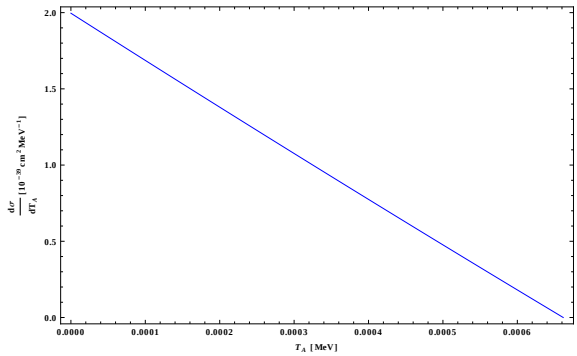

(b) Pinching factor $n_\nu = 1$

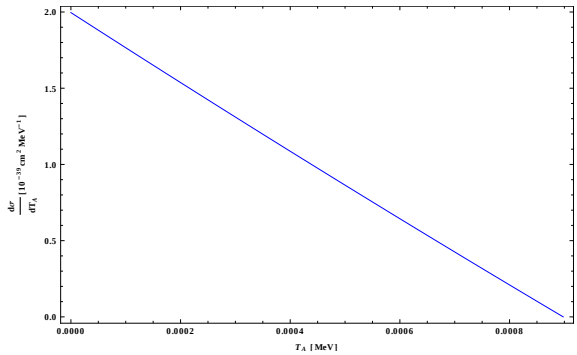

(c) Pinching factor $n_\nu = 2$

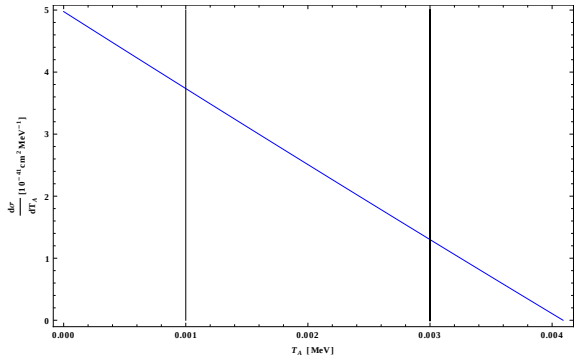

(d) Pinching factor $n_\nu = 3$

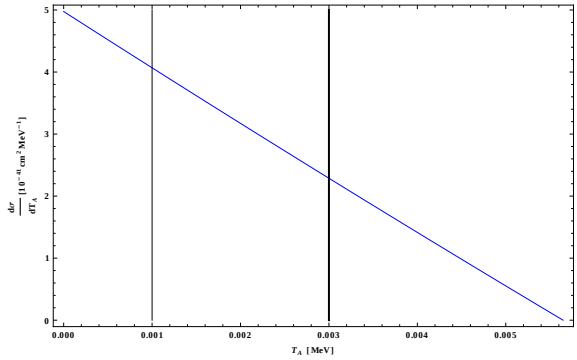

(e) Pinching factor $n_\nu = 4$

Figure 3.20: Differential cross $d\sigma/dT_A(T_A)$ for the ν_e flavor.The thin and thick vertical bars represent the $(T_A)_{thrs}$ and the threshold energy from the quenching factor.

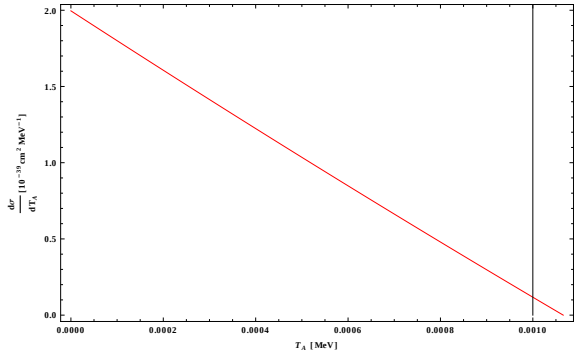

(a) Pinching factor $n_\nu = 0$

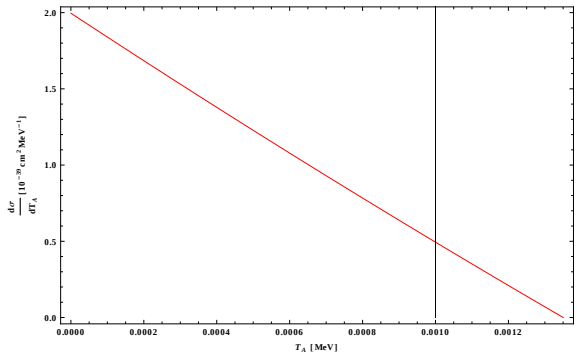

(b) Pinching factor $n_\nu = 1$

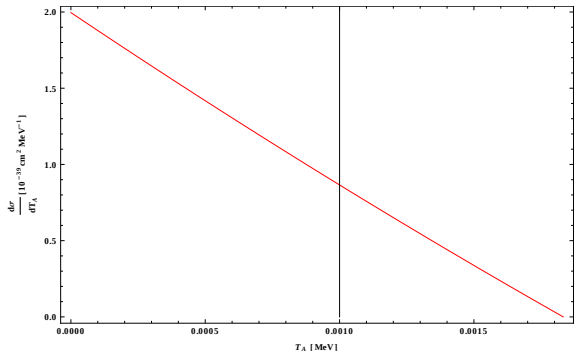

(c) Pinching factor $n_\nu = 2$

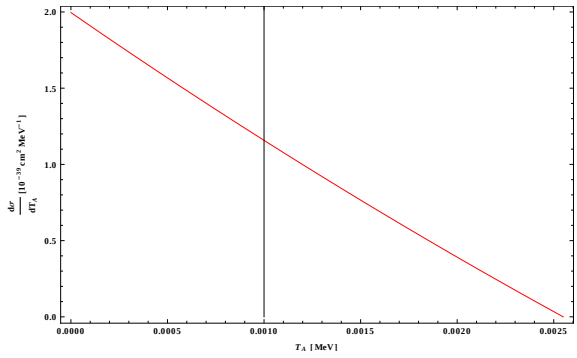

(d) Pinching factor $n_\nu = 3$

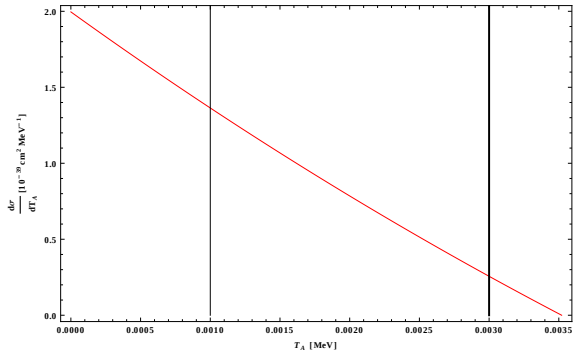

(e) Pinching factor $n_\nu = 4$

Figure 3.21: Differential cross $d\sigma/dT_A(T_A)$ for the $\bar{\nu}_e$ flavor.The thin and thick vertical bars represent the $(T_A)_{thrs}$ and the threshold energy from the quenching factor.

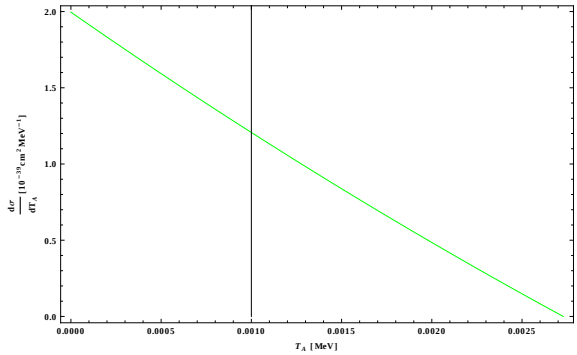

(a) Pinching factor $n_\nu = 0$

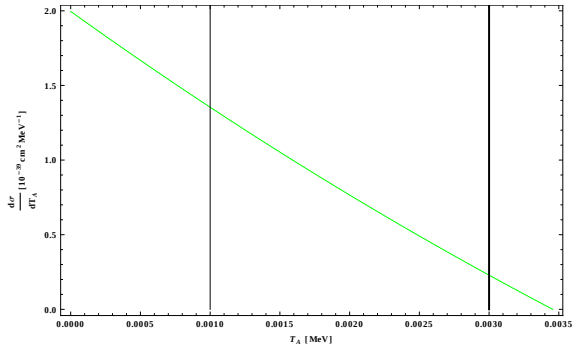

(b) Pinching factor $n_\nu = 1$

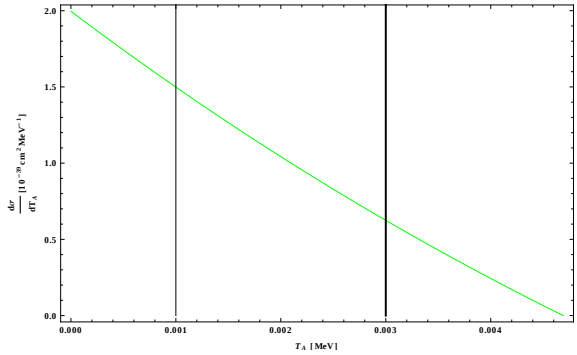

(c) Pinching factor $n_\nu = 2$

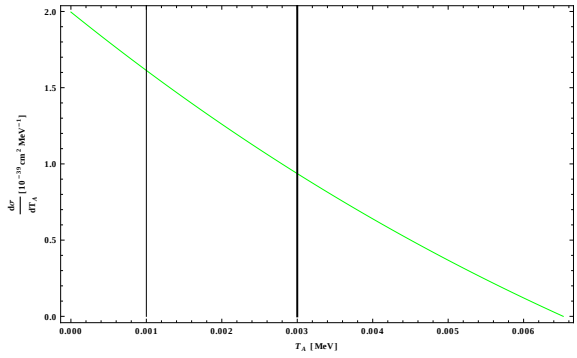

(d) Pinching factor $n_\nu = 3$

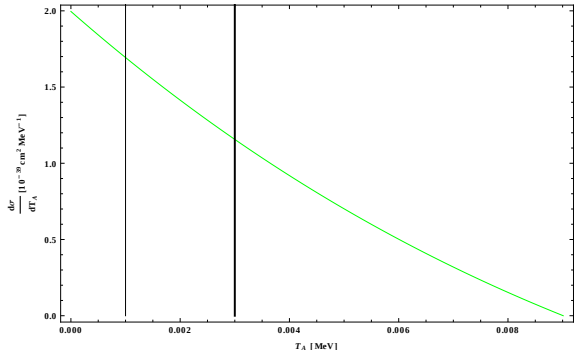

(e) Pinching factor $n_\nu = 4$

Figure 3.22: Differential cross $d\sigma/dT_A(T_A)$ for the ν_x flavors.The thin and thick vertical bars represent the $(T_A)_{thrs}$ and the threshold energy from the quenching factor.

(a) Total cross section for $(T_A)_{thrs} = 0\ keV$

n_ν	$\sigma_{tot}\ /10^{-39}\ cm^2$			
	ν_e $T = 3.5\ MeV$	$\bar{\nu}_e$ $T = 5\ MeV$	$\sum_x \nu_x$ $T = 8\ MeV$	Total
0	5.170	10.463	26.107	41.74
1	6.537	13.198	32.711	52.446
2	8.837	17.777	43.562	70.176
3	12.229	24.460	58.943	95.632
4	126.765	33.283	78.433	238.481

(b) Total cross section for $(T_A)_{thrs} = 1\ keV$

n_ν	$\sigma_{tot}\ /10^{-39}\ cm^2$			
	ν_e $T = 3.5\ MeV$	$\bar{\nu}_e$ $T = 5\ MeV$	$\sum_x \nu_x$ $T = 8\ MeV$	Total
0	0	0.039	10.151	10.190
1	0	0.861	16.008	16.869
2	0	3.555	26.122	29.677
3	0.471	8.753	40.923	50.147
4	2.870	16.528	60.004	79.402

(c) Total cross section for $(T_A)_{thrs} = 3\ keV$

n_ν	$\sigma_{tot}\ /10^{-39}\ cm^2$			
	ν_e $T = 3.5\ MeV$	$\bar{\nu}_e$ $T = 5\ MeV$	$\sum_x \nu_x$ $T = 8\ MeV$	Total
0	0	0	0	0
1	0	0	0.519	0.519
2	0	0	5.142	5.142
3	0	0	15.619	15.619
4	0	0.661	31.649	32.31

Table 3.7: Total cross sections of the $Neutrino - Xe$ elastic scattering for pinching factor values $n_\nu = 0 - 4$.

(a) Event rate for $n_\nu = 0$

$R\ [m]$	Number of events		
	$(T_A)_{thrs} = 0\ kev$	$(T_A)_{thrs} = 1\ kev$	$(T_A)_{thrs} = 3\ kev$
0.65	4	1	0
4	894	273	0
10	13968	4271	0

(b) Event rate for $n_\nu = 1$

$R\ [m]$	Number of events		
	$(T_A)_{thrs} = 0\ kev$	$(T_A)_{thrs} = 1\ kev$	$(T_A)_{thrs} = 3\ kev$
0.65	5	2	0
4	1063	417	13
10	16617	6512	207

(c) Event rate for $n_\nu = 2$

$R\ [m]$	Number of events		
	$(T_A)_{thrs} = 0\ kev$	$(T_A)_{thrs} = 1\ kev$	$(T_A)_{thrs} = 3\ kev$
0.65	6	3	1
4	1310	647	121
10	20461	10114	1888

(d) Event rate for $n_\nu = 3$

$R\ [m]$	Number of events		
	$(T_A)_{thrs} = 0\ kev$	$(T_A)_{thrs} = 1\ kev$	$(T_A)_{thrs} = 3\ kev$
0.65	7	4	2
4	1607	949	331
10	25108	14821	5179

(e) Event rate for $n_\nu = 4$

$R\ [m]$	Number of events		
	$(T_A)_{thrs} = 0\ kev$	$(T_A)_{thrs} = 1\ kev$	$(T_A)_{thrs} = 3\ kev$
0.65	8	6	3
4	1922	1295	605
10	30037	20234	9460

Table 3.8: Number of events for the different radii of the SPC .

n_ν	$(T_A)_{max}$ keV		
	ν_e $T = 3.5\ MeV$	$\bar{\nu}_e$ $T = 5\ MeV$	$\sum_x \nu_x$ $T = 8\ MeV$
0	0.522	1.066	2.728
1	0.662	1.350	3.457
2	0.823	1.832	4.690
3	1.249	2.549	6.525
4	1.725	3.520	9.011

Table 3.9: Maximum recoil energy $(T_A)_{max}$, for pinching factor values $n_\nu = 0-4$.

3.3.6 Conclusions

First of all we have to discuss the uncertainties due to differences in the astrophysical models of supernona explosions, hence in the emission spectra of neutrinos. If the equipartition of energy among the species is a widely accepted statement deriving from the universality of the interactions involved in Eq. (3.46) and Eq. (3.47), parameters such as the total energy of the explosion and the average energy, or the temperature, of the neutrinos spectra are much more uncertain. A variation in the total energy carried by the neutrinos has the trivial effect of changing linearly the number of neutrinos and hence the number of interactions in a given detector. The effect of a variation of the temperature of the spectra described in Eq.(3.48) must be discussed in more detail. A lower temperature corresponds to a red-shifted emission spectrum. Since the total energy content is the same, but the average energy is smaller,the number of emitted neutrinos is larger but a larger fraction of them will not be able to produce recoiling nuclei above threshold energy. Hence, the signal in the detector drops significantly. An increase of the temperature, on the contrary, leads to a higher maximum transferred energy between the incoming neutrinos and the recoiling nuclei. However, since the total number of neutrinos is smaller the signal increase is dumped and tends to saturate.

In the section above we can see what are the results, of the piching factor Eq. (3.48) variation. When the pinching factor is increased, the SN-neutrino emission spectra are widened. This variation (the temperature of each flavor is considered constant) does not change dramatically the number of emitted neutrinos or the mean neutrino energy, of each flavor, but the total cross section (folded cross section (3.53)) is significantly increased. This phenomenon is visible at the 3-dimensional plots of $d\sigma/dT(T_A, E_\nu)$. The energy spectra of the emitted neutrinos, are shifted towards greater values of neutrino energies. Thus, a larger fraction of the SN-neutrinos will produce recoil nuclei of higher energy. This is quite important as the rate of events, is significantly determined by the threshold of the detector.

Another important observation, is the different behaviour of light and heavy nuclei. Xenon has a much larger cross section than that of Argon, this was expected due of the squared neutron number factor (N^2) in Equation (3.42) . There is a price to be paid for the large cross section of Xenon, which is the low energy recoils, and thus in the presence of the threshold, a decrease of the event rate. The Spherical Proportional Counter (SPC) has the capability to reach a threshold

of $\sim 100\ keV$, that results (Fig.3.23, 3.24) in a significantly lesser event number loss, for both Argon and Xenon target nuclei.

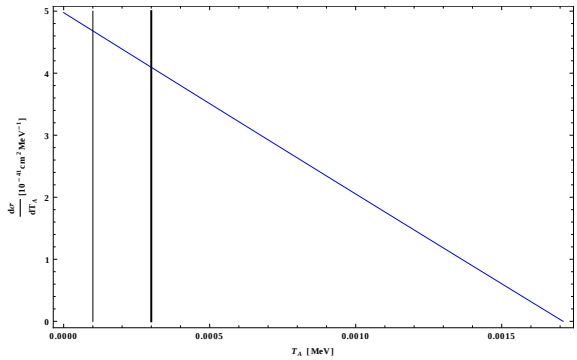

(a) ν_e flavor

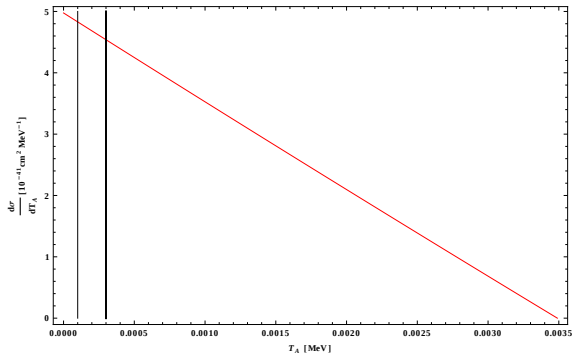

(b) $\bar{\nu}_e$ flavor

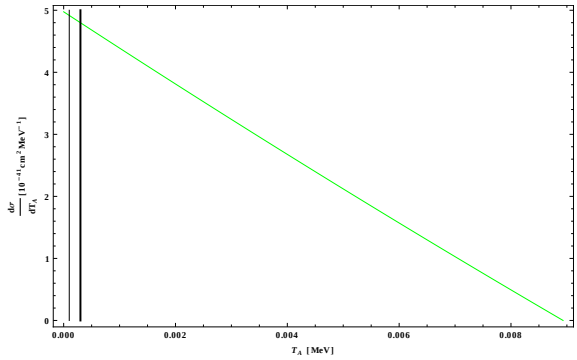

(c) ν_x flavor

Figure 3.23: Neutrino-Ar differential cross $d\sigma/dT_A(T_A)$ for every neutrino flavor (pinching factor $n_\nu = 0$). The thin and thick vertical bars represent the $(T_A)_{thrs}$ and the threshold energy from the quenching factor.

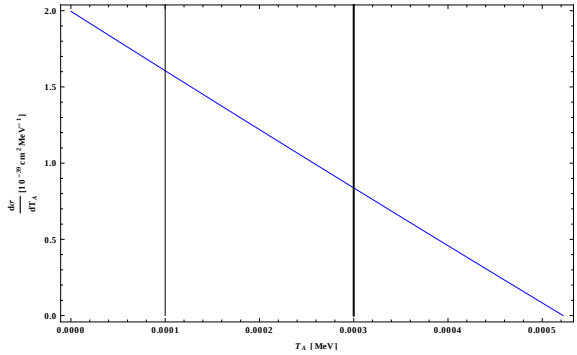

(a) ν_e flavor

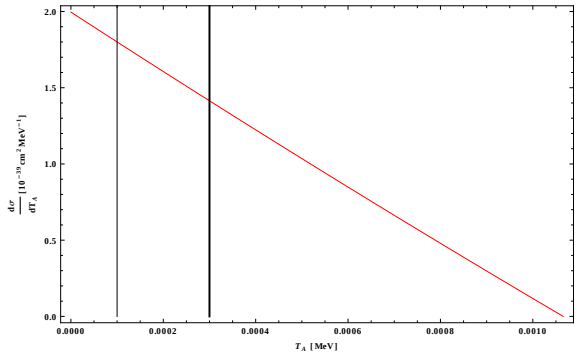

(b) $\bar{\nu}_e$ flavor

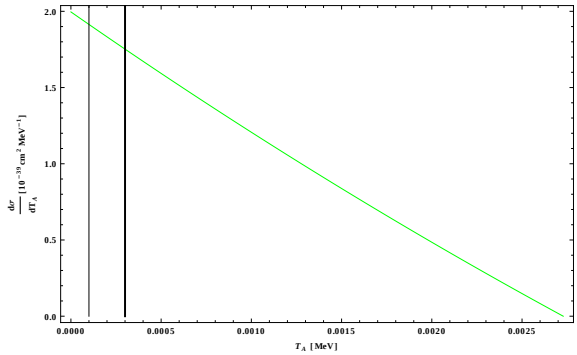

(c) ν_x flavor

Figure 3.24: Neutrino-Xe differential cross $d\sigma/dT_A(T_A)$ for every neutrino flavor (pinching factor $n_\nu = 0$). The thin and thick vertical bars represent the $(T_A)_{thrs}$ and the threshold energy from the quenching factor.

3.4 The Oak Ridge Spallation Neutron Source

Exploiting the neutral current interaction for detecting neutrino recoils, can be very usefull for the neutrino physics research. Due to the coherence of all neutrons in the nucleus one gets very large cross sections, which are proportional to the square of the neutron number (the coherent neutral current contribution due to protons is negligible). However to exploit this feature, one should design

large detectors with very low energy threshold, with well known capabilities. So, before we go to study, the emission of SN-neutrinos, with all the uncertainties they come with, it is important to study the behaviour of our detectors, using terrestrial neutrino sources with well known neutrino spectra.

One such source is Spallation Neutron Source (SNS) at the Oak Ridge National Laboratory, Oak Ridge, Tennessee, which is the most powerful source of pulsed intermediate-energy neutrinos. The spallation neutron source (SNS) will produce neutrons by firing a pulsed proton beam at a liquid mercury target. Among the fragments emitted will be pions. Negative pions will be captured in the target, but positive pions will come to rest and decay into positive muons and muon neutrinos. The muons will also come to rest and decay, emitting a positron, electron neutrino and muon anti neutrino. The pion decay time is 26 ns, and the muon decay time $2.2\mu s$. The neutrinos will be emitted isotropically from the target. The energy spectra of the ν_e and $\bar{\nu}_\mu$ are precisely known, since these neutrinos come from decay at rest; the ν_μ will be mono-energetic.
Their spectra can be calculated from the expression of the differential decay rate of the muon by integrating over the energies of the electron and $\bar{\nu}_\mu$ for the ν_e spectra, and integrating over the energies of the electron and ν_e for the $\bar{\nu}_\mu$ spectra. The normalized spectra are

$$f_{\nu_e}(E_{\nu_e}) = 96E_{\nu_e}^2 m_\mu^{-4}(m_\mu - 2E_{\nu_e}) \tag{3.60}$$

$$f_{\bar{\nu}_\mu}(E_{\bar{\nu}_\mu}) = 16E_{\bar{\nu}_\mu}^2 m_\mu^{-4}(m_\mu - 4E_{\bar{\nu}_\mu}) \tag{3.61}$$

The pulsed nature of the beam will be advantageous in reducing other types of background. The time difference for the emission of ν_e's and $\bar{\nu}_\mu$'s may also be used for distinguishing between events coming from these neutrinos and ν_μ's, as well as further reduction of background [17, 18].

The primary parameters of the SNS are as follows:
Proton beam power on target: 1.4 MW
Proton beam kinetic energy: 1.0 GeV
Average beam current on target: 1.4 mA
Protons per pulse on target: 1.5×10^{14}
Pulse repetition rate: 60 Hz
π^+ per proton: 0.068
π^+ per second 6.14×10^{14}
$R(\nu_e) = R(\bar{\nu}_\mu) = 6.14 \times 10^{14}$

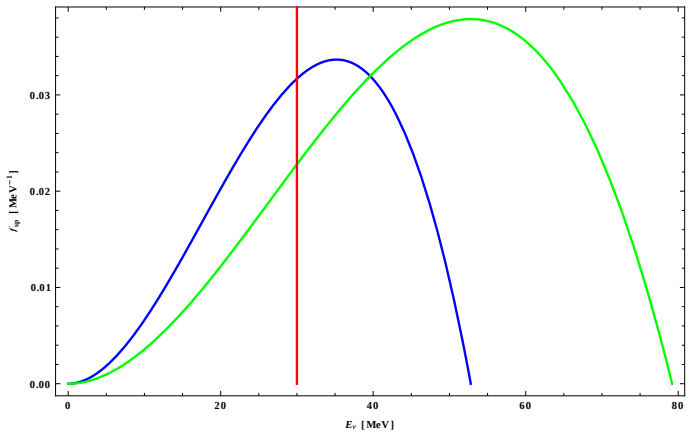

Figure 3.25: The normalized to unity SNS-neutrino spectra. The blue and green curves correspond to ν_e and ν_μ respectively. Also shown is the discreet $\bar{\nu}_\mu$ spectrum (red vertical line).

3.4.1 Cross sections and event rate

The differential cross sections for Ar and Xe as target nuclei, are obtained after folding with the neutrino spectra of Fig.3.25,the results are present at the following sections, as well as the total cross sections of this interactions. The number of expected events counted by the SPC of volume V, under pressure P and temperature T in a distance L takes the form

$$N_{ev} = \Phi(\nu, L)\sigma(A, N)\frac{PV}{kT}s(V, L) \tag{3.62}$$

where the parameter $s(V,L)$ is a geometrical factor needed when a large detector is close to the source. It depends on the shape of the vessel and the distance L of its geometric center from the source. In the case of sphere of radius R with its center at a distance d from the source the function $s(V,L)$ depends only on the ratio R/L, i.e. $s(V,L) \to s(R/L)$, and it is given by

$$s(R/L) = \frac{L^2}{(4/3)\pi R^3} 2\pi L \int_0^{R/L} x^2 dx \int_0^{\pi} \frac{sin\theta}{1+x^2+2xcos\theta} d\theta, \quad x = \frac{r}{L} \tag{3.63}$$

The above expression takes into account the fact that, if the sphere is close to the source, the neutrino flux is changing from point to point inside the sphere. Spherical coordinates (r, θ, ϕ), are used to specify any point inside the sphere. The origin of coordinates was chosen at the center of the sphere with polar axis the straight line from the source to the center of the sphere. With the above choice the flux is independent of the angle ϕ [17, 24]. The function $s(R/L)$ is given by

$$s(x) = \frac{3}{2x^3}\left(\frac{x^2-1}{2} ln\frac{1+x}{1-x} + x\right) \tag{3.64}$$

The geometric factor for the actual experimental set up, $L >> R$, is close to unity. Using

$$\Phi(\nu, L = 50\ m) = 1.95 \times 10^6 cm^{-2} s^{-1} \tag{3.65}$$

for each flavor we obtain the data of following tables.

3.4.2 Results for the Ar target

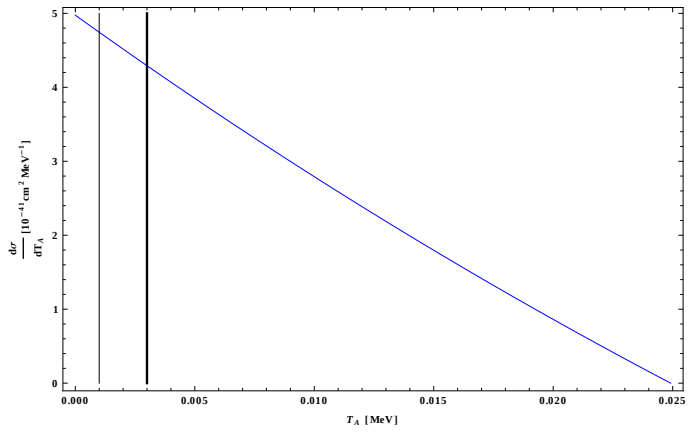

(a) ν_e flavor

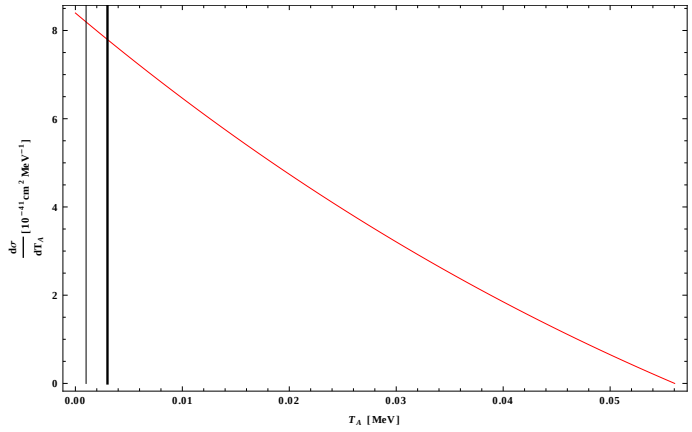

(b) $\bar{\nu}_\mu$ flavor

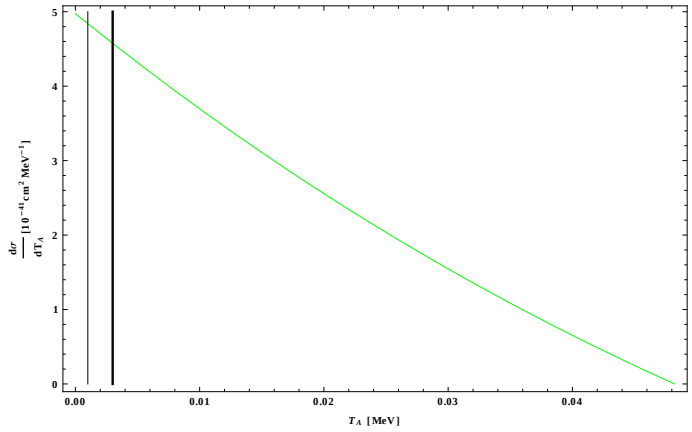

(c) ν_μ flavor

Figure 3.26: Neutrino-Ar differential cross $d\sigma/dT_A(T_A)$ for each neutrino flavor. The thin and thick vertical bars represent the $(T_A)_{thrs}$ and the threshold energy from the quenching factor.

$(T_A)_{thrs}[keV]$	σ_{tot} $/10^{-39}$ cm^2			
	ν_e $(T_A)_{max} = 7.61$ keV	$\bar{\nu}_\mu$ $(T_A)_{max} = 17.13$ keV	ν_μ $(T_A)_{max} = 14.74$ keV	Total
0	6.77	22.37	11.80	40.94
1	4.94	19.16	9.92	34.02
3	2.25	13.74	6.77	22.76

Table 3.10: Total cross section Neutrino-Ar interaction, for the SNS neutrino spectrum. The maximum neutrino recoil energy of each flavor are also presented.

$(T_A)_{thrs}[keV]$	Event rate /[yr]		
	ν_e $R = 0.65$ m	$\bar{\nu}_\mu$ $R = 4$ m	ν_μ $R = 10$ m
0	7097	$1.654 \cdot 10^6$	$2.584 \cdot 10^7$
1	5960	$1.375 \cdot 10^6$	$2.148 \cdot 10^7$
3	3947	$0.919 \cdot 10^6$	$1.437 \cdot 10^7$

Table 3.11: Number of events, for a Ar filled detector, for three different radii of the SPC, at $0,1,3$ keV thresholds. The event rate is for a detector at 10 atm of pressure, at temperature of 300^o K and at a distance of 50 m.

3.4.3 Results for Xe target nucleus

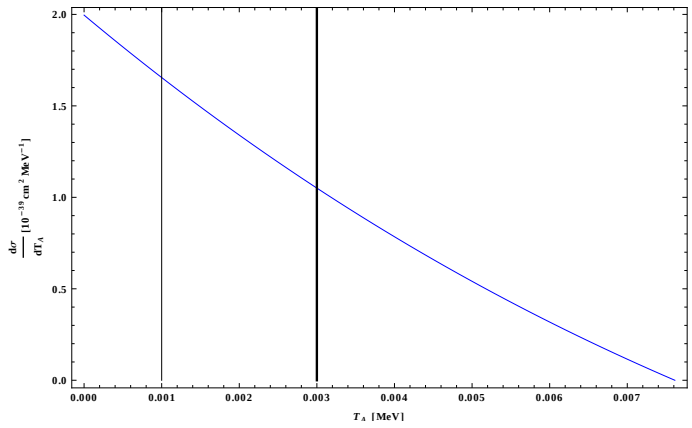

(a) ν_e flavor

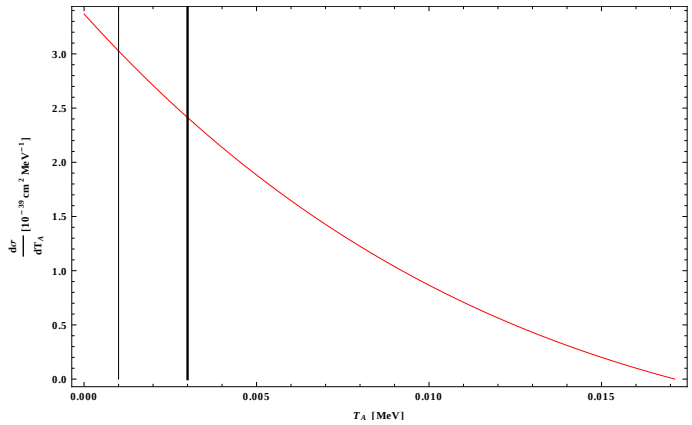

(b) $\bar{\nu}_\mu$ flavor

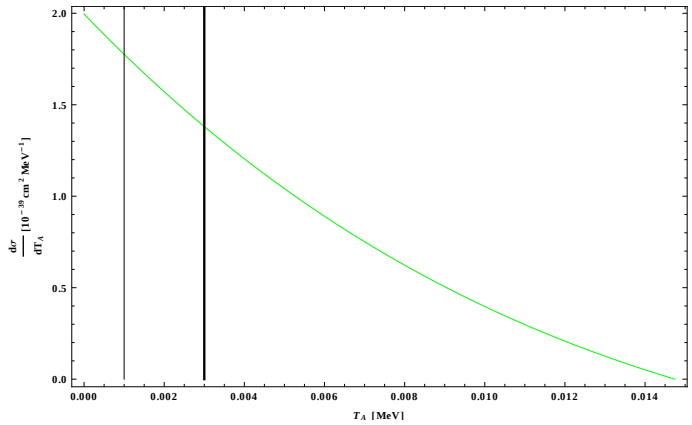

(c) ν_μ flavor

Figure 3.27: Neutrino-Xe differential cross $d\sigma/dT_A(T_A)$ for each neutrino flavor. The thin and thick vertical bars represent the $(T_A)_{thrs}$ and the threshold energy from the quenching factor.

$(T_A)_{thrs}[keV]$	$\sigma_{tot}\ /10^{-38}\ cm^2$			
	ν_e $(T_A)_{max} = 7.61\ keV$	$\bar{\nu}_\mu$ $(T_A)_{max} = 17.13\ keV$	ν_μ $(T_A)_{max} = 14.74\ keV$	Total
0	5.88	20.90	10.84	37.62
1	5.39	20.10	10.35	35.84
3	4.49	18.50	9.40	32.39

Table 3.12: Total cross section Neutrino-Xe interaction, for the SNS neutrino spectrum. The maximum neutrino recoil energy of each flavor are also presented.

$(T_A)_{thrs}[keV]$	Event rate /[yr]		
	ν_e $R = 0.65\ m$	$\bar{\nu}_\mu$ $R = 4\ m$	ν_μ $R = 10\ m$
0	652	$1.520 \cdot 10^5$	$2.236 \cdot 10^6$
1	621	$1.447 \cdot 10^5$	$2.262 \cdot 10^6$
3	561	$1.308 \cdot 10^5$	$2.044 \cdot 10^6$

Table 3.13: Number of events, for a Xe filled detector, for three different radii of the SPC, at $0,1,3\ keV$ thresholds. The event rate is for a detector at 10 atm of pressure, at temperature of $300^o\ K$ and at a distance of 50 m.

l	N_l^ν	E_l
^{235}U	1.92 ± 0.019	201.7 ± 0.6
^{238}U	2.38 ± 0.020	205.0 ± 0.9
^{239}Pu	1.45 ± 0.021	210.0 ± 0.9
^{241}Pu	1.83 ± 0.019	212.4 ± 1.0

Table 3.14: Total number of $\bar{\nu}_e$ per fission above 1.8 MeV and energy release per fission for the isotopes relevant in nuclear reactors. [28]

3.5 Nuclear Reactors as neutrino sources

Nuclear reactors make very convenient neutrino sources. Power reactors emit large numbers of antineutrinos, about 5×10^{20} $\bar{\nu}_e$ per second, broadly distributed over energies up to 10 MeV, with a peak at $0.5 - 1$ MeV [31]. Experiments at nuclear reactors have a long tradition in neutrino physics. Starting from the experimental discovery of the neutrino at the legendary Cowan-Reines experiment, many measurements at nuclear power plants have provided valuable information about neutrinos. For example, the results of the Gösgen, Bugey, Palo Verde, and CHOOZ experiments have lead to stringent limits on electron anti-neutrino disappearance. Building on the experience gathered in oscillation experiments ideas of "applied neutrino physics" appeared : A detector close to a nuclear reactor could be used for reactor monitoring, either for improving the reliability of operation of power reactors or as a method to accomplish certain safeguard requirements in the context of international treaties for arms control and non-proliferation of weapons of mass destruction [27].

In nuclear reactors the electrons antineutrinos in the energy range above the 1.8 MeV are produced dominantly by the beta decay of the fission products from the four isotopes $l = {}^{235}U, {}^{239}Pu, {}^{238}U, {}^{241}Pu$ (the flux from an isotope l is given by $\phi_l(E_\nu)$ in units of anti-neutrinos per fission and in MeV). In Table 3.14 the total number of $\bar{\nu}_e$ per fission above 1.8 MeV is given for ${}^{235}U, {}^{239}Pu, {}^{241}Pu$ and ${}^{238}U$. Accurate information on the anti-neutrino flux from ${}^{235}U$,${}^{239}Pu$, and ${}^{241}Pu$ can be obtained by the measurement of the beta spectra from the exposure of these isotopes to thermal neutrons. Subsequently these beta spectra have to be converted into anti-neutrino spectra, taking into account the large number of beta branches involved. These spectra are in excellent agreement with the direct observation of the anti-neutrino spectrum at the Bugey and Rovno reactors [27]. The errors on these fluxes are at the level of a few percent. Since modern reactor neutrino experiments aim at precisions at this level, a proper treatment of the flux uncertainties

becomes necessary. For ^{238}U, which does only undergo fast neutron fission, no similar measurements exist, and one has to rely on theoretical calculations. The number of events can be calculated by

$$N_{ev} = \frac{N_d}{4\pi L^2} \sum_l N_l^{fis} \int_{(T_A)_{thrs}}^{(T_A)_{max}} \int_{(E_\nu)_{min}}^{(E_\nu)_{max}} \frac{d\sigma}{dT_A} \phi_l(E_\nu) dE_\nu dT_A \tag{3.66}$$

Here N_d is the number density of the target nuclei in the detector and L is the distance between the reactor core and the detector. If the initial composition of the reactor fuel is known, the number of fissions per second N_l^{fis} of each isotope l can be calculated accurately (better than 1%) at each burn-up stage by core simulation codes. The thermal power output P of the reactor is given by $P = \sum_l N_l^{fis} E_l$, where E_l is the energy release per fission for the isotope l, see Table 3.14. Since the errors on E_l are less than 0.5% we will neglect in the following the uncertainty induced by them. Defining the relative contribution of the element l to the total power f_l, the N_l^{fis} can be expressed by P and Eq.(3.66) becomes

$$N_{ev} = \frac{N_d}{4\pi L^2} P \sum_l \frac{f_l}{E_l} \int_{(T_A)_{thrs}}^{(T_A)_{max}} \int_{(E_\nu)_{min}}^{(E_\nu)_{max}} \frac{d\sigma}{dT_A} \phi_l(E_\nu) dE_\nu dT_A \qquad with \qquad f_l = \frac{N_l^{fis} E_l}{P}. \tag{3.67}$$

The anti-neutrino spectra from the fission products of ^{235}U, ^{239}Pu and ^{241}Pu are determined by converting the precisely measured associated beta spectra. Based on these measurements we have a phenomenological parametrization for the reactor anti-neutrino flux.

3.5.1 Parametrization of the reactor anti-neutrino flux

We parametrize the spectrum of a given element using a polynomial:

$$\phi_l(E_\nu) = Exp\left(\sum_{k=1}^{K_l} a_{kl} E_\nu^{k-1} \right) \tag{3.68}$$

The coefficients a_{kl} are determined by a fit to the values, of the neutrino energy and the corresponding anti-neutrino flux, respectively [27, 31].

l	a_{1l}	a_{2l}	a_{3l}
^{235}U	0.904	-0.184	-0.0878
^{239}Pu	1.162	-0.392	-0.0790
^{241}Pu	0.852	-0.126	-0.1037
^{238}U	0.976	-0.162	-0.0790

Table 3.15: Coefficients of the polynomial of order 2 obtained from a fit to ν_e spectra. [31]

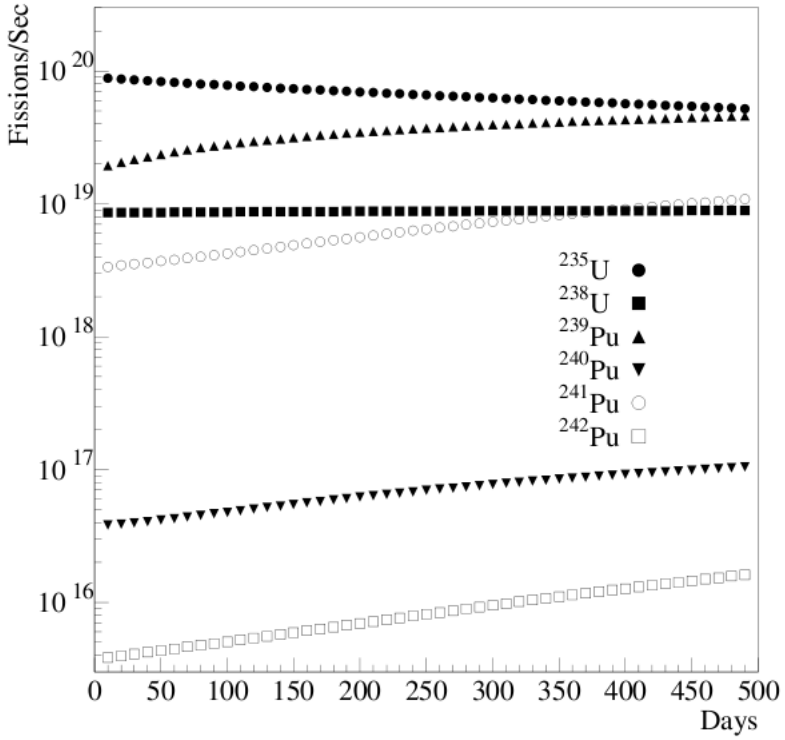

Figure 3.28: Time evolution of fission rates for each of the six most important isotopes the reactor core. The horizontal scale covers a full fuel cycle, at the end of which about 1/3 of the core is replaced with fresh fuel. Only the four most important isotopes are normally used to predict ν_e yields [25].

At the following tables we give the best-fit coefficients for the polynomials used to parameterize the anti-neutrino flux of the isotopes $^{235}U, ^{239}Pu$ and ^{241}Pu according to Eq. (3.68). In Table 3.15 the coefficients for the polynomial of order 2 are given, where in Table 3.16 we display the coefficients, their errors and the correlation matrix for the polynomial of order 5.

l	a_{1l}	a_{2l}	a_{3l}	a_{4l}	a_{5l}	a_{6l}
^{235}U	$3.519 \cdot 10^{0}$	$-3.517 \cdot 10^{0}$	$1.595 \cdot 10^{0}$	$-4.171 \cdot 10^{-1}$	$5.004 \cdot 10^{-2}$	$-2.303 \cdot 10^{-3}$
^{239}Pu	$2.560 \cdot 10^{0}$	$-2.654 \cdot 10^{0}$	$1.256 \cdot 10^{0}$	$-3.617 \cdot 10^{-1}$	$4.547 \cdot 10^{-2}$	$-2.143 \cdot 10^{-3}$
^{241}Pu	$1.487 \cdot 10^{0}$	$-1.038 \cdot 10^{0}$	$4.130 \cdot 10^{-1}$	$-1.423 \cdot 10^{-1}$	$-1.866 \cdot 10^{-2}$	$-9.229 \cdot 10^{-3}$

Table 3.16: Coefficients a_{kl} of the polynomial of order 5 for the anti-neutrino flux from elements $l = {}^{235}U, {}^{239}Pu$, and ${}^{241}Pu$ [27].

3.5.2 Cross sections and event rate

The differential cross sections for Ar and Xe as target nuclei, are obtained after folding with the total reactor anti-neutrino spectra of Fig.3.30(b), the results are present at the following sections, as well as the total cross sections of this interactions. The distance of the detector from the reactor core is considered $L = 100\ m$. The gas filling of the detector is at pressure $P = 10\ atm$, at temperature of $T = 300^{o}\ K$. The event rate is presented for SPC radii of $0.65, 4, 10\ m$ and recoil thresholds of 0 and 100 eV. The reason we must consider such low threshold is that the total reactor anti-neutrino spectra is consisted from neutrino energies of a few MeV, thus the nuclear recoils do not surpass the value of 1 keV. We consider that the reactor is in its initial burning cycle composition of 60.5% ^{235}U, 7.7% ^{238}U, 27.2% ^{239}Pu, and 4.6% ^{241}Pu [29]. As we can see from the figure 3.28, the isotope composition will change in its burning cycle, that will result in changes in the anti-neutrino flux. The reactor type is considered to be "N4" type (4 steam generators), with a thermal power of about 4.27 GW_{th}, and 1.5 GW_{e}. These are pressurized water reactors (PWR) and are fed with UO_x fuel [28].

Figure 3.29: Representation a "N4" type reactor.

(a)

$(T_A)_{thrs}$ $[eV]$	σ_{tot} $/10^{-41}$ cm^2
	$(T_A)_{max} = 0.36$ keV
0	8.825
100	4.551

(b)

$(T_A)_{thrs}$ $[eV]$	σ_{tot} $/10^{-41}$ cm^2
	$(T_A)_{max} = 0.115$ keV
0	107.65
100	0.2563

Table 3.17: Total cross section (a) Neutrino-Ar, (b) Neutrino-Xe interactions, for the total reactor anti-neutrino spectrum. The maximum neutrino recoil energies are also presented.

(a)

$(T_A)_{thrs}$ $[eV]$	Event rate /[yr]		
	$R = 0.65$ m	$R = 4$ m	$R = 10$ m
0	130850	$3.050 \cdot 10^7$	$4.779 \cdot 10^8$
100	67485	$1.573 \cdot 10^7$	$2.462 \cdot 10^8$

(b)

$(T_A)_{thrs}$ $[eV]$	Event rate /[yr]		
	$R = 0.65$ m	$R = 4$ m	$R = 10$ m
0	$1.596 \cdot 10^6$	$3.720 \cdot 10^8$	$5.823 \cdot 10^9$
100	3800	886023	$1.387 \cdot 10^7$

Table 3.18: Number of events, for an (a) Ar filled (b) Xe filled detector, for three different radii of the SPC, at $0,100$ eV thresholds. The event rate is for a detector at 10 atm of pressure, at temperature of 300^o K and at a distance of 100 m from the reactor core.

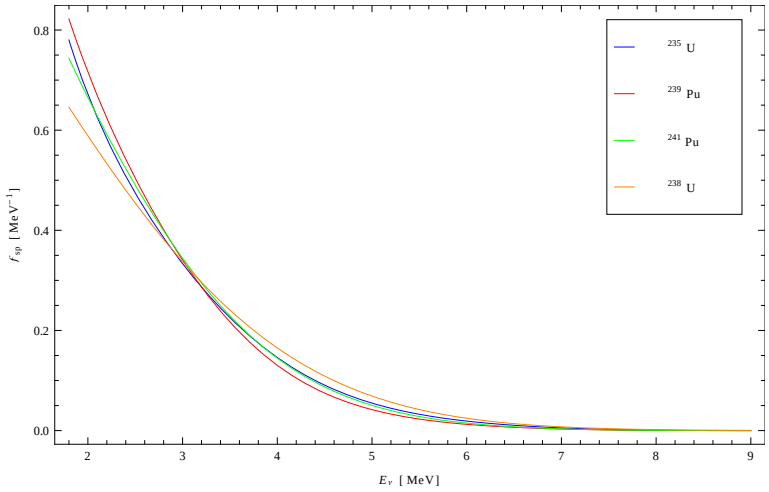

(a)

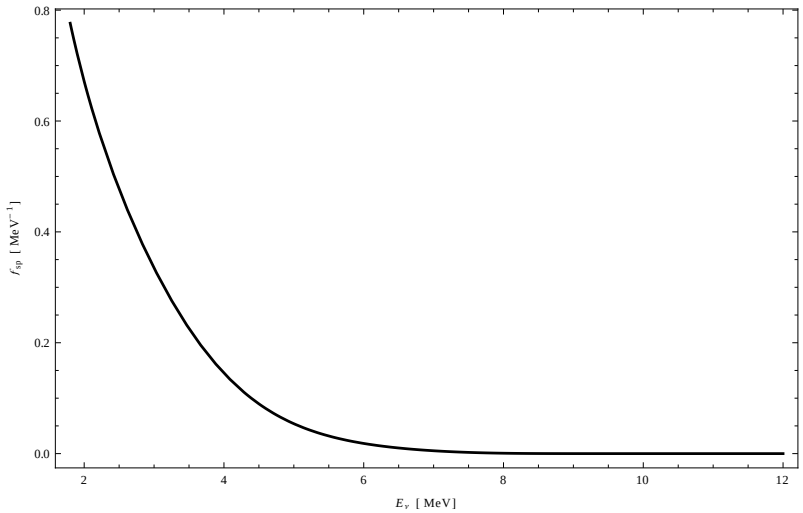

(b)

Figure 3.30: Reactor anti-neutrino spectra, (a) anti-neutrino spectrum of each isotope, (b) total anti-neutrino spectrum.

3.5.3 Observations

From the results on tables 3.16(a), 3.16(b), is obvious that if we want to exploit the neutrino-nucleus coherent elastic scattering for the detection of neutrinos from a nuclear reactor, the detector threshold must be lowered to the region of tenths of eVs, so that we have a measurable signal at the detector. The SPC has a threshold of about 100 eV, thus it is possible to detect efficiently neutrinos coming from nuclear reactors. The reactor neutrino detection is very important because it allows us to determine the isotopic composition of the reactor's core. This could lead to application of neutrino spectroscopy for reactor monitoring, either for improving the reliability of operation of power reactors or as a method to accomplish certain safeguard and non-proliferation objectives.

Chapter 4

Experimental procedure

4.1 Shielding study with FLUKA

4.1.1 Introduction

As aforementioned the purpose of this study is, whether, is possible to exploit he neutrino nucleus coherent scattering, for the detection of neutrinos through its nuclear recoils, using a gaseous detector. This nuclear recoils have very low energy (in the order of a few hundreds eV), so our detector must have high energy resolution, very low detecting threshold and most importantly high signal to noise ratio. To do that we must find ways to reduce the different types of background and noise and our experimental set up must be tested so that we can be sure that we can distinguish neutrino signal from all the rest. To test the SPC,we must use a kind of source that produces nuclear recoils in the gas area of our detector, at the desired energy area.This is accomplished using sources, that emit high neutron rates. The source used in our study is the $AmBe$ source. This source has a 6.6×10^4 per second neutron yield which is obtained through the reaction

$$ {}^{4}_{2}\alpha + {}^{9}_{4}Be \rightarrow {}^{12}_{6}C + {}^{1}_{0}n + 5.71\ MeV \tag{4.1} $$

which has also a $\sim 4.4\ MeV$ gamma ray emitted, from the deexcitation of ${}^{12}_{6}C$. The $AmBe$ source has the form of a metallurgically prepared alloy, where the Am is used as an alpha emitter and the beryllium as a target. Its alpha particle has the opportunity to interact with beryllium nuclei without any intermediate energy loss. The energy spectrum of the source is presented in Fig.4.1

As we mentioned above the neutron yield of this source, has an equal gamma ray yield, which interacting with the structural and shielding materials around the detector and the source casing, produces additional interfering radiation. This processes include Compton scattering, and the generation of secondary annihilation photons and characteristics X-rays through pair production or photoelectric

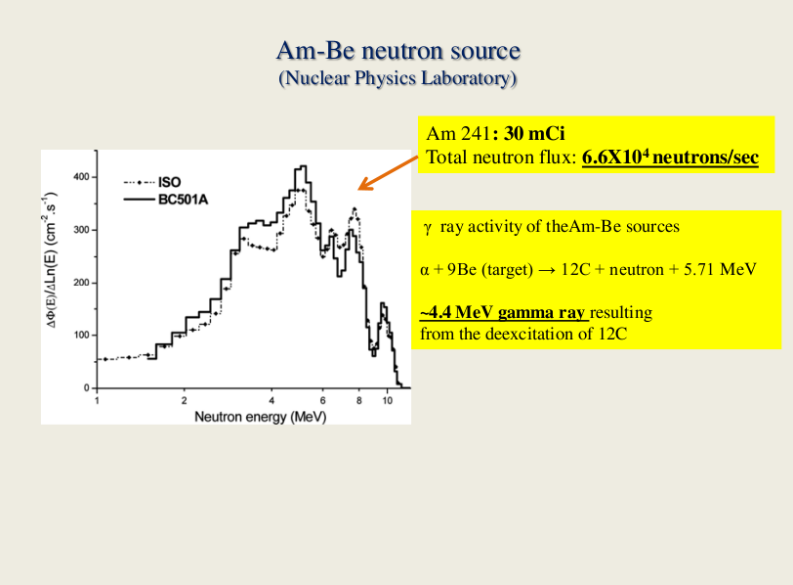

Figure 4.1: The energy spectrum of the *AmBe* source.

absorption. These effects could be avoided only by removing the materials from the vicinity of the detector, but practical demands do not permit this approach. The only solution is the shielding of the detector from this interfering radiation. The materials we use for shielding the detector is Lead and Steel.

Lead has a high density and large atomic number and for that is the material most often used for detector shields. The photoelectric absorption cross section predominates up to gamma ray energies up to 0.5 MeV, and therefore even hard gamma rays, from external sources can be absorbed efficiently. Because of its high density, thickness of just few centimeters, will provide a large reduction in the background of typical detectors. Lead is reasonably effective at removing many of the cosmic ray components of the background, although thicknesses beyond about 10 cm do not result in a appreciable decrease in the resulting counting rate because of the build up of secondary radiations, due to cosmic rays interactions with the lead itself.

Steel is also common gamma ray shielding material and is often used in situations where the size or configuration of the shield would make its construction from lead alone too expensive. In such circumstances, an outer layer of steel with an inner lead lining is often an effective compromise. Because both the atomic number and density of steel are considerably lower than those of lead, thicknesses of several tens of centimeters are normally required for very low background applications.

The choice of shielding for a detector is not straightforward, as the shielding must fulfil the demands of each experiment. The shielding in our experimental

setup must :

- Allow the greater neutron fraction possible to pass through and at the same time suppress the number of photons in a large degree.
- The energy deposited by neutron events inside the gas area of the the detector, must be greater than the energy deposited by photons, i.e. the supression of the photon number is not enough, because of the nature of the electromagnetic interaction, which allow even few number of photons, passing through the shielding to produce important interference.

For the study of the characteristics and results of a each type of shielding, a simulation of the irradiation of the detector with neutrons and gamma rays was performed, using FLUKA.

4.1.2 Radiation transport code FLUKA

FLUKA is a general purpose tool for calculations of particle transport and interactions with matter, covering an extended range of applications spanning from proton and electron accelerator shielding to target design, calorimetry, activation, dosimetry, detector design, Accelerator Driven Systems, cosmic rays, neutrino physics, radiotherapy etc. FLUKA uses sound and modern physical models. Microscopic models are adopted whenever possible, consistency among all the reaction steps and/or reaction types is ensured, conservation laws are enforced at each step, results are checked against experimental data at single interaction level. As a result, final predictions are obtained with a minimal set of free parameters fixed for all energy/target/projectile combinations. Therefore results in complex cases, as well as properties and scaling laws, arise naturally from the underlying physical models, predictivity is provided where no experimental data are directly available, and correlations within interactions and among shower components are preserved.

Some important features of FLUKA we used and are important part of our study are:

- transport of electrons, positrons and photons (EMF on)
- Rayleigh scattering and inelastic form factor corrections to Compton scattering activated
- Detailed photoelectric edge treatment and fluorescence photons activated
- Neutron multigroup transport and interactions in the range $0-20\ MeV$

- Fully analogue absorption for neutrons in the range $0-20\ MeV$
- Particle transport threshold set at $1\times m_{part}/m_{prot}\ MeV$, except neutrons (19.6 MeV)
- Restricted ionisation fluctuations on, for both hadrons/muons and EM particles
- Heavy fragment transport activated

The transport of electromagnetic particles is somewhat problematic because of the increase of the computing time when the transport cut is set low, so the energy cuts for electrons and photons were set at $100\ eV$, which is the detection threshold of the SPC.

4.1.3 Neutron transport in FLUKA

Transport of neutrons in FLUKA with energies lower than $20MeV$ is performed by a multigroup algorithm. The multi-group technique,is widely used in low-energy neutron transport programs. The energy range between $10^{-5}\ eV$ and 19.6 MeV is divided into 260 energy groups of approximately equal logarithmic width, 31 of them thermal . Elastic and inelastic reactions are simulated not as exclusive processes, but by group-to-group transfer probabilities forming the so-called downscattering matrix.

The scattering transfer probability between different groups is represented by a Legendre polynomial expansion truncated at the $(N+1)^{th}$ term, as shown in the equation:

$$\sigma_s(g\rightarrow g',\mu)=\sum_{i=0}^{N}\frac{2i_1}{4\pi}P_i(\mu)\sigma_s^i(g\rightarrow g') \tag{4.2}$$

where $\mu=\Omega\cdot\Omega$ is the scattering angle and N is the chosen Legendre order of anisotropy. The angular probabilities for inelastic scattering are obtained by a discretisation of a $P5$ Legendre polynomial expansion of the actual scattering distribution which preserves its first 6 moments.

4.1.4 Radiation units used in FLUKA

In radiation background calculations, the rates of particles in a given detector region are quantified in terms of flux, or current. These two quantities have the dimensions of number/unit-time/unit-area, but they do not have the same meaning. Flux counts the rate of arrivals per unit area independent of the particle direction and its real physical meaning is that of path density, whereas current

counts the rate crossing through a given plane, referred to area elements in the surface of the plane. The importance of flux is that if one considers lengths in mean free paths for a given reaction, then the path density is just equal to the reaction density. To measure lengths in mean free paths means to multiply the lengths in cm by the cross section and by the atom density. Thus, every time we want to score a quantity which is proportional to any effect which has a cross section, or a mean free path, we must score flux. Current is meaningful only for counting particles independent of any effect they may produce in matter. In FLUKA flux is defined either as the track-length of a particle per unit of volume, or as the number of particles hitting a sphere of unit cross-section per unit time and its unit can be expressed as ($cm^{-2}s^{-1}$). Fluence is the time integral of flux expressed in units of (cm^{-2}). Only in the special case of normal incidence on a flat surface the flux is equal to the number of particles crossing a unit surface. For particles arriving at an angle to a flat surface the flux is the number of particles crossing a unit surface per unit of time weighted by ($1/cos\theta$), where θ is the angle with respect to the normal of the surface. A star is a hadronic inelastic interaction (spallation reaction) at an energy higher than a user-defined threshold (or by default higher than the transport threshold of the interacting particle). Star scoring (traditionally used in most high-energy shielding codes) can therefore be considered as a form of crude collision estimator: multiplication of the star density by the asymptotic value of the inelastic nuclear interaction length gives the fluence of hadrons having energy higher than the current threshold. Selecting star scoring is meaningful for hadrons, photons and muons (if their energy is sufficiently high). Any other particle will not produce any star. Moreover, in FLUKA stars do not include spallations due to annihilating particles. The results are expressed in stars/cm^3 /primary particle. The scoring by regions enables the calculation of the energy deposition in different detectors represented by different regions. Energy deposition is expressed in GeV/cm^3 /primary particle. To obtain doses (in Gy per unit primary particle), the results must be multiplied by ($10^{12} \times e/\rho \times V$), where ρ is the material density in g/cm^3 , e the electron charge in C and V the volume of the region in cm^3 . The fluence of charged particles and the absorbed dose, are correlated for a given particle type and energy in a given medium. Assume a minimum ionizing particle passing through an object and interacting only by dE/dX energy loss due to ionization. The damage will depend on accumulated track-length, even in the case of very thin detectors, and the damage scales with the flux, since the accumulated track-length does not depend on orientation. For charged particles, track-length is proportional to the energy deposited ($Edep = L \times S$,where L is the tracklength and S=dE/dX is the stopping power). To sum up, star density by producing particle and region as well as energy de- position by region,

total or from electrons/photons only can be scored. Moreover, fluence and current scoring as a function of energy can be done via boundary- crossing, collision and track-length estimators coincident with regions or region boundaries.

4.1.5 Implementation of SPC shielding in FLUKA

FLUKA simulation was used to study six types of shielding, the material used were blocks of lead and steel separately and combinations of them, the copper shell of the SPC was also studied as a shielding. The six types of shielding area

1. Copper shell of 6 *mm* thickness
2. Steel block of 5 *cm* thickness
3. Lead block of 5 *cm* thickness
4. Lead block of 9 *cm* thickness
5. Lead block of 5 *cm* thickness plus a steel block of 5 *cm* thickness
6. Lead block of 9 *cm* thickness plus a steel block of 5 *cm* thickness

The AmBe source was simulated using the SOURCE command. The irradiation of the detector with neutrons and gamma rays, was performed in separate runs. The reason is, that the energy deposition by neutrons and gamma rays, as well as the number of events of their interactions, must be calculated separately. The criteria used for shielding efficiency are the ratio between the total energy deposited by neutron and gamma rays, and the ratio between the number of events of neutrons and gamma rays interactions with the argon gas fill.

The geometry used is composed from the following regions:

- Spherical copper shell of 6 *mm* thickness, with a 65 *cm* inner radius
- Argon gas filling at 100 *mbar* pressure
- Shielding (30 $cm \times 30$ *cm* blocks)

the AmBe source is considered at a distance of 90 *cm* from the center of the sphere.

The FLUKA command EVENTDAT was also used. EVENTDAT records every energy deposition event by event, in every area defined. The data were recorded in a binary file, which was later can read using a script A.4, keeping only the events in the gas region. The energy spectra of the neutrons and gamma rays crossing the copper shell and pass into the gas area, were calculated using the

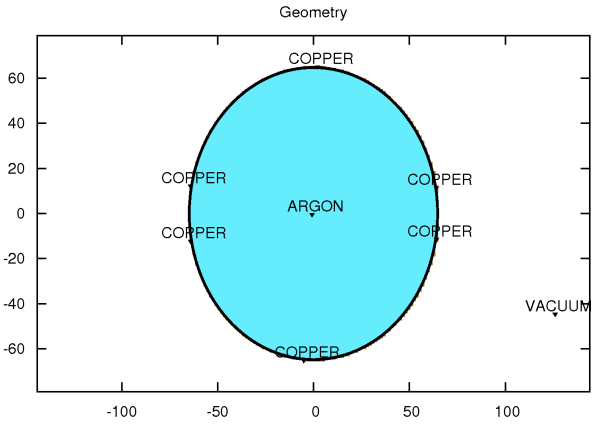

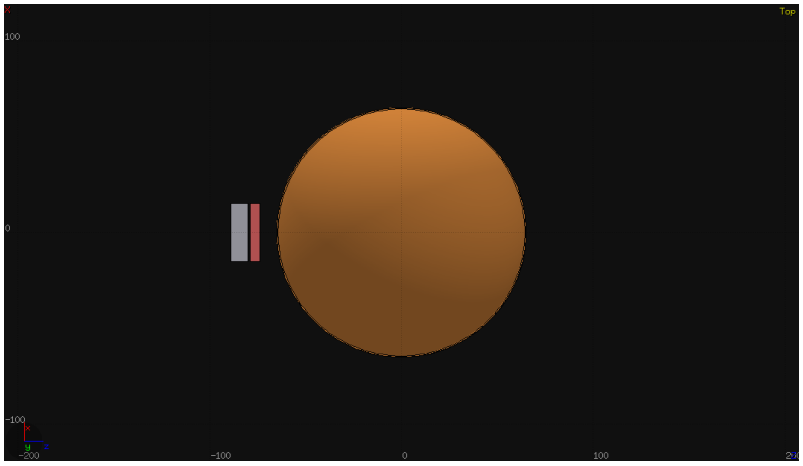

Figure 4.2: Sketch of the geometry and the defined regions, the axes are in centimeters

USRDBX command (FLUKA boundary crossing estimator). Finally the spatial distribution of the neutrons (gamma rays) fluence and the neutrons (gamma rays) energy deposition was scored using the USRBIN command (with WHAT(2) NEUTRON (PHOTON) or ENERGY respectively).

		Total energy deposition keV per primary		$EnDep_n/EnDep_\gamma$
Number	Shielding	Neutrons	Gamma rays	Ratio
1	Cu 6 *mm* (only the shell)	2.920E-2	4.100E-1	0.0712
2	Steel 5 *cm*	9.563E-2	1.600E-1	0.598
3	Pb 5 *cm*	9.999E-2	5.066E-2	1.974
4	Pb 9 *cm*	1.136E-1	4.125E-3	27.539
5	Pb 5 *cm*+Steel 5 *cm*	5.352E-1	1.909E-2	28.035
6	Pb 9 *cm*+Steel 5 *cm*	4.307E-2	3.705E-3	11.624

Table 4.1: The total energy deposition normalized by the number of source particles emitted, for the neutrons and the gamma rays, and their ratio $EnDep_n/EnDep_\gamma$.

		Number of events per primary		N_n/N_γ
Number	Shielding	Neutrons	Gamma rays	Ratio
1	Cu 6 *mm* (only the shell)	2.448E-3	24.60E-3	0.101
2	Steel 5 *cm*	1.932E-3	8.160E-3	0.024
3	Pb 5 *cm*	1.604E-3	2.480E-3	0.647
4	Pb 9 *cm*	1.128E-3	0.320E-3	3.525
5	Pb 5 *cm*+Steel 5 *cm*	1.176E-3	1.200E-3	0.980
6	Pb 9 *cm*+Steel 5 *cm*	0.840E-3	0.240E-3	3.500

Table 4.2: Total number of events normalized by the number of source particles emitted, for the neutrons and the gamma rays, and their ratio N_n/N_γ.

		Events per second	
Number	Shielding	Neutrons	Gamma rays
4	Pb 9 *cm*	74	21
5	Pb 5 *cm*+Steel 5 *cm*	78	79
6	Pb 9 *cm*+Steel 5 *cm*	55	16

Table 4.3: The event detection rate in events per second for the neutron and the gamma ray interactions.

		Energy deposition keV per event	
Number	Shielding	Neutrons	Gamma rays
4	Pb 9 *cm*	100.7	12.9
5	Pb 5 *cm*+Steel 5 *cm*	455.1	15.2
6	Pb 9 *cm*+Steel 5 *cm*	51.3	4.4

Table 4.4: The event detection rate in events per second for the neutron and the gamma ray interactions.

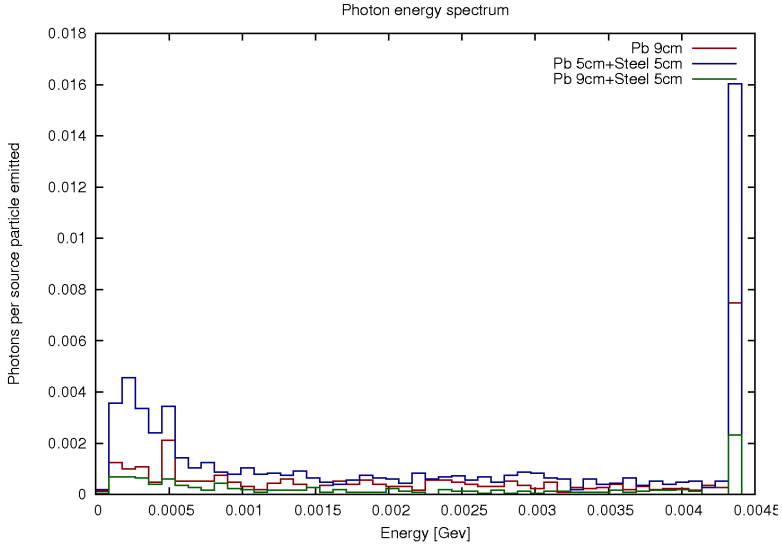

(a) Photons per primary source photon emitted

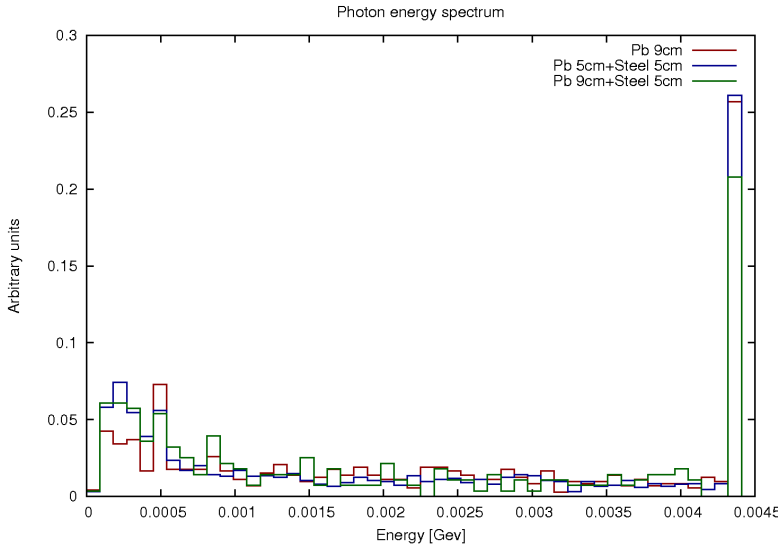

(b) Photon spectrum normalized to unity

Figure 4.3: Energy spectrum of the photons that pass through the shielding and enter into the gas area. The last energy bin contains the initial particles remaining.

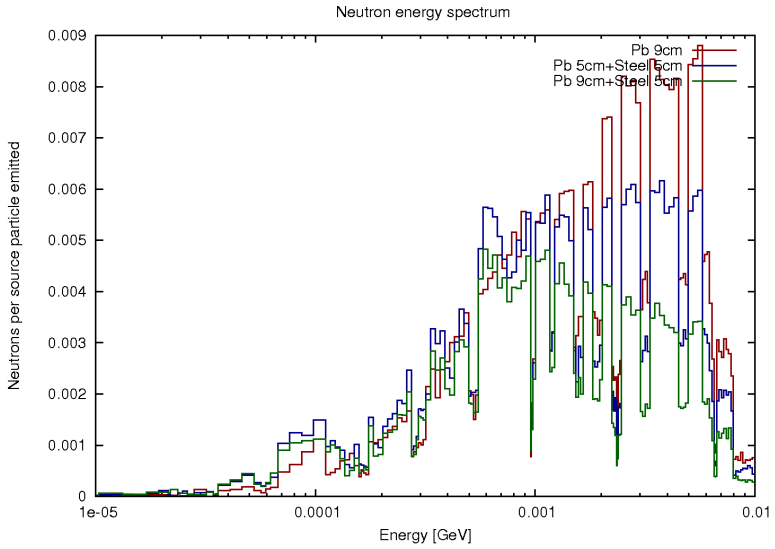

(a) Photons per primary source photon emitted

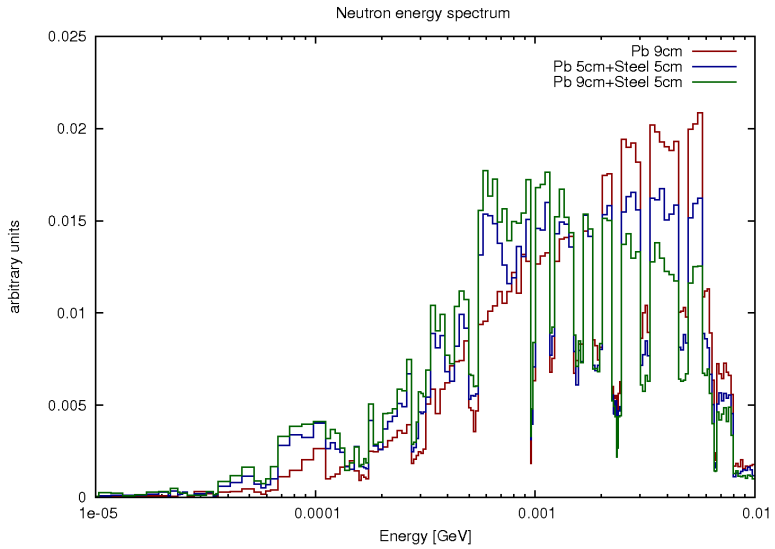

(b) Photon spectrum normalized to unity

Figure 4.4: Energy spectrum of the photons that pass through the shielding and enter into the gas area.

4.1.6 Conclusions

The first three types of shielding of Tables 4.1 and 4.2, must be excluded from further study, the reason is that the energy deposition and the event rate, in the gas area is dominated by the interactions of photons against the neutron ones. The fifth type of shielding (Pb 5 cm plus steel 5 cm) is special because as we can see the energy deposition of neutrons is far greater than that of the photons, but the event rate is the same for both of them, it allows a high percent of the initial gamma to pass. The cause of this phenomenon is that, as we can see Fig.4.3(a), we have more photons at the lower energy regions of the spectrum (below 100 keV), were the gamma ray attenuation coefficient has much greater values, than the values at the MeV region.

The shieldings types three and six (Pb 9 cm and Pb 9 cm+Steel5 cm) are those which suppress, in a large degree the gamma event rate and energy deposition, in comparison with that of neutrons, Tables 4.1 and 4.2. This type shielding seem to have similar behaviour with the difference that type six, has worse energy depositon ratio, but similar event rate ratio, in comparisom with that of type three. For this two types of shielding, the detector's response was calculated, in the form of normalized energy deposition spectra presented at Fig.4.6. As we can see the greater fraction of recoil events is at the energy region of $0-60$ keV. This may struck as abnormal but if we look at the differential neutron-Argon elastic scattering cross section Fig.4.5(b) scatterings at small angles (low energy recoils) are preferred.

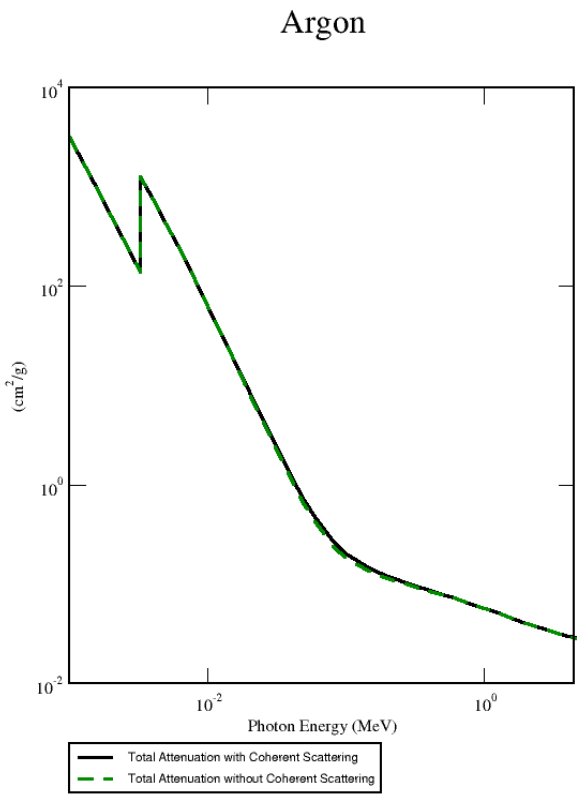

(a) Photon cross section data for Argon

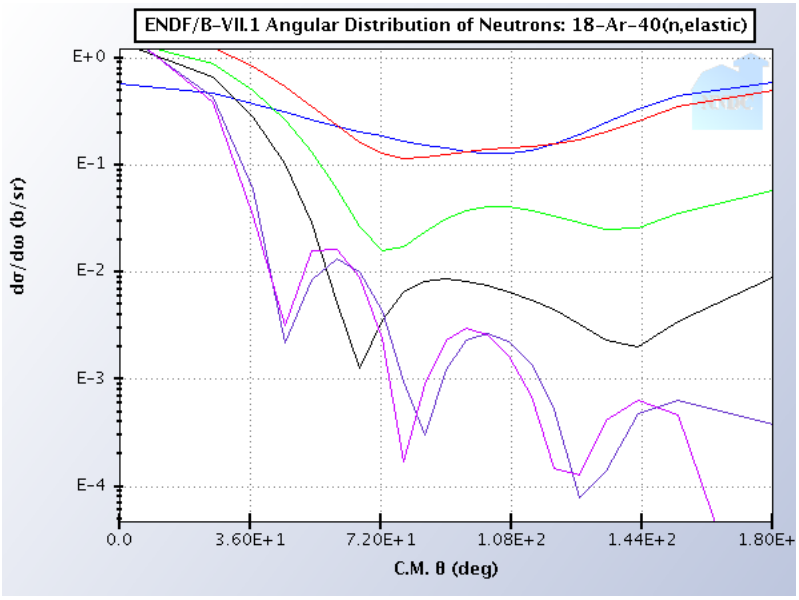

(b) Neutron differential cross section for Argon

Figure 4.5: (a) The photon total attenuation cross section [53] and (b) the neutron-argon elastic scattering differential cross section for 1 MeV (blue), 2.4 MeV (red), 5 MeV (green), 8 MeV (black), 15 MeV (purple), 1 MeV (violet) [54].

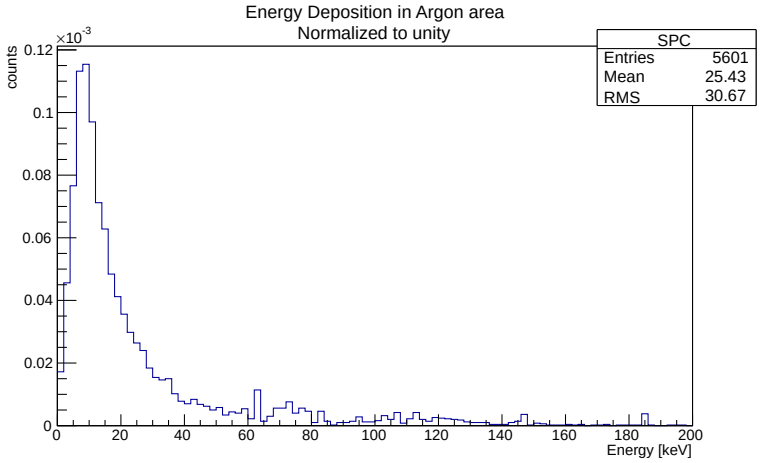

(a) Shielding type 3 (Pb 9 *cm*)

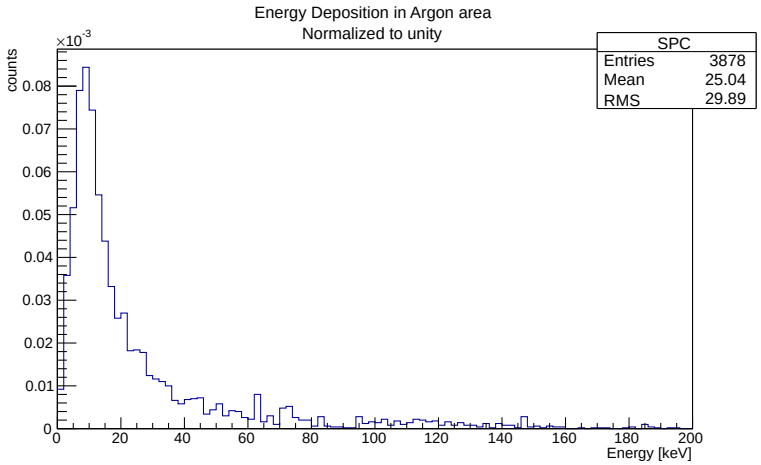

(b) Shielding type 4 (Pb 9 *cm*+Steel5 *cm*)

Figure 4.6: Energy spectrum of the photons that pass through the shielding and enter into the gas area.

4.2 Event Discrimination

4.2.1 Data Collection

The signal coming from the interactions, inside the volume of the SPC is collected through the sensor and is driven to the preamplifier. The exit of the preamplifier is connected with the ADC. The ADC processes every pulse separately and records them at the hard drive of the computer. This data are converted using the TANGO program, in the form of an NTUPLE ascii format file for further analysis. The variables recorded by the ADC through TANGO are the amplitude, the rise time, the duration, and baseline of the pulse. The time moment from the beginning of the running of every pulse is also recorded Fig.4.7.

```
root [4] ***************************************************************************************************
*    Row   *    numero *      date *     delai *      ampl *      base *     bruit *    montee *     duree *
***************************************************************************************************
*        0 *         1 * 0.0292760 *         0 * 1983.9599 * -2089.959 * 37.821998 * 0.0175001 * 0.2763180 *
*        1 *         2 * 0.0588640 * 0.0295880 * 6212.9599 * -3756.959 * 30.528699 * 0.0183662 * 0.3153649 *
*        2 *         3 * 0.0741999 * 0.0153360 * 8192.0302 * -2237.030 * 10.392299 * 0.0180412 * 0.3024649 *
*        3 *         4 * 0.1562470 * 0.0820470 * 1699.2700 * -1627.270 * 9.7724103 * 0.0171333 * 0.3122439 *
*        4 *         5 * 0.3822839 * 0.2260369 *   9523.25 *  -1844.25 * 31.622800 * 0.0173495 * 0.2945429 *
*        5 *         6 * 0.4025979 * 0.0203140 * -1219.329 * -321.6730 * 310.15100 * 0.2858040 * 0.4666450 *
*        6 *         7 * 0.4730750 * 0.0704770 * 4473.2998 * -1899.300 * 155.64100 * 0.0162592 * 0.2554920 *
*        7 *         8 * 0.5294799 * 0.0564050 * 3525.1201 * -2457.120 * 86.072601 * 0.0164298 * 0.2786999 *
*        8 *         9 * 0.5519329 * 0.0224530 *   2028.75 *  -1825.75 * 9.4074401 * 0.0165668 * 0.3053700 *
*        9 *        10 * 0.5728049 * 0.0208720 * 7587.2402 * -2804.239 * 10.931599 * 0.0160725 * 0.2993389 *
*       10 *        11 * 0.5805619 * 0.0077570 * 4388.9502 * -3301.949 * 34.727500 * 0.0170968 * 0.3255760 *
***************************************************************************************************
```

Figure 4.7: The different variable of the signal recorded by the ADC.

4.2.2 Definition of the rise time and the duration of the pulse

The preamplifier provides a pulse with no shaping, and its output is a linear tail pulse. The linear tail pulse is the kind of generated when the output of the radiation detector is collected across an equivalent circuit of large time constant. The leading edge of the pulse corresponds to the time over which the produced charge by the detector is integrated across the capacitance of the collections circuit. Therefore, the time characteristics of the leading edge are determined exclusively by the charge collection time within the detector. The decay of the pulse is determined by the time constant of the collection circuit. In order to assure complete collection or to avoid ballistic deficit, this time constant must be large compared with the detector charge collection time. For linear tail pulses, the most significant parameter besides the amplitude is the rise time of the leading edge of the pulse. The rise time of the pulse is defined as the interval between the times at which the pulse reaches 10% and 90% of its final amplitude. The duration of the pulse is the full width at half maximum amplitude (FWHM) [42]. The pulse rise time and duration are strongly correlated and follow the relation

$$Fall-time = Duration - 0.5 \times Rise\ time \approx RC\ amplifier \tag{4.3}$$

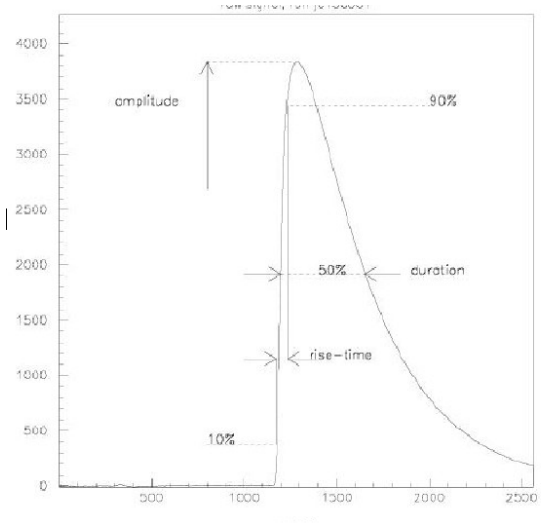

Figure 4.8: The shape and parameters of a typical pulse.

This parameters contain all the physics information we can get from the pulse. This information are used in the analysis of the data analysis in a form of biparametric plot, amplitude versus rise time. With the help of this plot we can discriminate events coming from different types of interaction of radiation with the gas fill. Nuclear recoils are produced from the elastic collisions of neutrons with the gas atoms. This recoils travel a distance of a few μm inside the gas volume, and consequently have a very low rise time. Electromagnetic radiations interact with matter in a different way. Energetic electrons loose the energy after they travel a much greater distance, hence their rise time depending on their energy will have larger values. Therefore by measuring the rise time of the pulse we have a way to discriminate between events, as we can see at Fig.4.9.

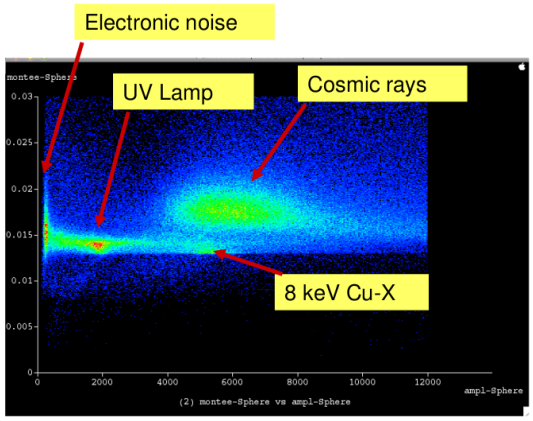

(a)

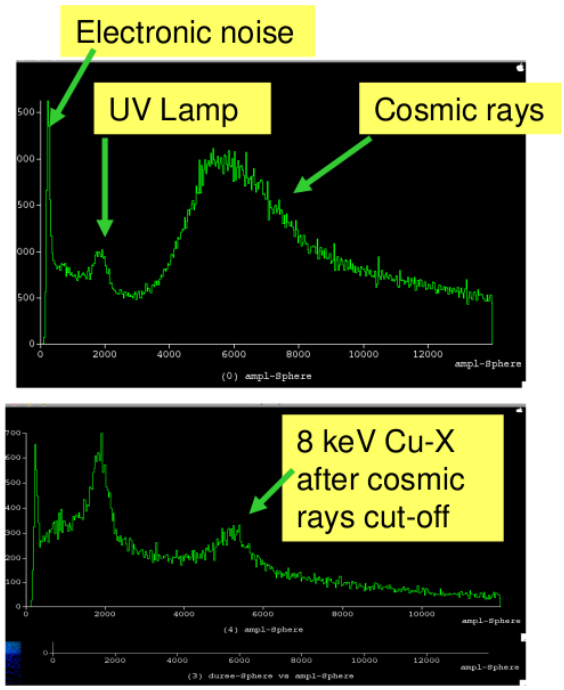

(b)

Figure 4.9: An amplitude versus rise time, biparametric plot. The gas fill is $Ne + 5\%\ CH_4$, at pressure $P = 500\ mbar$. The different types of radiations are discriminated [34].

4.2.3 Example event run

Here we present a typical run, there were two measurement both of 1500 sec. The gas fill was at pressure $P = 30\ mbar$. The first measurement was performed without the use of any sources to measure the background. The second measurement was perfomed using the *AmBe* source. The expected event rate count from

radiation of the source is calculated using the relationship

$$Rate = \frac{N_{S+B}}{t_{S+B}} - \frac{N_B}{t_B} \tag{4.4}$$

where N_{S+B} is the number of events coming from the background and the source, N_B is the number of events coming from the background alone, t_{S+B} and t_B are the measurement times for the background and the source measurement and the background alone measurement respectively. Using (4.4) we expect ~ 200 source events, coming from the neutrons and the gamma rays of the *AmBe* source. Using the list of variables provided by TANGO we can discriminate between the neutron events and the rest radiation events, performing rise time, duration and amplitude cuts. The results of the data analysis of this event run are presented at the following section.

Data analysis results

Here we present the analysis results with no cuts performed.

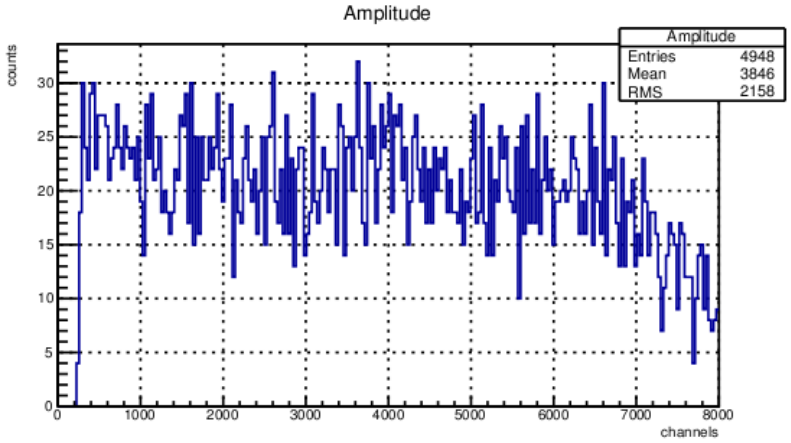

(a) Background

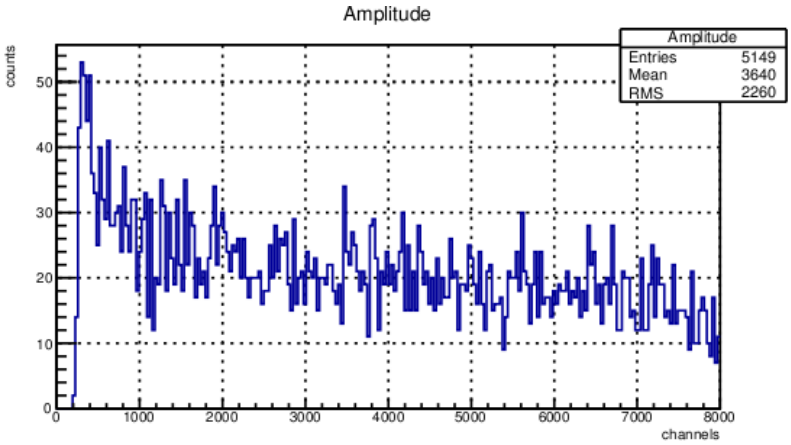

(b) *AmBe*+ Source plus Background

Figure 4.10: Amplitude spectra for (a) the background measurement and (b) the Source plus Background measurement. The visible difference is the low low energy events, were the neutrons events were expected to be.

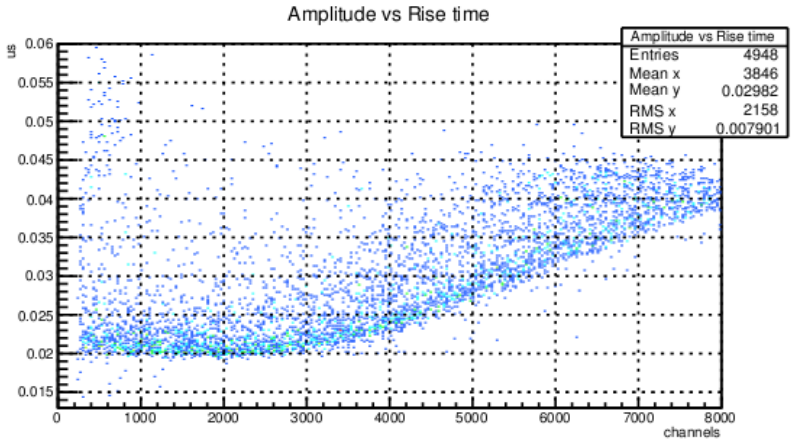

(a) Background

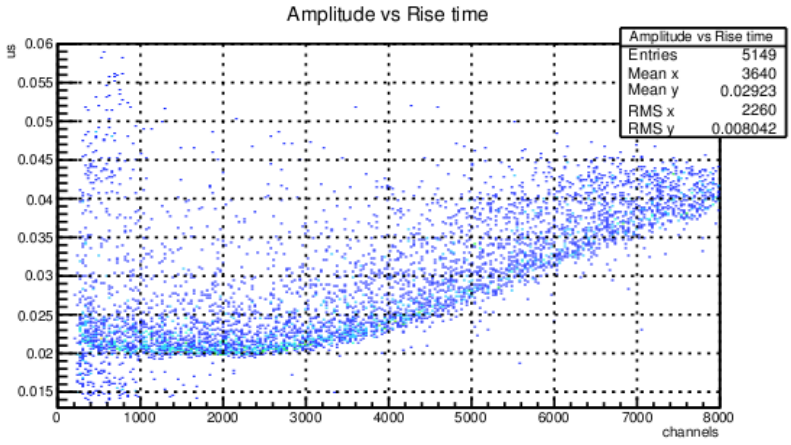

(b) *AmBe*+ Source plus Background

Figure 4.11: Amplitude vs rise time 2D histogram for (a) the background measurement and (b) the Source plus Background measurement. The difference between the two plot is expected to be at the low rise time area.

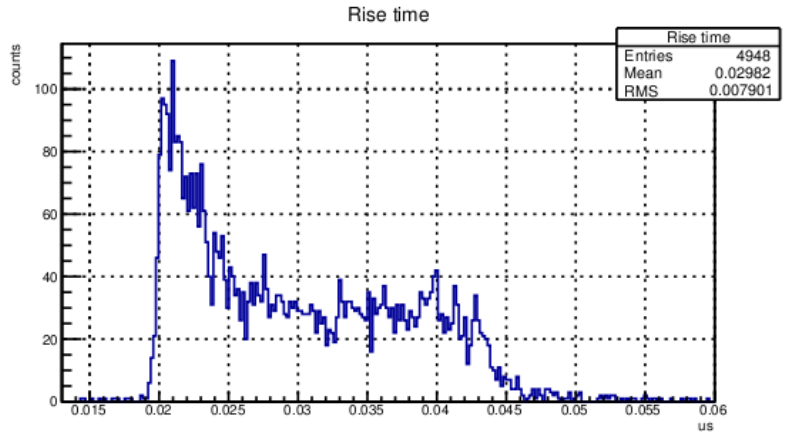

(a) Background

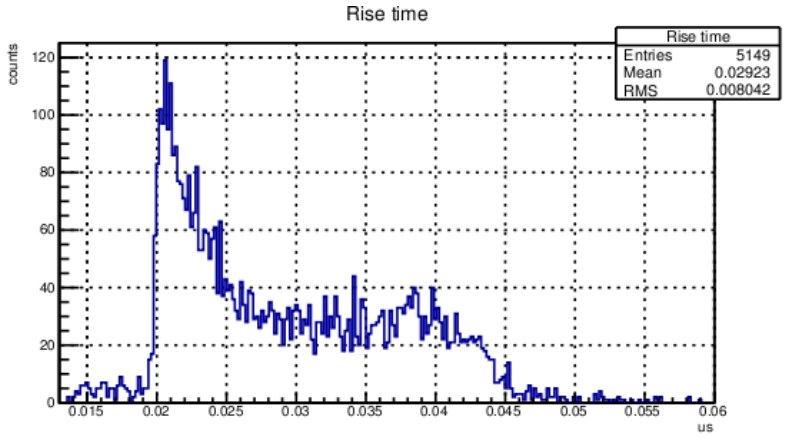

(b) *AmBe*+ Source plus Background

Figure 4.12: Rise time histogram for (a) the background measurement and (b) the Source plus Background measurement. The two peaks observed in both graphs correspond to two different types of sources, for this events. We can see that the neutron induced events are at rise times below $2\mu s$.

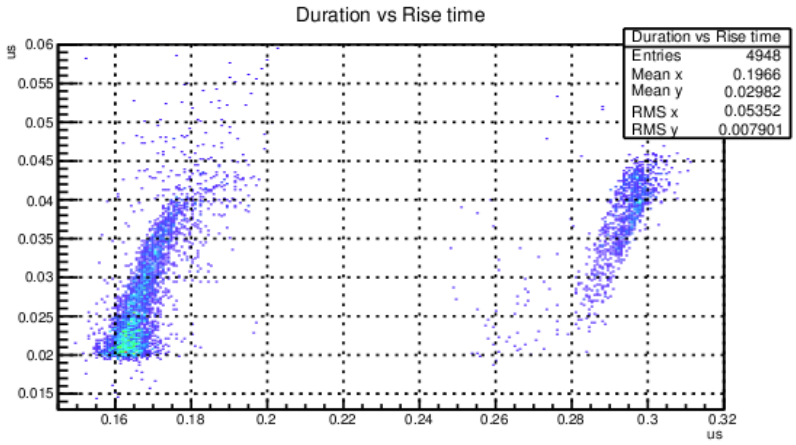

(a) Background

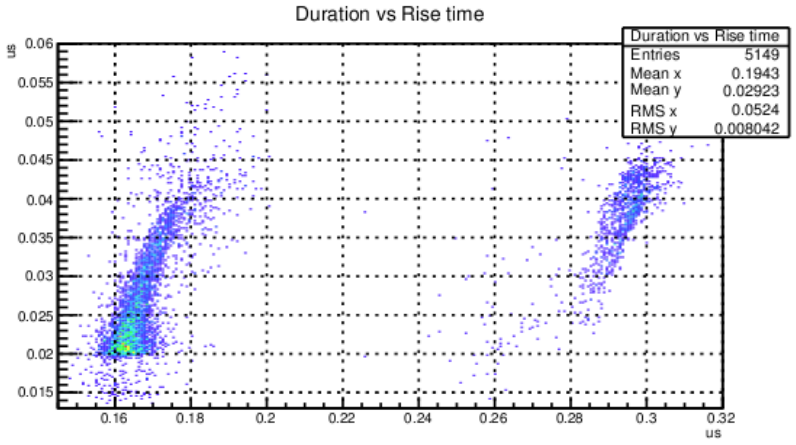

(b) $AmBe+$ Source plus Background

Figure 4.13: Pulse duration histogram for (a) the background measurement and (b) the Source plus Background measurement. The two clusters observed in both graphs correspond to two different types of sources, for this events. The first cluster are the interactions of the cosmic rays and the second cluster at the high duration area are the alpha wall effect.

Here we presented the $AmBe+$ Source plus Background measurement analysis after performing an $duration < 0.2\mu sec$ cut.

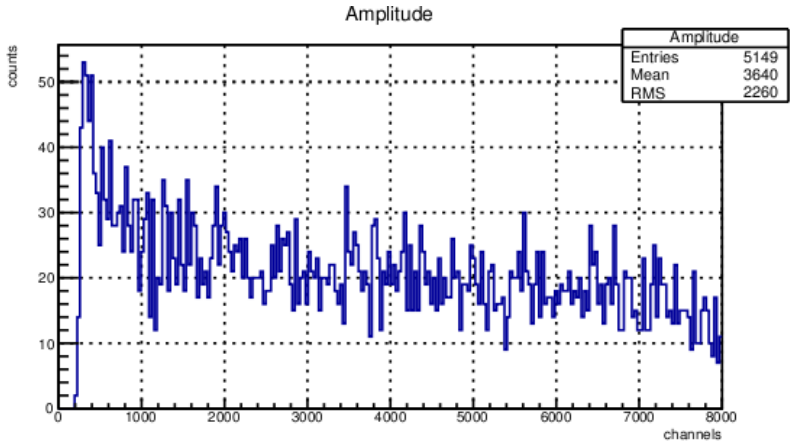

(a) No cuts

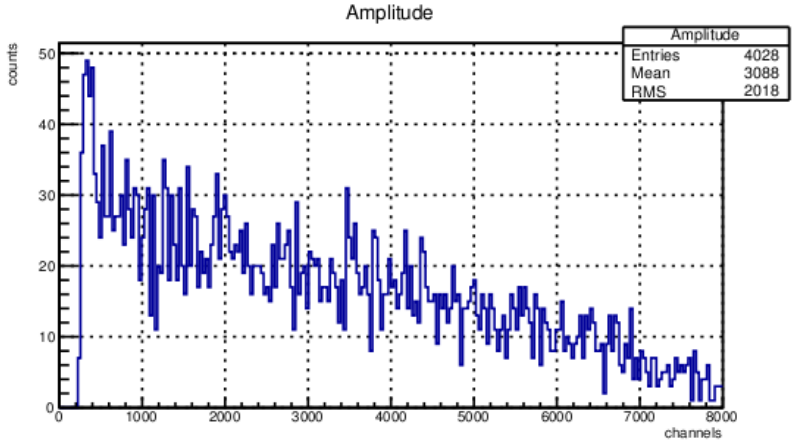

(b) Pulse duration cut

Figure 4.14: After the cut the alpha wall effect events, at high energy area, were removed from the spectrum

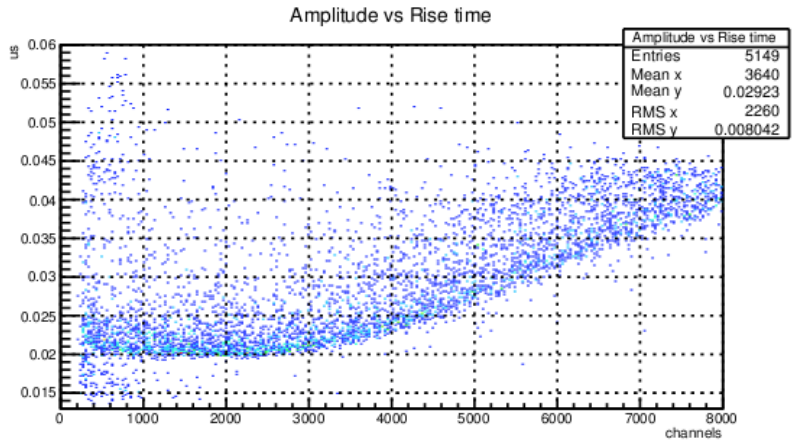

(a) No cuts

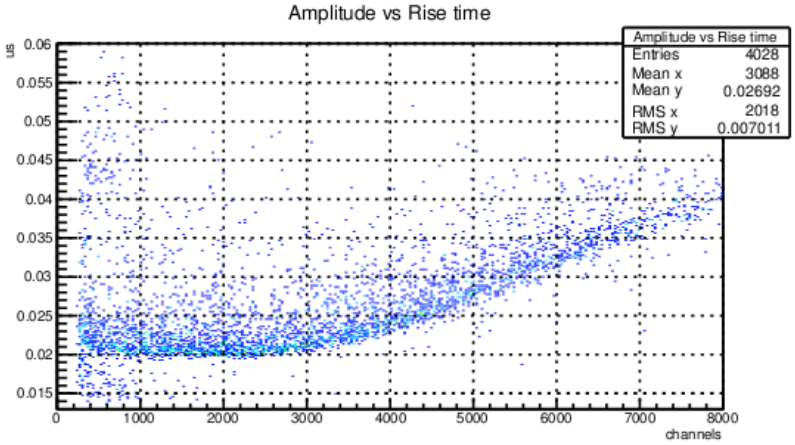

(b) Pulse duration cut

Figure 4.15: After the cut the alpha wall effect events, at high energy area, were removed from the amplitude vs rise plot

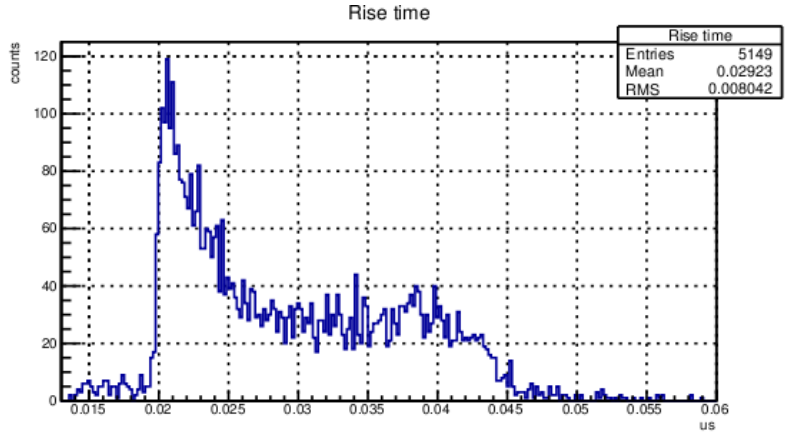

(a) No cuts

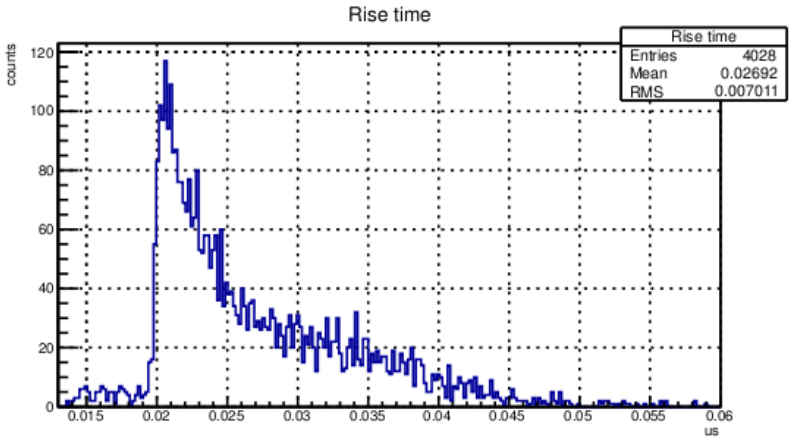

(b) Pulse duration cut

Figure 4.16: After the cut the second peak was removed, as expected (correlation between the rise time and the duration of the pulse).

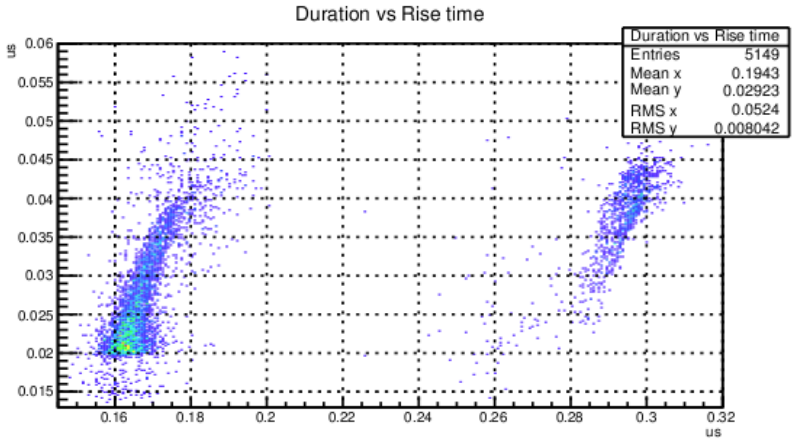

(a) No cuts

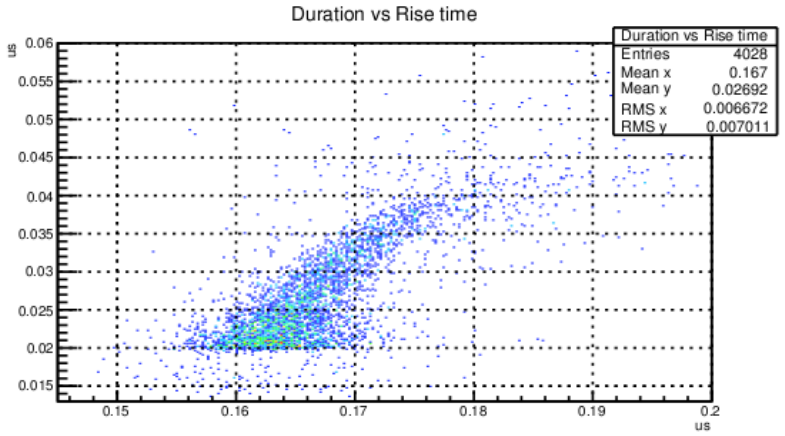

(b) Pulse duration cut

Figure 4.17: The duration of the pulse spectra after removing the second cluster.

Here the neutron induced events are discriminated from the rest, by performing a $0.013 < rise\ time < 0.019\ \mu s$ **and a** $duration < 0.2 \mu s$ **cuts.**

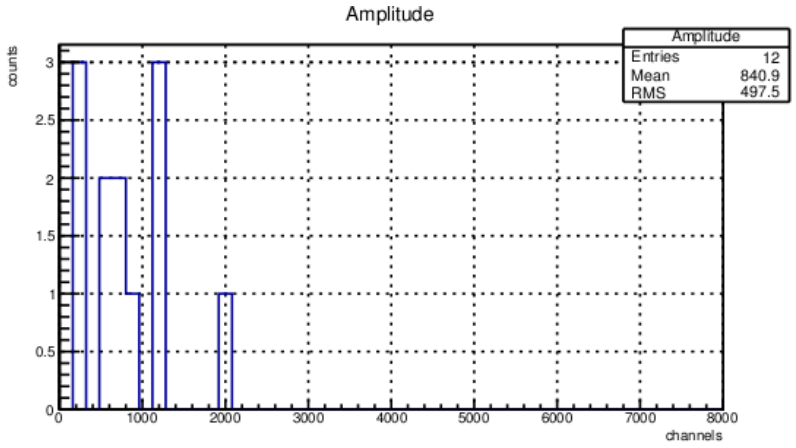

(a) Background

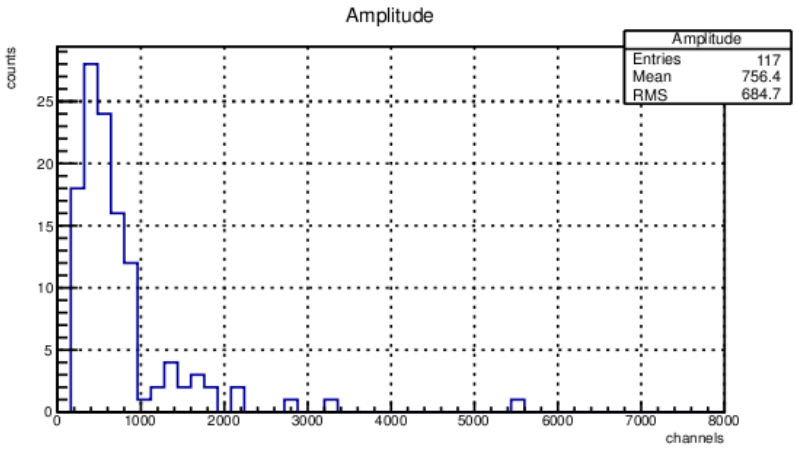

(b) *AmBe*+ Source plus Background

Figure 4.18: The amplitude spectra after performing a rise time cut. The neutron induced events are discriminated.

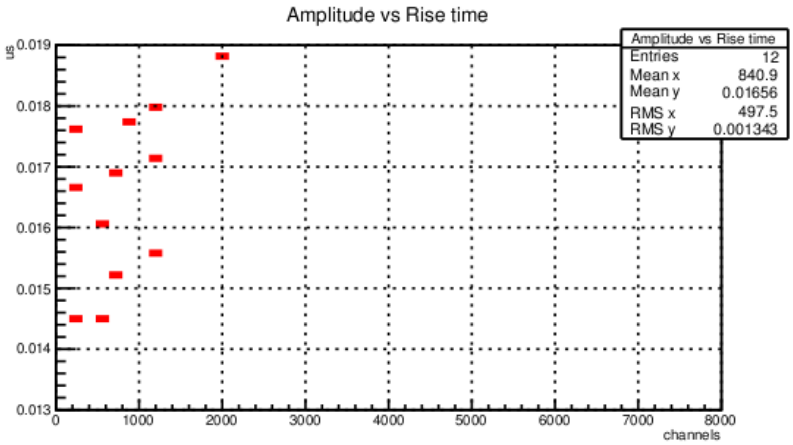

(a) Background

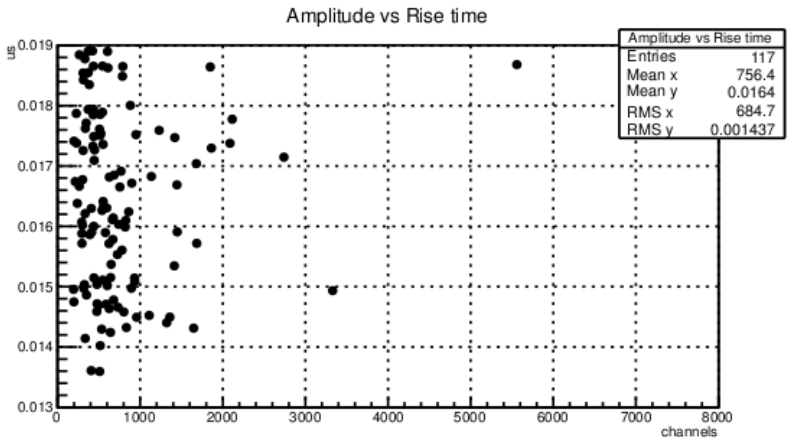

(b) $AmBe+$ Source plus Background

Figure 4.19: The amplitude vs rise time 2D histograms after performing a rise time cut. The neutron induced events are discriminated.

Appendix A

FLUKA input files

A.1 Neutrons transport

```
TITLE
SPC filled with Argon irradiated by an AmBe source of yield 6.6E4 n/sec
#if 0
OPEN                1.                                                      NEW

#endif
* We will need the EMF-CUT command to stop the transport at 100eV
DEFAULTS                                                                    CALORIME
RANDOMIZ            1.     11111.
*EMF
*EMFCUT         1.0E-07    1.0E-07         0.0         6.          7.         1.0
*PHYSICS             3.          3.          3.          3.                    NEUTRINO
*EMFFLUO             1.0     COPPER
*LOW-NEUT          260.         42.     0.0196         0.0
*PART-THR                   NEUTRON                                 0.0
*PART-THR      -1.0E-07    ELECTRON    ELECTRON          1.         0.0
*PART-THR      -1.0E-07     PHOTON      PHOTON          1.         0.0
*EMFRAY              1.          6.          7.         1.0
* ****************************************************************************
START             2.5E5                                                 0.0
* ****************************************************************************
* ****************************************************************************
*BEAM              -.0044         0.0    1896.86         0.0         0.0          1.PHOTON
BEAM              -.0158                                                        NEUTRON
BEAMPOS             0.0          0.0        -90.         0.0
SOURCE              2.
* ****************************************************************************
GEOBEGIN                                                                    COMBNAME
    0     0
SPH BlckBody    0.0 0.0 0.0 10000.0
SPH Vcum        0.0 0.0 0.0 5000.0
SPH ShellIn     0.0 0.0 0.0 64.4
SPH ShellOut    0.0 0.0 0.0 65.0
#if 0
RPP Polyeth     -15.0 +15.0 -15.0 +15.0 -73. -71.
#endif
#if 0
RPP Steel       -15.0 +15.0 -15.0 +15.0 -79. -74.
```

```
#endif
#if 0
RPP Lead        -15.0 15.0 -15.0 +15.0 -89. -80.
#endif
END
BLCKBODY     5 +BlckBody -Vcum
VACUUM       5 +Vcum -ShellOut
#if 0
STEEL1       5 +Steel
#endif
#if 0
PLAST1       5 +Polyeth
#endif
#if 0
LEAD         5 +Lead
#endif
CuShell      5 +ShellOut -ShellIn
Gas          5 +ShellIn
END
GEOEND
* ***************************************************************************
* ***************************************************************************
MATERIAL         29.     63.546       8.96        12.                    COPPER
MATERIAL         18.     39.9488.38819E-5         20.                    ARGON
MAT-PROP      0.0987                            ARGON
* 197 Methane C_H4
* Chemical Formula
*    of Methane              H
*                            |
*  C  H                   H — C — H
*       4                    |
*                            H
*MATERIAL                      1.76038E-5                                METHANE
*COMPOUND         4.0  HYDROGEN        1.0    CARBON                     METHANE
* Ar 95% -CH4 5%
*MATERIAL                      3.52075E-4                                GAS
*MAT-PROP         0.2                            GAS
*COMPOUND        -.95    -ARGON       -.05   -METHANE
* 221 Polyethylene, Marlex
* Density variation of polyethylene is 0.91 - 1.05 g/cm3. "Low" density is
*  0.920, "medium" is .93, and "high" is .95. Special polyethelene is made
* for nuclear shielding, and this has loaded densities up to 1.08.
* Chemical                   H    H
* Formula :                  |    |
*           |C H |       —— C — C ——
*           | 2 4|n         |    |
*                            H    H
MATERIAL                          .94                                    Polyethy
COMPOUND         4.0  HYDROGEN        2.0    CARBON                     Polyethy
MATERIAL         24.    51.9961       7.18                              CHROMIUM
* Stainless-Steel (typical)
* Stainless-Steel is produced with Cr content ranging from
* 4 - 19 Atomic Percent, and with C content from 0 - 4 percent.
MATERIAL                          8.0                                    Steel
COMPOUND        18.0  CHROMIUM      74.0      IRON        8.0     NICKELSteel
*MAT-PROP                         41.7    METHANE
ASSIGNMA    BLCKHOLE  BLCKBODY
*USRBDX          1.    NEUTRON      -29.         6.          7.          dbx_in
*USRBDX       0.0172        0.0                                          &
```

```
SCORE          ENERGY    NEUTRON
* ****************************************************************************
* Scoring
* ****************************************************************************
USRBIN           10.     ENERGY       -21.       100.       100.       100.EdepDet1
USRBIN         -100.       -100.      -100.       100.       100.       100.&
USRBIN           10.     NEUTRON       -22.       100.       100.       100.FluenDet1
USRBIN         -100.       -100.      -100.       100.       100.       100.&
USRBDX             1.    NEUTRON       -30.    CuShell       Gas            dbx_in
USRBDX                   1.0E-14                                             &
EVENTDAT       -23.                                                        data
*EVENTBIN      -12.0     ENERGY       -24.        Gas                       EnDepSpec1
*EVENTBIN                                                                  &
*USERDUMP        100.         40.         3.                               DUMP
*EVENTBIN      -12.0     ENERGY        26.         7.                       EnDepSpec2
*EVENTBIN                                                                  &
*EVENTBIN      -12.0     NEUTRON       -27.         7.                       FluenDet2
*EVENTBIN                                                                  &
*EVENTDAT        25.                                                       score
*USRBIN          12.     NEUTRON                    7.                       FluenDet3
*USRBIN          12.      E+&E-                     7.                       FluenDet2
*EVENTBIN      -12.0     NEUTRON        28.         7.                       FluenDet3
*EVENTBIN      -10.0     ENERGY                    80.        80.        80.EnDepSpec2
*EVENTBIN        -80.       -80.       -80.       200.       200.       200.&
*EVENTBIN      -10.0     ENERGY       -26.        80.        80.        80.EnDepSpec2a
*EVENTBIN        -80.       -80.       -80.       200.       200.       200.&
ASSIGNMA      VACUUM    VACUUM
ASSIGNMA      COPPER    CuShell
ASSIGNMA       ARGON       Gas
*ASSIGNMA    Polyethy    PLAST1
*ASSIGNMA       Steel    STEEL1
*ASSIGNMA        LEAD      LEAD
STOP
```

A.2 Photons transport

```
TITLE
SPC filled with Argon irradiated by an AmBe source of yield 6.6E4 n/sec
#if 0
OPEN                1.                                                  NEW

#endif
* We will need the EMF-CUT command to stop the transport at 100eV
DEFAULTS                                                            CALORIME
RANDOMIZ            1.     11111.
*EMF
EMFCUT         1.0E-06    1.0E-06        0.0    CuShell        Gas         1.0
*PHYSICS             3.          3.          3.          3.                    NEUTRINO
EMFFLUO             1.0     COPPER
*LOW-NEUT          260.
PART-THR        -1.E-6  ELECTRON                    1.         0.0
PART-THR        -1.E-6    PHOTON                    1.         0.0
EMFFRAY             1.    CuShell        Gas         1.0
* ***************************************************************************
START            2.5E4                                          0.0
* ***************************************************************************
* ***************************************************************************
BEAM            -.0044         0.0      1251.0         0.0         0.0          1.PHOTON
*BEAM           -0.0172                                                        NEUTRON
BEAMPOS            0.0         0.0        -90.         0.0
*SOURCE             2.
* ***************************************************************************
GEOBEGIN                                                                  COMBNAME
    0     0
SPH BlckBody    0.0 0.0 0.0 10000.0
SPH Vcum        0.0 0.0 0.0 5000.0
SPH ShellIn     0.0 0.0 0.0 64.4
SPH ShellOut    0.0 0.0 0.0 65.0
#if 0
RPP Polyeth     -15.0 +15.0 -15.0 +15.0 -73. -71.
#endif
#if 0
RPP Steel       -15.0 +15.0 -15.0 +15.0 -79. -74.
#endif
RPP Lead        -15.0 15.0 -15.0 +15.0 -89. -80.
END
BLCKBODY      5 +BlckBody -Vcum
VACUUM        5 +Vcum -ShellOut
#if 0
STEEL1        5 +Steel
#endif
#if 0
PLAST1        5 +Polyeth
#endif
#if 0
LEAD          5 +Lead
#endif
CuShell       5 +ShellOut -ShellIn
Gas           5 +ShellIn
END
GEOEND
* ***************************************************************************
* ***************************************************************************
```

```
MATERIAL          29.     63.546       8.96        12.                    COPPER
MATERIAL          18.     39.9488.38819E-5         20.                    ARGON
MAT-PROP       0.0987                             ARGON
* 197 Methane C_H4
* Chemical Formula
*    of Methane                H
*                              |
*  C   H                  H --- C --- H
*       4                      |
*                              H
*MATERIAL                        1.76038E-5                              METHANE
*COMPOUND          4.0  HYDROGEN        1.0   CARBON                     METHANE
* Ar 95% -CH4 5%
*MATERIAL                        3.52075E-4                              GAS
*MAT-PROP          0.2                          GAS
*COMPOUND         -.95   -ARGON        -.05  -METHANE
* 221 Polyethylene, Marlex
* Density variation of polyethylene is 0.91 - 1.05 g/cm3. "Low" density is
*  0.920, "medium" is .93, and "high" is .95. Special polyethelene is made
* for nuclear shielding, and this has loaded densities up to 1.08.
* Chemical                      H    H
* Formula :                     |    |
*           |C H |         ---- C -- C ----
*           | 2 4|n           |    |
*                              H    H
MATERIAL                           .94                                   Polyethy
COMPOUND          4.0  HYDROGEN        2.0   CARBON                     Polyethy
MATERIAL          24.    51.9961       7.18                             CHROMIUM
* Stainless-Steel (typical)
* Stainless-Steel is produced with Cr content ranging from
* 4 - 19 Atomic Percent, and with C content from 0 - 4 percent.
MATERIAL                           8.0                                   Steel
COMPOUND         18.0  CHROMIUM      74.0     IRON        8.0    NICKELSteel
*MAT-PROP                          41.7   METHANE
ASSIGNMA    BLCKHOLE  BLCKBODY
*USRBDX            1.    NEUTRON      -29.   CuShell       Gas          dbx_in
*USRBDX       0.0172        0.0                                         &
* ****************************************************************************
* Scoring
* ****************************************************************************
SCORE          ENERGY    PHOTON
USRBIN            10.    ENERGY       -21.       100.       100.       100.EdepDet1
USRBIN          -100.     -100.       -100.       100.       100.       100.&
USRBIN            10.    PHOTON       -22.       100.       100.       100.FluenDet1
USRBIN          -100.     -100.       -100.       100.       100.       100.&
*EVENTBIN       -12.0    ENERGY       -24.        Gas                    EnDepSpec1
*EVENTBIN                                                               &
*EVENTBIN       -12.0  EM-ENRGY        26.        Gas                    EnDepSpec2
*EVENTBIN                                                               &
*USRBDX            1.    PHOTON       -30.        Gas   CuShell          dbx_out
*USRBDX       0.0045        0.0        50.                               &
USRBDX             1.    PHOTON       -31.    CuShell       Gas          dbx_in
USRBDX        0.0045        0.0        50.                               &
*USERDUMP        100.        40.         3.                               dump
*EVENTBIN       -12.0    NEUTRON       -27.        Gas                    FluenDet2
*EVENTBIN                                                               &
EVENTDAT        -25.                                                    evdata
*USRBIN           12.    NEUTRON                   Gas                    FluenDet3
*USRBIN           12.      E+&E-                   Gas                    FluenDet2
```

```
*EVENTBIN      -12.0  NEUTRON    28.      Gas                    FluenDet3
*EVENTBIN      -10.0  ENERGY              80.      80.      80.EnDepSpec2
*EVENTBIN      -80.   -80.    -80.      200.     200.     200.&
*EVENTBIN      -10.0  ENERGY    -26.      80.      80.      80.EnDepSpec2a
*EVENTBIN      -80.   -80.    -80.      200.     200.     200.&
ASSIGNMA  VACUUM  VACUUM
ASSIGNMA  COPPER  CuShell
ASSIGNMA  ARGON   Gas
*ASSIGNMA  Polyethy  PLAST1
*ASSIGNMA  Steel     STEEL1
*ASSIGNMA  LEAD      LEAD
STOP
```

A.3 Modified source.f user routine

```
*$ CREATE SOURCE.FOR
*COPY SOURCE
*
*=== source ============================================================*
*
      SUBROUTINE SOURCE ( NOMORE )

      INCLUDE '(DBLPRC)'
      INCLUDE '(DIMPAR)'
      INCLUDE '(IOUNIT)'
*
      INCLUDE '(BEAMCM)'
      INCLUDE '(FHEAVY)'
      INCLUDE '(FLKSTK)'
      INCLUDE '(IOIOCM)'
      INCLUDE '(LTCLCM)'
      INCLUDE '(PAPROP)'
      INCLUDE '(SOURCM)'
      INCLUDE '(SUMCOU)'
*

      LOGICAL LFIRST
*
      PARAMETER (NCF = 33, NAMBE = 22)
      DIMENSION CF(0:NCF), AMBE(0:NAMBE), ENERCF(0:NCF), ENERAM(0:NAMBE)
      DIMENSION CUMUCF(0:NCF), CUMUAM(0:NAMBE)
      SAVE LFIRST
      DATA LFIRST / .TRUE. /
      DATA ENERCF / 4.64d-6,
     & 1.00d-5, 1.25d-5, 1.58d-5, 1.99d-5, 2.51d-5, 3.16d-5,
     & 3.98d-5, 5.01d-5, 6.30d-5, 7.94d-5, 1.00d-4, 1.25d-4, 1.58d-4,
     & 1.99d-4, 2.51d-4, 3.16d-4, 3.98d-4, 5.01d-4, 6.30d-4, 7.94d-4,
     & 1.00d-3, 1.25d-3, 1.58d-3, 1.99d-3, 2.51d-3, 3.16d-3, 3.98d-3,
     & 5.01d-3, 6.30d-3, 7.94d-3, 1.00d-2, 1.58d-2, 2.00d-2 /
      DATA ENERAM / 7.94d-5, 1.00d-4, 1.25d-4, 1.58d-4,
     & 1.99d-4, 2.51d-4, 3.16d-4, 3.98d-4, 5.01d-4, 6.30d-4, 7.94d-4,
     & 1.00d-3, 1.25d-3, 1.58d-3, 1.99d-3, 2.51d-3, 3.16d-3, 3.98d-3,
     & 5.01d-3, 6.30d-3, 7.94d-3, 1.00d-2, 1.58d-2 /
* spectra are in n/cm2 per unit lethargy!
      DATA CF / 0.d0,
     & 9.22d-4, 1.29d-3, 1.79d-3, 2.48d-3, 3.39d-3, 4.64d-3,
     & 6.38d-3, 8.81d-3, 1.21d-2, 1.69d-2, 2.37d-2, 3.26d-2, 4.45d-2,
     & 6.05d-2, 8.22d-2, 1.09d-1, 1.45d-1, 1.89d-1, 2.41d-1, 3.00d-1,
     & 3.59d-1, 4.14d-1, 4.52d-1, 4.62d-1, 4.34d-1, 3.66d-1, 2.71d-1,
     & 1.69d-1, 8.61d-2, 3.35d-2, 4.27d-3, 4.31d-4, 0.d0 /
      DATA AMBE / 0.d0,
     &   1.66d-2, 2.21d-2, 2.87d-2, 3.67d-2, 4.65d-2, 5.77d-2,
     &   7.06d-2, 8.48d-2, 9.61d-2, 1.06d-1, 1.18d-1, 1.27d-1, 1.81d-1,
     &   2.43d-1, 4.21d-1, 5.71d-1, 6.86d-1, 6.50d-1, 5.78d-1, 1.66d-1,
     &   1.72d-2, 0.d0 /
      NOMORE = 0
*  +-------------------------------------------------------------------*
*      COUNTER=1
*  +-------------------------------------------------------------------*
*  |  First call initializations:
      IF ( LFIRST ) THEN
*  |  *** The following 3 cards are mandatory ***
```

```
      TKESUM = ZERZER
      LFIRST = .FALSE.
      LUSSRC = .TRUE.
*  |  *** User initialization ***
      WRITE(LUNOUT,*)
      WRITE(LUNOUT,'(A,132A)') ("*",I=1,132)
      WRITE(LUNOUT,*)
      WRITE(LUNOUT,*)
      IF(NINT(WHASOU(1)) .EQ. 1) THEN
         WRITE(LUNOUT,'(A)') "@ Source: Cf-252"
      ELSE IF(NINT(WHASOU(1)) .EQ. 2) THEN
         WRITE(LUNOUT,'(A)') "@ Source: Am-Be"
      ELSE
         STOP "Incorrect WHASOU(1)"
      END IF
      WRITE(LUNOUT,*)
      WRITE(LUNOUT,*)
      WRITE(LUNOUT,'(A,132A)') ("*",I=1,132)
      WRITE(LUNOUT,*)
      if(nint(whasou(1)) .eq. 1) then
*        Transform energies to lethargies
         do i = 0, ncf
            enercf(i) = log(enercf(i))
         end do
         cumucf(0) = 0.d0
*        prepare the cumulative function
         do i = 1, ncf
            cumucf(i) = cumucf(i-1) +
     &                  (cf(i-1)+cf(i))*(enercf(i)-enercf(i-1))*0.5d0
         end do
*           WRITE(88,*) "Lethargies, Cumulative, non normalized"
*           DO I = 0, NCF
*              WRITE(88,'(I3,1X,1P,2G15.9)') I, ENERCF(I), CUMUCF(I)
*           END DO
*        normalize the cumulative function
         cunorm = cumucf(ncf)
         do i = 1, ncf
            cumucf(i) = cumucf(i)/cunorm
         end do
*           WRITE(88,*) "Lethargies, Cumulative, normalized"
*           DO I = 0, NCF
*              WRITE(88,'(I3,1X,1P,2G15.9)') I, ENERCF(I), CUMUCF(I)
*           END DO
      else if(nint(whasou(1)) .eq. 2) then
*        Transform energies to lethargies
         do i = 0, nambe
            eneram(i) = log(eneram(i))
         end do
         cumuam(0) = 0.d0
*        prepare the cumulative function
         do i = 1, nambe
          cumuam(i) = cumuam(i-1) +
     &                (ambe(i-1)+ambe(i))*(eneram(i)-eneram(i-1))*0.5d0
         end do
*        normalize the cumulative function
         cunorm = cumuam(nambe)
         do i = 1, nambe
            cumuam(i) = cumuam(i)/cunorm
         end do
```

```
            end if
*           kount = 0
*         WRITE(88,*)
*        & "Sampled: xi, cum(i-1), cum(i), leth(i-1), leth(i), leth, energy"
         END IF
*  |
*  +-------------------------------------------------------------------*
*  Push one source particle to the stack. Note that you could as well
*  push many but this way we reserve a maximum amount of space in the
*  stack for the secondaries to be generated
* Npflka is the stack counter: of course any time source is called it
* must be =0
*         kount = kount + 1
*         if(kount .gt. 100) nomore = 1
         NPFLKA = NPFLKA + 1
* Wt is the weight of the particle
         WTFLK  (NPFLKA) = ONEONE
         WEIPRI = WEIPRI + WTFLK (NPFLKA)
* Particle type (1=proton.....). Ijbeam is the type set by the BEAM
* card
*  +-------------------------------------------------------------------*
*  |  (Radioactive) isotope:
         IF ( IJBEAM .EQ. -2 .AND. LRDBEA ) THEN
            IARES  = IPROA
            IZRES  = IPROZ
            IISRES = IPROM
            CALL STISBM ( IARES, IZRES, IISRES )
            IJHION = IPROZ  * 1000 + IPROA
            IJHION = IJHION * 100 + KXHEAV
            IONID  = IJHION
            CALL DCDION ( IONID )
            CALL SETION ( IONID )
*  |
*  +-------------------------------------------------------------------*
*  |  Heavy ion:
         ELSE IF ( IJBEAM .EQ. -2 ) THEN
            IJHION = IPROZ  * 1000 + IPROA
            IJHION = IJHION * 100 + KXHEAV
            IONID  = IJHION
            CALL DCDION ( IONID )
            CALL SETION ( IONID )
            ILOFLK (NPFLKA) = IJHION
*  |  Flag this is prompt radiation
            LRADDC (NPFLKA) = .FALSE.
*  |
*  +-------------------------------------------------------------------*
*  |  Normal hadron:
         ELSE
            IONID = IJBEAM
            ILOFLK (NPFLKA) = IJBEAM
*  |  Flag this is prompt radiation
            LRADDC (NPFLKA) = .FALSE.
         END IF
*  |
*  +-------------------------------------------------------------------*
* From this point .....
* Particle generation (1 for primaries)
         LOFLK  (NPFLKA) = 1
* User dependent flag:
```

```
      LOUSE  (NPFLKA) = 0
*  User dependent spare variables:
      DO 100 ISPR = 1, MKBMX1
         SPAREK (ISPR,NPFLKA) = ZERZER
 100  CONTINUE
*  User dependent spare flags:
      DO 200 ISPR = 1, MKBMX2
         ISPARK (ISPR,NPFLKA) = 0
 200  CONTINUE
*  Save the track number of the stack particle:
      ISPARK (MKBMX2,NPFLKA) = NPFLKA
      NPARMA = NPARMA + 1
      NUMPAR (NPFLKA) = NPARMA
      NEVENT (NPFLKA) = 0
      DFNEAR (NPFLKA) = +ZERZER
*  ... to this point: don't change anything
*  Particle age (s)
      AGESTK (NPFLKA) = +ZERZER
      AKNSHR (NPFLKA) = -TWOTWO
*  Group number for "low" energy neutrons, set to 0 anyway
      IGROUP (NPFLKA) = 0
*  Kinetic energy of the particle (GeV). Sample from the cumulative
       xi = flrndm(dummy)
       if(nint(whasou(1)) .eq. 1) then
          do i = 1, ncf
             if(xi .gt. cumucf(i-1) .and. xi .le. cumucf(i)) then
                enkin = enercf(i-1)+(enercf(i)-enercf(i-1))*
     &          (sqrt(xi) - sqrt(cumucf(i-1)))/
     &                                (sqrt(cumucf(i))-sqrt(cumucf(i-1)))
*               WRITE(88,'(3G12.4,1P,4G12.4)')
*     & XI,CUMUCF(I-1),CUMUCF(I),ENERCF(I-1),ENERCF(I),ENKIN,EXP(ENKIN)
                go to 1
             end if
          end do
       else if(nint(whasou(1)) .eq. 2) then
          do i = 1, nambe
             if(xi .gt. cumuam(i-1) .and. xi .le. cumuam(i)) then
                enkin = eneram(i-1)+(eneram(i)-eneram(i-1))*
     &          (sqrt(xi) - sqrt(cumuam(i-1)))/
     &                                (sqrt(cumuam(i))-sqrt(cumuam(i-1)))
                go to 1
             end if
          end do
       end if
 1     continue
*      back from lethargy to energy
       tkeflk (npflka) = exp(enkin)
*      TKEFLK (NPFLKA) = SQRT ( PBEAM**2 + AM (IONID)**2 ) - AM (IONID)
*  Particle momentum
*      PMOFLK (NPFLKA) = PBEAM
       PMOFLK (NPFLKA) = SQRT ( TKEFLK (NPFLKA) * ( TKEFLK (NPFLKA)
     &                          + TWOTWO * AM (IONID) ) )
*|----------------------------------------------------------------------|*
*|----------------------------------------------------------------------|*
*|----------------------------------------------------------------------|*
*|----------------------------------------------------------------------|*
       CALL SFECFE(SINF,COSF)
       PI=4.D0*DATAN(1.D0)
```

```
      COST=COS(PI*0.2*FLRNDM(DUMM))
      SINT=SQRT((ONEONE-COST)*(ONEONE+COST))

*       WRITE(LUNOUT,*)"------------ANGLES-------------------------------"
*       WRITE(LUNOUT,*) "sin(THETA)=",SINT," ","cos(PHI)=",COSF

      TXFLK  (NPFLKA) = SINT*COSF
      TYFLK  (NPFLKA) = SINT*SINF
      TZFLK  (NPFLKA) = SQRT(ONEONE-TXFLK(NPFLKA)**2 -TYFLK(NPFLKA)**2)
*       WRITE(LUNOUT,*)"------------POSITIONS-----------------------------"
*       WRITE(LUNOUT,*) "TX=",TXFLK
*       TXFLK  (NPFLKA) = UBEAM
*       TYFLK  (NPFLKA) = VBEAM
*       TZFLK  (NPFLKA) = WBEAM
*|-----------------------------------------------------------------------|*
*|-----------------------------------------------------------------------|*
* Polarization cosines:
      TXPOL  (NPFLKA) = -TWOTWO
      TYPOL  (NPFLKA) = +ZERZER
      TZPOL  (NPFLKA) = +ZERZER
* Particle coordinates
      XFLK   (NPFLKA) = XBEAM
      YFLK   (NPFLKA) = YBEAM
      ZFLK   (NPFLKA) = ZBEAM
*       WRITE(LUNOUT,*) "Z", ZFLK
*|-----------------------------------------------------------------------|*
*|-----------------------------------------------------------------------|*
*  Calculate the total kinetic energy of the primaries: don't change
      IF ( ILOFLK (NPFLKA) .EQ. -2 .OR. ILOFLK (NPFLKA) .GT. 100000 )
     &   THEN
         TKESUM = TKESUM + TKEFLK (NPFLKA) * WTFLK (NPFLKA)
      ELSE IF ( ILOFLK (NPFLKA) .NE. 0 ) THEN
         TKESUM = TKESUM + ( TKEFLK (NPFLKA) + AMDISC (ILOFLK(NPFLKA)) )
     &            * WTFLK (NPFLKA)
      ELSE
         TKESUM = TKESUM + TKEFLK (NPFLKA) * WTFLK (NPFLKA)
      END IF
      RADDLY (NPFLKA) = ZERZER
*  Here we ask for the region number of the hitting point.
*     NREG (NPFLKA) = ...
*  The following line makes the starting region search much more
*  robust if particles are starting very close to a boundary:
      CALL GEOCRS ( TXFLK (NPFLKA), TYFLK (NPFLKA), TZFLK (NPFLKA) )
      CALL GEOREG ( XFLK  (NPFLKA), YFLK  (NPFLKA), ZFLK  (NPFLKA),
     &              NRGFLK(NPFLKA), IDISC )
*  Do not change these cards:
      CALL GEOHSM ( NHSPNT (NPFLKA), 1, -11, MLATTC )
      NLATTC (NPFLKA) = MLATTC
      CMPATH (NPFLKA) = ZERZER
      CALL SOEVSV
      RETURN
*=== End of subroutine Source =========================================*
      END
```

A.4 Files for reading the EVENTDAT unformatted output

```
      PROGRAM RDEVDT

      CHARACTER*80 RUNTIT, FILNAM
      CHARACTER*32 RUNTIM
      DIMENSION ISCORE(4), ENDIST(12), REGSCO(5000,4)
*-----------------------------------------------------------------------
*     User valiables of interest
*-----------------------------------------------------------------------
      ENDEPTOT=DBLE(0)
      COUNTER=DBLE(0.0)


      OPEN(UNIT = 8, FORM = 'FORMATTED', FILE = 'Data.txt',
     &     STATUS = 'NEW')

      CALL treeinit();
*
      iev = 0
      call histini(iev)
*-----------------------------------------------------------------------
*     Loop on each file (reading multiple files)
*-----------------------------------------------------------------------
1000  CONTINUE
      WRITE(*,*) 'Name of the EVENTDAT binary file?'
      READ(*,'(A)') FILNAM
      IF (FILNAM .EQ. ' ') GO TO 2000

      IB = INDEX(FILNAM, ' ')
      OPEN(UNIT = 7, FORM = 'UNFORMATTED', FILE = FILNAM(1:IB-1),
     &     STATUS = 'OLD')
*-----------------------------------------------------------------------
*     Once, at the beginning of the run:
*-----------------------------------------------------------------------
      READ(7)  RUNTIT, RUNTIM, NREGS, NSCO, (ISCORE(IS), IS = 1, NSCO)
C      WRITE(8,'(A80)') RUNTIT
C      WRITE(8,'(A32)') RUNTIM
C      WRITE(8,'(A,I6,5X,A,I4)') 'Number of regions: ', NREGS,
C     &           ' Number of scored quantities: ', NSCO
C      WRITE(8,'(A,4I6)') 'The scored quantities are: ',
C     &           (ISCORE(IS), IS = 1, NSCO)
*-----------------------------------------------------------------------
*     Loop on each primary particle:
*-----------------------------------------------------------------------
 100  CONTINUE
c      WRITE(8,*)
      READ(7,END=300) NCASE, WEIPRU, ENETOT
c      WRITE(8,'(A,I10,1P,2G12.4)') 'NCASE, WEIPRU, ENETOT: ',
c     &                 NCASE, WEIPRU, ENETOT
      READ(7) (ENDIST(IE), IE = 1, 12)
c      WRITE(8,'(A)') 'ENDIST: '
*
c      DO 400 IE = 1, 12, 2
c      WRITE(8,'(2(I5,5X,1P,G12.4))') IE,ENDIST(IE),IE+1,ENDIST(IE+1)
c 400  CONTINUE
```

```
*
      DO 200 ISC = 1, NSCO
      READ(7) IISC, ISCORE(ISC)
*     IISC is redundant, must be equal to ISC
      IF(IISC .NE. ISC) STOP 'Wrong sequence'
c      WRITE(8,'(A,I2,A,I3,A)')
c     &     'Quantity n. ',ISC, ' (',ISCORE(ISC),'):'
*
      READ(7) (REGSCO(IR,ISC), IR = 1, NREGS)
c      WRITE(8,*) 'Scoring per region:'
      DO 500 IR = 1, NREGS
*-----------------------------------------------------------------------
* define area of interest and distribution of interest
*-----------------------------------------------------------------------

      IF((IR.EQ.4).AND.(ISC.EQ.1))THEN
        IF(REGSCO(IR,ISC).GT.0.0)THEN
c      WRITE(8,*) 'Scoring per region:'
c      WRITE(8,'(I10, X, 2G12.4, X, I7, 1P, G12.4)')
c     &     NCASE, ENETOT, IR, REGSCO(IR,ISC)
C        WRITE(8,'(I,G)') NCASE, REGSCO(IR,ISC)
c       WRITE(8,'(I10,1P,2G12.4,I7,3X,1P,G12.4)') NCASE, WEIPRU, ENETOT, IR, REGSCO(IR,ISC)
!       WRITE(8,'(I10,1P,G12.4)') IR, REGSCO(IR,ISC)
        WRITE(8,*) REGSCO(IR,ISC)
        ENDEPTOT= ENDEPTOT+ DBLE(REGSCO(IR,ISC))
        COUNTER=COUNTER+1.0
        CALL treefill(DBLE(REGSCO(IR,ISC))*DBLE(1.0E+6))
        !CALL treefill()
        END IF
      END IF
*
 500  CONTINUE
 200  CONTINUE
*
      READ(7) NDUM, DUM1, DUM2
      IF (DUM1 .LT. 0.) THEN
*     DUM1 < 0 is used to signal that seeds follow
      READ(7) ISEED1, ISEED2, SEED1, SEED2, SOPP1, SOPP2
c      WRITE(8,*) ISEED1, ISEED2, SEED1, SEED2, SOPP1, SOPP2
      ELSE
      BACKSPACE 7
      END IF
*-----------------------------------------------------------------------
*     This event is finished, start again with the next one
*-----------------------------------------------------------------------
      GO TO 100
*
 300  CONTINUE
c      WRITE(8,*) "End of a run of ", NCASE, " particles"
      CLOSE (UNIT = 7)
      GOTO 1000
2000  CONTINUE
*      CLOSE (UNIT = 8)
      CALL fileclose()
      WRITE(*,*) 'ENDEPTOT',ENDEPTOT/DBLE(2.5E+5)
      WRITE(*,*) 'COUNTER',COUNTER/DBLE(2.5E+5)

      STOP
      END
```

```
// Giannis version


#ifndef __CFORTRAN_LOADED
#include "cfortran.h"
#endif

using namespace std;

#include <stdio.h>
#include <stdlib.h>
#include "iostream"
#include <ctime>
#include <TROOT.h>
#include <TTree.h>
#include <TFile.h>
#include <TH1D.h>
#include <time.h>

#ifndef WIN32
#define treeinit treeinit_
#else
#define treeinit TREEINIT
#endif

static TFile *RootFile = 0;

TH1D *RootHist1;

extern "C" {
  void treeinit ()
  {
    printf("Executing TREEINIT\n");
    RootFile = new TFile("mutel.root","recreate");
  }
}

#ifndef WIN32
#define histini histini_
#else
#define histini HISTINI
#endif

extern "C" {
  void histini (Int_t &ih)
  {
        printf("Executing RootHist\n");
         RootHist1 = new TH1D("sc1","Scint1",30,0.0400334734,2377.64232);
  }
}

#ifndef WIN32
#define treefill treefill_
#else
#define treefill TREEFILL
#endif
extern "C" {
  void treefill(Double_t &edep1/*, Double_t &edep2, Double_t &edep3  */)
  {
```

```
                //cout<<"edep = "<<edep1<<endl;

                RootHist1->Fill( edep1 );

  }
}

#ifndef WIN32
#define fileclose fileclose_
#else
#define fileclose FILECLOSE
#endif

extern "C" {
  void fileclose()
  {
    RootHist1->Write();

    printf("Closing \n");
    RootFile->Close();
  }
}

# Makefile for the ROOT test programs.
# This Makefile shows nicely how to compile and link applications
# using the ROOT libraries on all supported platforms.
# Giannis version


ARCH          = linux
CXX           =
ObjSuf        = o
SrcSuf        = cpp
ExeSuf        =
DllSuf        = so
OutPutOpt     = -o
SrcFor        = f

ROOTCFLAGS   := $(shell root-config --cflags)
ROOTLIBS     := $(shell root-config --libs)
ROOTGLIBS    := $(shell root-config --glibs)
FLUKALIB      = $(FLUPRO)/libflukahp.a

# Linux with egcs, gcc 2.9x, gcc 3.x (>= RedHat 5.2)
CXX           = g++
CXXFLAGS      = -O -Wall -fPIC
LD            = g++
LDFLAGS       = -O
SOFLAGS       = -shared
G77           = g77
FFLAGS        = -O3 -g -mcpu=pentiumpro -fexpensive-optimizations -funroll-loops -fstrength-reduce -malign-double -W -f
CXXFLAGS     += $(ROOTCFLAGS)
LIBS          = $(ROOTLIBS) $(SYSLIBS)
GLIBS         = $(ROOTGLIBS) $(SYSLIBS)

#------------------------------------------------------------------------------

readdat:    readdat.o HistLib.o
            @echo "Generating Object $@..."
```

```
            g77 readdat.o HistLib.o $(FLUKALIB) $(ROOTLIBS) -o readdat

readdat.o:   readdat.f
            @echo "Generating Object $@..."
            g77 -c readdat.f $(FFLAGS)

HistLib.o:  HistLib.cpp
            @echo "Generating Library $@..."
            g++ -c HistLib.cpp $(ROOTCFLAGS)

clean:
            @rm -f readdat readdat.o HistLib.o core.*

.$(SrcSuf).$(ObjSuf):
        $(CXX) $(CXXFLAGS) -c $<
```

Bibliography

[1] *E. Bougamont et al*, arXiv:1010.4132v1, 2010

[2] *J.Derre*, Pulse shape in the SPC prototype, October 4, 2007

[3] *S. Aune et al*, J. Phys.: Conf. Ser. 39 281, 2006

[4] *S Andriamonje et al*, J. Phys.: Conf. Ser. 179 012003, 2009

[5] *I Giomataris et al*, 2008 JINST 3 P09007

[6] *Andrew Durocher*, Understanding of the Proportional Counter Pulse Shape, RARAF

[7] *I. Giomataris*, The spherical detector, Glascow, 2008.

[8] *I. Savvidis*, Underground Low Flux Neutron Background Measurements in LSM Using A Large Volume (1 m^3) Spherical Proportional Counter,Rome, 2009

[9] *G. Gerbier*, Spherical Proportional Counter for low neutron flux measurements @ Laboratoire Souterrain de Modane,2010 TPC workhop,Paris, Dec 16th 2010

[10] *I. Giomataris et al*, arXiv:hep-ex/0502033v1,(2005)

[11] *Y. Giomataris, J.D. Vergados*, arXiv:hep-ex/0503029v2,(2006)

[12] *S. Aune et al*,AIP Conf. Proc. 785, pp. 110-118, 2004

[13] *J.D. Vergados, Y. Giomataris*, Phys.Atom.Nucl.70:140-149,2007

[14] *Carlos Martinez Amaya, Matteo Biassoni*, arXiv:1110.3536v2, 2011

[15] *J.D. Vergados, Y. Giomataris*, PHYSICS OF ATOMIC NUCLEI,Volume 67, Number 6, 1097-1106

[16] *G. J. Gounaris, E. A. Paschos, and P. I. Porfyriadis* , Phys. Rev. D 70, 113008 (2004)

[17] *J. D. Vergados, F. T. Avignone, III, I. Giomataris*, Phys. Rev. D 79, 113001 (2009)

[18] *Philip S. Amanik, Gail C. McLaughlin*, arXiv:0707.4191v1, 2007

[19] *J.D.Vergados, Y. Giomataris, Yu. N. Novikov* , J.Phys.Conf.Ser.259:012100,2010, arXiv:1010.4388v1

[20] *J.D.Vergados, Y. Giomataris, Yu. N. Novikov*, Nucl.Phys.B854:54-66,2012, arXiv:1103.5307v2

[21] *Γεωργία Η. Καραθάνου*, Ηλιακά νετρίνα : Επεξεργασία, ανάλυση και προσομοιώσεις διαστημικών και επίγειων παρατηρήσεων, Διδακτορική Διατριβή, Πανεπιστήμιο Ιωαννίνων, 2010

[22] *Βαΐτσα Α. Τσακαστάρα*, Μελέτη αστροφυσικών νετρίνων με τεχνικές προσομοίωσης και υπολογισμούς πυρηνικής δομής, Διδακτορική Διατριβή, Πανεπιστήμιο Ιωαννίνων, 2010

[23] *Battistoni, G and Ferrari, A and Lantz, M and Sala, P R,Smirnov, G*, A neutrino-nucleon interaction generator for the FLUKA Monte Carlo code, 2010

[24] *J. D. Vergados*, arXiv:1103.1107v2, 2011

[25] *Carlo Bemporad, Giorgio Gratta, Petr Vogel*, Rev.Mod.Phys.74:297,2002, arXiv:hep-ph/0107277v1

[26] *V. Kopeikin, L. Mikaelyan, V. Sinev*, Phys.Atom.Nucl. 67 (2004) 1963-1968, arXiv:hep-ph/0308186v1

[27] *Patrick Huber, Thomas Schwetz*, Phys.Rev. D70 (2004) 053011, arXiv:hep-ph/0407026v2

[28] *Maury Goodman, Thierry Lasserre*, arXiv:hep-ex/0606025

[29] *John M. LoSecco*, Double Chooz – A ν_e Experiment to Measure θ_{13}, March 24, 2005

[30] *David Lhuillier*, ν spectrum emitted by a reactor, 2011

[31] *Vogel, P. and Engel, J.*, Physical Review D, 39 (11). pp. 3378-3383, (1989)

[32] *K. Nakamura et al. (Particle Data Group)* PASSAGE OF PARTICLES THROUGH MATTER, J. Phys. G 37, 075021 (2010)

[33] *I. Savvidis*, Sphere-3, Am-Be neutron source data, Thessaloniki, November-December 2011

[34] *I. Savvidis*, The Large Volume (1m3) Spherical Proportional Counter, December 2011

[35] *I. Savvidis*, Progress on a Spherical Proportional Counter for Nuclear Reactor and Supernova Neutrino Detection, AUTH, Athens 2011

[36] *R. Lazauskas, C. Volpe*, J.Phys.G37:125101,2010

[37] *J.D. Vergados, Ch.C. Moustakidis*, arXiv:1009.0631v1

[38] *Chen Ya-Zheng et al*, 2011 Commun. Theor. Phys. 55 1059

[39] *J.D. Vergados, Y. Giomataris, Yu.N. Novikov*, arXiv:1105.3654v1, 2011

[40] *G. Mention et al*, Reactor antineutrino anomaly,Phys. Rev. D 83, 073006 (2011)

[41] *Yu.N. Novikov et al*, arXiv:1110.2983v1, 2011

[42] *Glenn F. Knoll*, Radiation Detection & Measurement. John Wiley & Sons Inc.

[43] *Stefaan Tavernier*, Experimental Techniques in Nuclear and Particle Physics, Springer

[44] *F. Sauli*, Principles of operation of multiwire proportional and drift chambers, CERN 77-09, 1977

[45] *Nicholas Tsoulfanidis*, MEASUREMENT AND DETECTION OF RADIATION, Second Edition, Taylor & Francis

[46] *Claus Grupen, Boris Shwartz* , Particle Detectors, Cambridge University Press

[47] *Kai Zuber*, Neutrino Physics, Taylor & Francis

[48] *Richard C. Fernow*, Introduction to experimental particle physics, Cambridge University Press

[49] *G. Battistoni, S. Muraro, P.R. Sala, F. Cerutti, A. Ferrari,S. Roesler, A. Fasso', J. Ranft,*The FLUKA code: Description and benchmarking, Proceedings of the Hadronic Shower Simulation Workshop 2006,Fermilab 6–8 September 2006, M. Albrow, R. Raja eds., AIP Conference Proceeding 896, 31-49, (2007)

[50] *A. Ferrari, P.R. Sala, A. Fasso', and J. Ranft*, FLUKA: a multi-particle transport code, CERN-2005-10 (2005), $INFN/TC_0 5/11, SLAC-R-773$

[51] Wolfram ,S . *The Mathematica Book, Fifth Edition.* 2003

[52] Wolfram, S . *Wolfram Mathematica 7 Documentation Center* "http://reference.wolfram.com/mathematica/guide/Mathematica.html", 2007-2010.

[53] *NIST*, http://www.nist.gov/

[54] *National Nuclear Data Center*, http://www.nndc.bnl.gov/

List of Tables

List of Figures